Surface/Interface Engineering of Si-based Photocathodes for Efficient Photoelectrochemical Hydrogen Production

(表面/界面制御によるシリコン系光電極の効率的な光電気化学水素生成に関する研究)

Sijie LI

Graduate School of Chemical Sciences and Engineering

Hokkaido University

2022

Contents

Contents

Contents

Abstract

Photoelectrochemical (PEC) water splitting is a promising approach to directly convert solar energy into hydrogen fuel. As an attractive light absorber, p-type crystal Si has been intensively studied as a photocathode to carry out PEC hydrogen evolution reaction (HER) due to its earth abundance and remarkable light-harvesting ability (1.12 eV bandgap). However, the easy corrosion of Si in electrolyte solution leads to poor stability, and the excited electron-hole pairs inevitably recombine at the Si/electrolyte interface, causing sluggish surface kinetic for HER. In this regard, the design of Si-based photocathodes with sufficient surface catalytic activity and facile interfacial charge transport should be considered to improve the efficiency and stability of solar-to-hydrogen conversion, especially when low-cost cocatalysts have been developed over the past decades. Therefore, this thesis focused on rational Si surface modification for sensitive photocurrent response, cocatalyst design for high photovoltage, and interface engineering by inserting functional protection layer between Si and cocatalyst for robust stability and rapid charge-transfer kinetics.

In chapter 1, a general background about photoelectrochemistry and a brief overview of Si-based PEC HER were introduced. Then, the recent development of surface/interface engineering strategies (including etching Si photonic textures, loading cocatalysts, introducing protection layers, and fabricating junction structures) to promote the PEC performance of Si photocathodes was summarized.

In chapter 2, an amorphous Si (a-Si) layer was in-situ co-deposited with Pt nanoparticles onto crystal Si (c-Si) photocathode through electroless method, forming a structure of Pt/a-Si/c-Si, in order to facilitate electron transfer from c-Si to Pt. Compared with the Pt/c-Si photocathode, the a-Si layer within Pt/a-Si/c-Si can not only act as an electron transfer mediator but also as a good passivation layer, producing a high-quality a-Si/c-Si buried junction for enhanced photovoltage and photocurrent response. The resulting a-Si/c-Si interface has a large energy band shift simultaneously, forming a potential barrier to suppress carrier recombination and ensure charge transfer. In addition, the a-Si layer serves as the growth substrate of the cocatalyst, which could effectively modulate the size and distribution of Pt nanoparticles to be smaller and more uniform. This Pt/a-Si/c-Si photocathode presented an onset potential of +0.42 V vs. reversible hydrogen electrode (V_{RHE}) and a photocurrent density of 35.0 mA cm^{-2} at 0 V_{RHE} in 0.5

M H_2SO_4. This study provides a feasible manner to improve the photoresponse of Si-based photocathodes based on the construction of surface Si junction structures.

In chapter 3, a NiS_2/NiS heterojunction (NNH) was designed and applied to a planar p-type Si (p-Si) substrate as an effective cocatalyst to achieve progressive electron transfer. The NNH/Si photocathode exhibited an onset potential of +0.28 V_{RHE} and a photocurrent density of 18.9 mA cm^{-2} at 0 V_{RHE}, as well as a 0.9% half-cell solar-to-hydrogen efficiency, which is much superior compared with those of NiS_2/Si and NiS/Si photocathodes. The enhanced performance for NNH/Si was attributed to the contact between the n-type semiconducting NNH and the planar p-Si semiconductor through a p-Si/n-NiS/n-NiS_2 manner that functions as a local pn-junction to promote electron transfer. Thus, the photogenerated electron was transferred from p-Si to n-NiS within NNH as the progressive medium, followed by Ni^{2+} and/or S_2^{2-} of the defect-rich n-NiS_2 phase as the key active sites. This research may pave the way for planar Si-based PEC applications of heterogeneous metal sulfide cocatalysts through the progressive transfer of electrons.

In chapter 4, to reinforce the interfacial interaction at the Si/cocatalyst interface, a synergetic coupling of the anti-reflective Co-P cocatalyst and the anti-corrosive WS_x interlayer on planar p-Si photocathode was investigated for efficient and durable PEC HER in alkaline media. The thin-film WS_x interlayer plays a trifunctional role in 1) protecting Si substrate from alkaline corrosion, 2) providing an appropriate nucleation base for the morphology optimization of Co-P cocatalyst, and 3) promoting the electron transfer from photocathode to the electrolyte. The Co-P cocatalyst could be modulated by controlling thin-film WS_x morphology to have the least light-blocking effect but retain the catalytic activity. The complementary integration of the Co-P film cocatalyst on WS_x/Si photocathode exhibited superior catalytic properties (onset potential of +0.47 V_{RHE}, photocurrent density of −25.1 mA cm^{-2} at 0 V_{RHE}), which benefits from the significantly enhanced reaction kinetics by promoting electron transfer. Meanwhile, through such a rational structure, the optimal Co-P/WS_x/Si photocathode showed long-term stability of 300 h at a high photocurrent density above −25 mA cm^{-2} at 0 V_{RHE} without noticeable degradation. These findings offer a facile and effective interface modulation approach for the further development of durable Si-based photoelectrochemical devices.

In chapter 5, an overall summary of this dissertation work was presented. This thesis carried out a systematic study on the surface/interface engineering of Si-based

photocathodes for efficient and durable PEC hydrogen evolution. In the Si-based PEC-HER system, the inert active surface and easy corrosion of Si can be effectively alleviated through surface-supported cocatalysts. More importantly, the selection and optimization of cocatalysts, as well as suitable surface/interface engineering between Si and cocatalysts are also the keys to further offer tunable optical properties, high mechanical stability, and rapid charge transfer. This thesis progressively revealed that Si surface modification, cocatalyst optimization, and introduction of functional interfacial layer between Si and cocatalyst were of great significance for improving the PEC-HER performance. The relevant findings in this study deepened the understanding of Si-based PEC-HER application, and provided a potential surface/interface engineering strategy for constructing Si-based photocathodes with a high-quality interface and enabling efficient hydrogen production.

Chapter 1 Introduction

1.1 General introduction of photoelectrochemical hydrogen evolution

Fossil fuel-related global CO_2 emission rose by 6% in 2021 to 36.3 billion tons, the highest ever level in records of all time.[1] It has set a shadow on more severe energy and environmental issues that we must face. Using green hydrogen to replace fossil fuels is estimated to reduce 6 billion tons of CO_2 emission over the next thirty years, when the hydrogen fuel is produced through harnessing solar energy.[2] As termed "solar fuel", green hydrogen is strongly regarded as an excellent energy carrier since it is made from H_2O splitting and combusted back to H_2O, achieving net-zero carbon emission. It is also an important chemical feedstock for the present industry manufactory. Using hydrogen as a fuel also has the advantages of high energy density and light packaging. Compared with other chemical fuels, the chemical energy per unit mass of hydrogen is 142 MJ kg^{-1}, which is about 3 times that of other fuels.[3] Thus, solar-driven hydrogen production from water splitting has attracted worldwide interest.

As one of the solar-driven techniques, photoelectrochemical (PEC) water splitting has sparked plenty of studies since Fujishima and Honda demonstrated PEC water oxidation on a TiO_2 photoelectrode for the first time.[4] The overall water splitting reaction as equation (1) is a thermodynamical task because a standard free energy change ΔG^0 of 237.2 kJ mol^{-1} (corresponding a potential of 1.23 V per electron) is required as an energy input for converting one molecule of H_2O into H_2 and 1/2 O_2 under standard conditions (**Figure 1.1**a). Thus, two electrons (e^-) are needed for hydrogen evolution reaction (HER), while four holes (h^+) are required to oxygen evolution reaction (OER) according to equation (2) and (3):

overall water splitting	$H_2O \rightarrow H_2 + \frac{1}{2} O_2$ ΔG^0=237.2 kJ mol^{-1}	(1)
hydrogen evolution reaction (HER)	$2 H^+ + 2 e^- \rightarrow H_2$	(2)
oxygen evolution reaction (OER)	$2 H_2O + 4 h^+ \rightarrow O_2 + 4 H^+$	(3)

The PEC water splitting cell is basically composed of a semiconductor photoelectrode and its counter electrode immersed in an electrolyte. The performance of water splitting is highly dependent on the properties of the semiconductors. Each semiconductor has its intrinsic conduction band at higher potential and valence band at lower potential position. The gap between conduction band and valence band is the energy bandgap for a

semiconductor. The Fermi level (E_F) of p-type semiconductor is located near its valence band (VB), and the band bending will downward when they contact with electrolyte (Figure 1.1b). In contrast, the Fermi level of n-type semiconductor is located near its conduction band (CB), and the band bending will upward when it contacts with the electrolyte (Figure 1.1c).

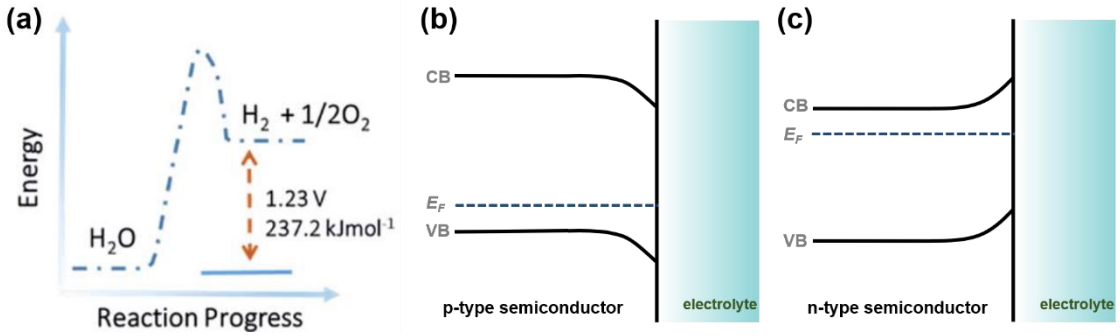

Figure 1.1 (a) The kinetics progress of PEC water splitting reaction.[5] Schematic illustration of the band diagram of (b) p-type and (c) n-type semiconductors at equilibrium in contact with electrolyte.

Under sunlight illumination with energy higher than the energy bandgap of a semiconductor, the semiconductor will absorb the photons and electrons will be excited from the valence band to the conduction band, leaving the corresponding holes in the valence band. The p-type semiconductors with holes as the major carriers are usually used as photocathodes. The photogenerated electrons will diffuse to the surface of photocathodes and participate in the water reduction to produce hydrogen, as shown in **Figure 1.2**. Similarly, n-type semiconductors are usually functioned as the photoanodes, in which the holes will accumulate on the surface of the photoanode for water oxidation to oxygen. However, the recombination of photogenerated electron-hole charges easily occurs during the PEC reaction process, which is the source of the loss in the conversion of solar energy to hydrogen fuel.[6, 7] Therefore, applying an external bias to the PEC system can help promote charge carrier migration and suppress unnecessary recombination.[8] The goal of a PEC device is to generate the maximum photocurrent with minimal bias, which is theoretically determined by the intersection of the steady-state current-potential curves of the photoelectrode.[9] To this end, it can be achieved by using a semiconductor with appropriate bandgap to maximize light absorption and by appropriately modifying the semiconductor to minimize the loss from charge recombination.[10]

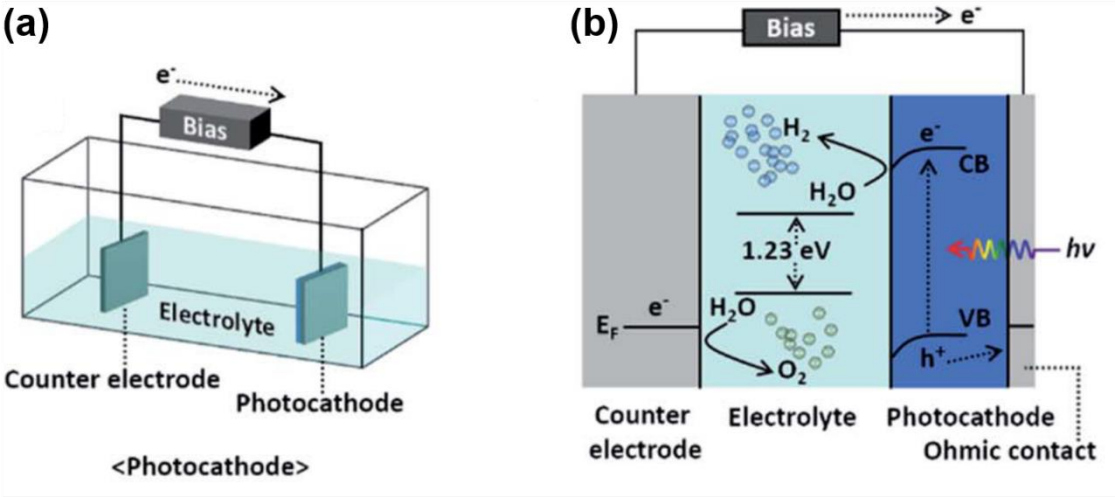

Figure 1.2 (a) Schematic diagram and (b) corresponding detailed mechanism in energy band of a typical PEC water splitting cell using a p-type semiconductor as the photocathode.[11]

Since then, great efforts have been made to explore new semiconductors as photoelectrodes for PEC water splitting system. Notably, the development of efficient semiconductor materials needs to meet the following conditions. First, the bandgap of the semiconductor should be suitable to drive the water splitting reaction by efficiently absorbing and utilizing more sunlight energy, especially visible light. Secondly, the conduction-band-minimum edge position of p-type semiconductor should be more negative than the reduction potential of H^+ to H_2 (0 V *versus* normal hydrogen electrode (V_{NHE}) at pH 0), while the valence-band-maximum edge position of n-type semiconductor should be more positive than the oxidation potential of H_2O to O_2 (1.23 V_{NHE}). The band edge positions of frequently used semiconductors are displayed in **Figure 1.3**. Third, for large-scale industrial applications, semiconductor materials should be selected based on low-cost earth-abundant elements, as well as exploring suitable approaches and technologies to fabricate stable and efficient photoelectrodes.

Undoubtedly, developing both efficient photocathode and photoanode raise the feasibility to achieve unassisted-bias water splitting, while in practice, photocathode and photoanode can be studied separately. Thus, considering the photocathode as half of a key, PEC HER requires adequate offset under electrochemical potential with high current density, for which the emphasis will be to fabricate practical, stable, and cost-competitive photocathodes.[12,13] So far, semiconductors such as Si, Cu_2O, GaN, GaP, InP, CdTe, etc. have been widely studied as efficient photocathodes for PEC HER. However, the

observed photocurrents produced by earth-abundant Cu_2O photocathodes are relatively low because of the relatively large bandgap of 2.0 eV. Furthermore, the scarcity of Ga and In, as well as the toxicity of Cd, have also motivated the exploration of Si semiconductors as photocathodes due to remarkable advantages of the suitable bandgap, earth abundance, non-toxicity, and industrial-scale production.[14, 15]

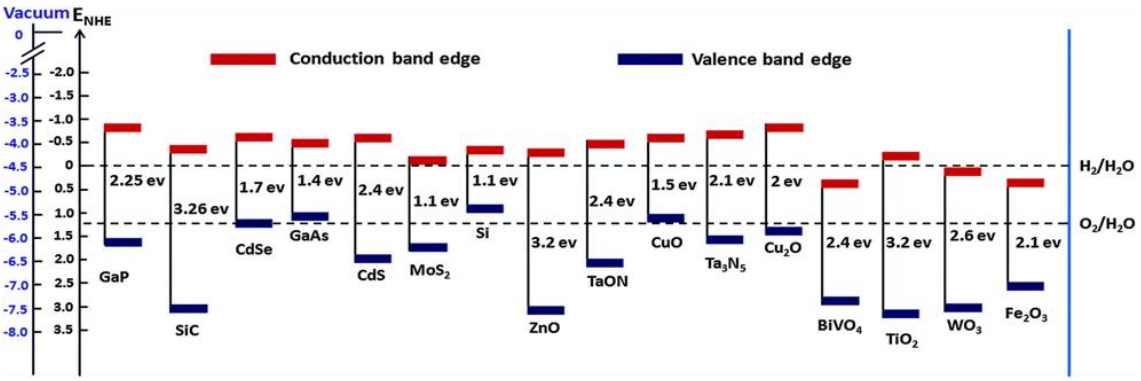

Figure 1.3 Band edge positions of semiconductors in contact with the aqueous electrolyte at pH = 0 relative to normal hydrogen electrode (NHE) and the vacuum level.[16]

1.2 Fundamentals of Si-based photocathodes for PEC HER

Si, with a small bandgap of 1.12 eV that allows light absorption from ultraviolet to near-infrared up to about 1100 nm, has been intensively studied as a photocathode for efficient PEC HER that can reach a high theoretical photocurrent density of up to 44 mA cm^{-2}.[9] Solar-to-hydrogen conversion efficiencies of over 10% have been demonstrated as the benchmark for Si-based photoelectrodes in an increasing number of reports.[17, 18] Since Si has indirect band-edge absorption, which shows less efficient light absorption than direct bandgap semiconductors, a longer optical path is required for efficient light adsorption.[19] Thus, the thickness of the planar Si substrate currently used as a photocathode is usually greater than 50 μm, ensuring efficient light absorption. However, a longer optical path, such as a thick film, results in less efficient transport of the carriers generated deeper inside when the film thickness is greater than the carrier diffusion length.[20] There is another issue that about 25% of incident visible light is reflected at the planar Si/water interface.[21-23] Therefore, the issues need to be addressed if the light absorption of Si is wanted without obvious limitation to achieve the high theoretical photocurrent.[9]

In addition to the suitable bandgap, the conduction band edge position of Si is more negative to the electrochemical potential of HER, suggesting it is suitable to drive the

reaction.[24] The difference between the quasi-Fermi level of Si and the electrochemical potential of HER impels the electron transfer when Si contacts the electrolyte, resulting in a depletion region and a band bending at the Si surface. A downward band bending is necessary for PEC HER to promote electron carrier transfer to drive the reaction while preventing the hole carrier transfer to the surface. It is generally realized by doping less valent elements in Si to lower quasi-Fermi levels, resulting in hole carriers as the majority in p-type Si (p-Si) photocathodes.[22] The potential difference between the quasi-Fermi level of electrons and holes represents the photovoltage of the semiconductor.[21] Theoretically, Si can deliver a maximum photovoltage of about 0.8 V, which is beneficial in reducing the water-splitting reaction overpotential. Noting that voltages higher than 1.8 V are often practically necessary for water-splitting reactions due to transportation, ohmic losses, and overpotentials,[9] even though the thermodynamic potential of 1.23 V is required.[5] Utilizing the maximum photovoltage fully over the Si has always been the object of research interest.

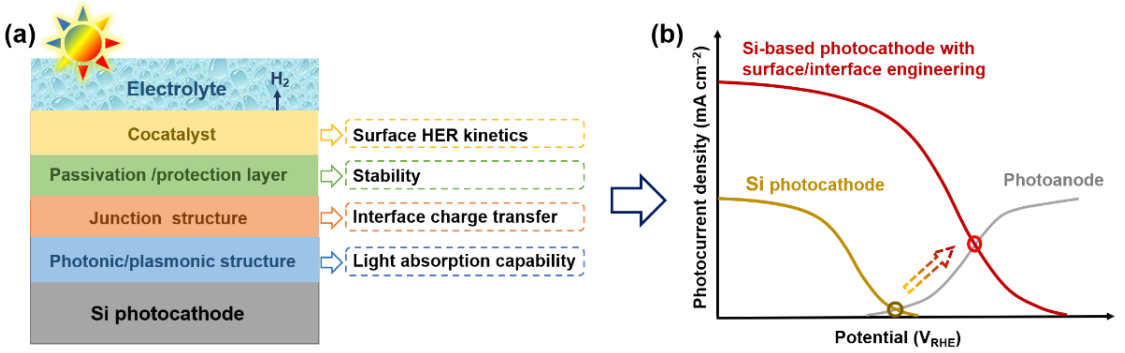

Figure 1.4 (a) Schematic illustration of major surface/interface engineering strategies used for the development of the Si photocathode and the mechanism thereof to improve the PEC-HER performance. (b) Schematic linear sweep voltammograms (LSVs) of the surface/interface modified Si-based photocathode with a potential photoanode are beneficial to achieve overall unassisted water splitting.

Several other key issues are under consideration despite all the aforementioned attractive advantages. First, the bare Si surface is inert for HER due to the large bonding energy of Si with proton confirmed experimentally.[25] The Si-H bonding energy is 3.1 eV, far away from the optimal M-H bond energy of 2.5 eV in the "volcano plot" evaluation.[26-28] Second, the thermodynamic instability of Si originates from the fact that its self-oxidation potential of about –1.0 V_{NHE} is placed above $E(O_2/H_2O)$, which causes the Si surface to be easily oxidized and corroded in high ionic strength electrolytes.[29] So it is

beneficial to cut off the direct contact between the Si surface and the electrolyte. Meanwhile, the self-reduction potential (~0.2 V_{NHE}) of Si is placed between the conduction band and $E(H_2/H_2O)$, leading to sluggish surface HER kinetics.[30] Third, the PEC process is relative to the electron transfer from the Si to the electrolyte species, crossing some mediate or cocatalyst layers in most cases. Si has surface band bending in contact with other materials, so favorable band bending is necessary for the prompt interfacial charge–transfer kinetics.[31]

Therefore, to solve the above-mentioned original issues of Si, it is necessary to comprehensively improve various characteristics through the surface/interface engineering strategies, as schematically illustrated in **Figure 1.4**a. Especially, as more non-precious and efficient HER cocatalysts have been developed[5, 32, 33], the surface/interface engineering becomes more vital to integrate the performance balance among the electron transfer, light absorbance, corrosion resistance, etc.[34] Specifically, the introduction of photonic texture or plasmonic metal nanoarchitecture on the Si surface can reduce the loss of reflected and scattered light, resulting in higher incident photon-to-current conversion efficiency for solar-driven hydrogen production. The inert active surface of Si can be effectively alleviated through surface-supported cocatalysts to enhance surface HER kinetics at the solid/liquid interface. Furthermore, suitable interface modifications, including junction structures and protection/passivation layers, are also the keys to offering further tunable optical properties, high mechanical stability, and rapid charge transfer. Eventually, a photocathode with excellent HER performance in key aspects is obtained to match the photoanode better to achieve a practical overall water splitting system under an unbiased potential (Figure 1.4b).

1.3 Surface/interface engineering strategies to improve the PEC performance of Si-based photocathodes

1.3.1 Photonic/plasmonic structures for enhanced light absorption

One of the most critical challenges in realizing solar-driven hydrogen production is to utilize the full solar spectrum. Unfortunately, limited by the mismatch between the semiconductor bandgap and the photon energy, a theoretical light utilization efficiency can only reach around 30% of the full solar spectrum for a single absorber.[35] So then, the essential will be to maximize light utilization to this theoretical efficiency at the most. Introducing surface photonic textures over Si photocathodes is an effective strategy to

reduce reflection and scattered light loss.[36-38] The internal reflection of light over the Si photonic structures could be enhanced due to their high aspect ratios, and the wavelength range of absorbable light could also be broadened, thereby maximizing the optical absorption capacity and conversion efficiency. So far, introducing surface photonic textures mainly focuses on Si nano/micro-wire, micro-pyramid, nano/micro-pillar, and nanohole arrays. In addition, noble metals (such as Pt, Au) as the most active HER catalysts were initially utilized on Si-based photocathodes, while recently, their nanostructures have drawn more attention on the plasmonic effect over the electron transfer at the interface of Si/cocatalysts. Localized surface plasmon resonance (LSPR) could be triggered by accurately regulating the size and geometry of noble metal nanoparticles, which can enhance light-harvesting capability in a surface-near region and excite vast electrons under light illumination.[39, 40]

1.3.1.1 Photonic structures

Nanowire (NW) array, as one of the most typical Si surface photonic textures, has been widely explored. The structural evolution, optical properties, and PEC-HER performance of Si NWs were well investigated by Gopalakrishnan et al. in neutral solutions.[41] The Si NW array was constructed through a metal-assisted chemical etching (MACE) process utilizing H_2O_2 as oxidants. When the H_2O_2 concentration increased, the length and etching rate of the NWs increased, resulting in the morphology change from vertical to porous structure due to the higher etching rate of lateral than axial direction. The anti-reflection is significantly heightened in visible light because of the multiple reflections of photons and entire internal reflection of Si NW inner surface. In addition, Nam et al. tuned the length of the Si NW array (**Figure 1.5**a) by controlling the etching time using a metal-catalyzed electroless etching (MCEE) approach.[42] They observed a structural transformation from porous to NWs as the etching time increased, along with the increase of NW length. As MACE and MCEE methods generally produce lowly-ordered Si NW arrays, the researchers have concentrated on the highly-ordered and vertically-oriented Si NW arrays. Liu et al. introduced the Si NW array photocathode with homogeneous structural parameters, as shown in Figure 1.5b, which employed the e-beam lithography method and deep reactive ion etching (DRIE).[43] They first investigated the effect of Si NW inter-wire spacing and diameter on the PEC-HER property and speculated that the optimal sample is a combination of 175 nm inter-wire spacing and 200 nm diameter. The micro-pyramid (MPy) array is another widely studied Si photonic texture. Hou et al.

fabricated typical Si MPy arrays with a height of 2-6 μm from planar Si.[44] Compared to planar Si, which has a reflectance of about 25% at normal incidence in the range of 600 to 900 nm, the overall reflectance of the MPy-structured Si surface is reduced to less than 10%. Jin et al. successfully designed Si MPy array with n^+pp^+ junction as the light absorber with omnidirectional broadband light-trapping ability (Figure 1.5c).[45] Like the traditional upright MPy arrays, the inverted MPy arrays have recently attracted attention. Yuan et al. synthesized Si inverted MPy arrays via copper-assisted chemical etching with a low reflectance of about 6.55% (Figure 1.5d).[46]

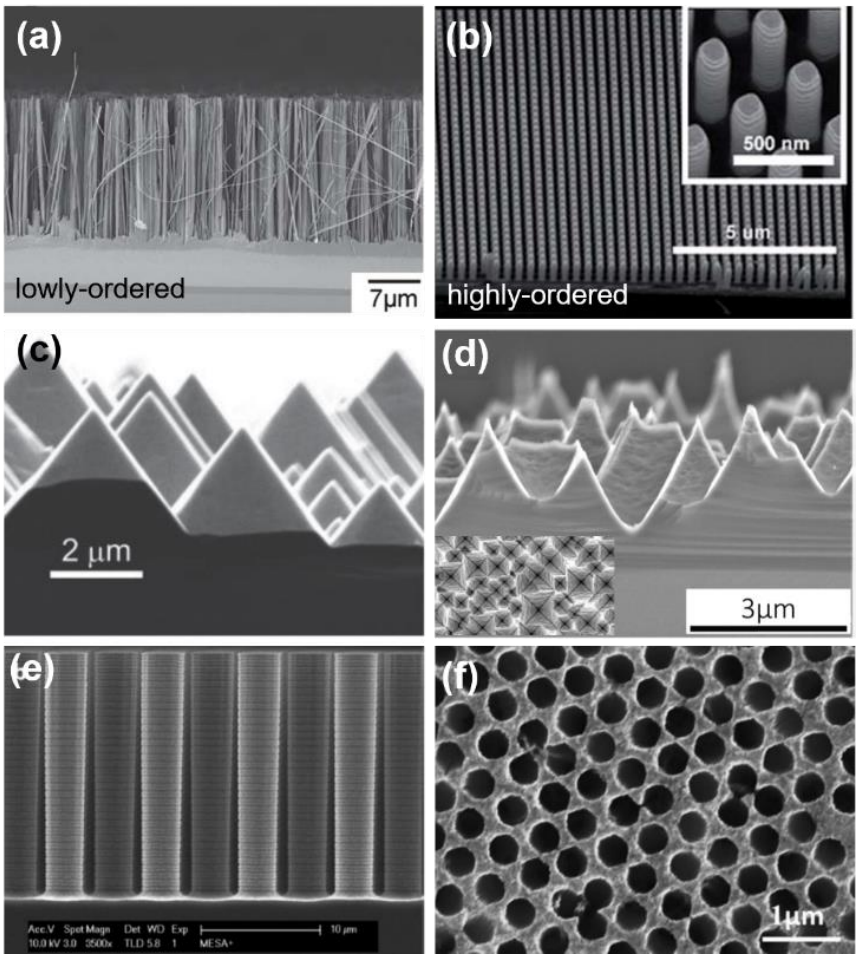

Figure 1.5 Typical morphology of micro/nanostructured-Si: (a) lowly-ordered Si NW arrays using MCEE approach[42], (b) highly-ordered Si NW arrays using e-beam lithography method followed by DRIE[43], (c) Si MPy arrays[45], (d) Si inverted MPy arrays[46], (e) Si MP arrays[47], (f) Si NH arrays[48].

Besides Si NW and MPy arrays, other surface modification strategies to fabricate Si optical textures, such as micropillar (Figure 1.5e) and nanohole arrays (Figure 1.5f), also have been proposed. The features of micropillars, such as height, diameter, and pitch, are

well studied as the factors determining the vital parameters for PEC HER, including light absorption capacity, surface area, and charge separation.[49,47] Most studies concluded that an appropriate length of the Si pillars is the key to obtaining optimal PEC HER. Similar to controlling the micropillar length, the depth optimization of the Si nanoholes as photocathode is also a research focus. For example, Si nanoholes array with 0.6 μm modified depth as a photocathode exhibits a saturated photocurrent of 28 mA cm^{-2} in an acid electrolyte, higher than 21.5 mA cm^{-2} for planar Si.[48] In reality, there is a trade-off between carrier recombination and surface area for Si nanoholes arrays with the effect of nanoholes depth. When the depth of Si nanoholes arrays increases, the increased surface area plays a dominant role in increasing the current, and the subsequent rise in Si nanoholes depth beyond 1.1 μm makes the interfacial recombination dominate, and thus the limiting-current reduces significantly. The problem can be resolved using tapered Si nanoholes arrays, which feature a refractive index gradient and increase the optical bandgap for field-effect surface passivation to further suppress recombination losses.[50]

Incorporating surface photonic textures has demonstrated the potential advantages in light absorption and antireflection over planar Si photocathodes. However, the textured structures may generate impurities and defects, creating surface trap states for carrier recombination. Therefore, the parameters of the surface-textured Si should balance the two key factors of light absorption and surface recombination. On the other hand, the construction of Si textured structures involves complex and time-consuming processing. In this regard, the use of planar Si is more cost-effective and greatly simplifies the pretreatment operation, which is beneficial for the industrialization of Si-based photoelectrodes for solar water splitting.

1.3.1.2 Plasmonic nanoarchitectures

Noble metal nanoparticles (NPs) can enhance the optical absorbance through the localized surface plasmon resonance (LSPR).[40] For example, Han et al. employed Au or Pt NPs on 3C-SiC emitter-protected Si photocathodes, obtaining LSPR-induced enhancement of the saturated photocurrent to 38 mA cm^{-2} by tuning the size, geometry, and distribution of the metal NPs.[51] Ge and coworkers embedded Au nanorings (NRs) into Si nanohole arrays with TiO_2 layers, finding that controlling the geometry and size of Au NRs could trigger the LSPR effect.[39] By simulating electric field distributions at 560 nm, as shown in **Figure 1.6**a-b, the hot electrons are concentrated on the Au NRs top adjacent to the Schottky junction, which is favorable for the electron transfer through the

junction. Similarly, Liu and colleagues utilized plasmonic Ag on Si microwire array and systematically investigated the LSPR effect of Ag nanostructures for PEC HER.[52] From the UV-Vis spectra (Figure 1.6c), although the deposition of Ag plasmonic particles blocks the absorption of Si microwires in the visible light, it also extends the absorption edge to the UV region. Based on the finite element method simulations (Figure 1.6d), the electric field intensity at 380 nm (Ag plasmonic adsorption of light) is higher than that at 300 nm (Ag inherent adsorption of light), which suggests that it is the plasma-induced electric field rather than the inherent absorption of Ag particles. Therefore, owing to the cooperative function of the Ag plasmonic and catalytic support to promote the generation of charge carriers, the V_{on} of the Ag-decorated Si microwire photocathode is positively shifted by 0.5 V compared with the bare Si microwire.

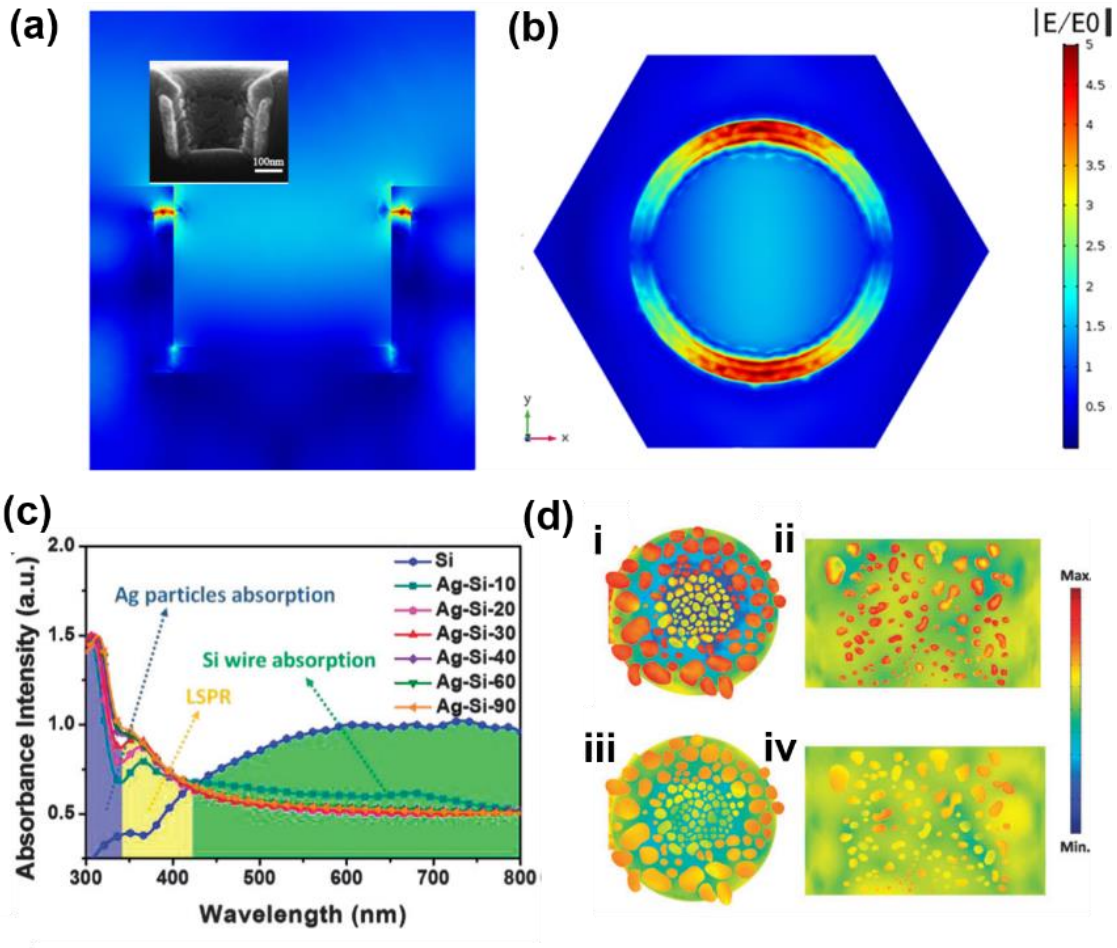

Figure 1.6 Electric field (|E/E0|) distributions simulated by COMSOL Multiphysics: (a) cross view perpendicular to the direction of the electric field, and (b) top view of the interface between the Si surface and the TiO_2 layer.[39] (c) UV-vis spectra of Ag/Si photocathodes with different Ag deposition time, and (d) electric field intensity maps of

Ag-decorated Si MWs obtained from FEM simulations at (i and ii) λ = 380 nm and (iii and iv) λ = 300 nm.[52]

1.3.2 Junction structures for facile interface charge transfer

The narrow band gap of Si results in a limited photovoltage generated through the Si/electrolyte junction. In order to generate the increasing photovoltage needed to drive the PEC HER, phosphorus and boron atoms are usually doped into the surface of the Si wafer by thermal diffusion, ion implantation, spin-on, or plasma-enhanced chemical vapor deposition (CVD) methods to form a buried p-n junction (such as pn^+, p^+pn^+, and n^+np^+ junctions). These buried p-n junction structures provide a built-in electric field with a larger band bending degree to accelerate the outward migration of photogenerated carriers effectively. In addition to the buried Si p-n homojunction for high photovoltage, other Si-based heterojunctions have also been investigated as high-quality interfacial photocathodes. The design of the metal-insulator-semiconductor (MIS) junction structure plays a vital role in defensing Si semiconductors from the corrosive liquid electrolyte and facilitating the photogenerated carrier transfer. One key point in building the MIS structure is to tunnel the insulator layer, usually a thin metal oxide layer.[53] The formation of Si heterojunctions by coating Si with other functional semiconductors with more favorable band alignment has also been studied to enhance the photovoltage of Si photocathode for PEC application.

1.3.2.1 Buried p-n junctions

The surface n^+p junction, as a representative member of buried junctions, has been broadly exploited to provide a built-in electric field from n→p for a p-Si photocathode to accelerate the outward migration of photogenerated carriers. Generally, an n^+p-Si junction is first formed by supporting an n^+ emitter layer on the planar Si surface by thermal diffusion with $POCl_3$ as a phosphorus source at high temperature. The modifications of functional interlayer and/or HER cocatalyst loading are then carried out based on the n^+p-Si substrates to obtain Si-based photocathodes with high-quality interfacial structures. These Si-based photocathodes with built-in n^+p junctions exhibit a greater V_{on} in both acidic and alkaline conditions.[54, 55] Studies further shows that adding a p^+ layer on the backside of n^+p-Si can promote majority carrier collection and improve PEC-HER performances. Therefore, Vesborg et al. firstly designed a back-illuminated Si-based photocathode with a n^+pp^+ junction using the ion implantation method for PEC HER.[56]

Based on the data of the theoretical study, it is found that n^+pp^+-Si with Si thickness as a parameter can evaluate the effect of the carrier diffusion length/thickness (L_e/L) ratio on the probability of charge collection. Further experimental investigation demonstrates that the p^+pn^+-Si with 50 μm thick showed the highest photocurrent of 17.0 mA cm^{-2} under backlight illumination. However, the 350 μm thick sample with a 7-fold lower L_e/L ratio displays only a photocurrent of 6.1 mA cm^{-2}, and the 30 mm thick sample with an improved L_e/L ratio also shows a slightly lower photocurrent because of its infrared photon loss.

In reality, surface modification of buried junctions can combine with surface texture fabrications. Jin's group fabricated Si micropyramid photocathodes integrating n^+pp^+-junction (n^+ emitter layer fabricated by thermal diffusion and p^+ back surface field layer formed by screen-printing Al and annealing process) and examined the advantage of n^+pp^+-Si over planar Si in PEC-HER systems.[45] Due to the beneficial bending of the n^+pp^+-junction, the V_{on} of MoS_xCl_y- and $MoSe_xCl_y$-coated n^+pp^+-Si micropyramid photocathode under illumination are dramatically higher than those using planar Si from 0.27 V *versus* reversible hydrogen electrode (V_{RHE}) to 0.41 V_{RHE} and 0.18 V_{RHE} to 0.35 V_{RHE} in 0.5 M H_2SO_4, respectively. They further integrated CoPS on n^+pp^+-Si micropyramid and achieved a relatively higher V_{on} of 0.45 V_{RHE} under the same acid electrolyte.[57] Zhang et al. also reported that a V_{on} of about 0.5 V_{RHE} is obtained in 1 M KOH alkaline solution for a micropyramid-textured n^+p-Si/Ti/NiS_xO_y photocathode.[55] Furthermore, Shen et al. found that the photocathode of n^+np^+-Si with a micropyramid textured surface exhibited better PEC-HER performance in alkaline electrolytes than the corresponding n^+pp^+-Si, where the fabrication process of the junctions contained the spin coating of phosphorus and boron dopant precursors and the subsequent thermal diffusion.[58] From their points, n^+np^+-Si photocathodes enable backside illumination of Si substrates, while front-side protection layers and cocatalysts can be thick enough to design stable and efficient photocathodes without shading concerns. Thus, compared with n^+pp^+-Si micropyramid photocathode with integrated Ni-Mo cocatalyst and Ni protection layer, the V_{on} of n^+np^+-Si MPy photocathode with the same cocatalyst and protector positively shifts from 0.4 to 0.5 V_{RHE} in 1.0 M KOH.

The Si surface modification have been proven to be beneficial to PEC HER enhancement. Most of these works can be the base of the further interface engineering. In specific, the matching of Si photonic textures or buried junctions with subsequent

deposition of functional layers and cocatalysts also needs attention. Therefore, designing novel Si surface structures with the excellent light-harvesting ability and low surface recombination loss, matched with other functional interfaces, is crucial for efficient solar water splitting for hydrogen production.

1.3.2.2 Heterojunctions

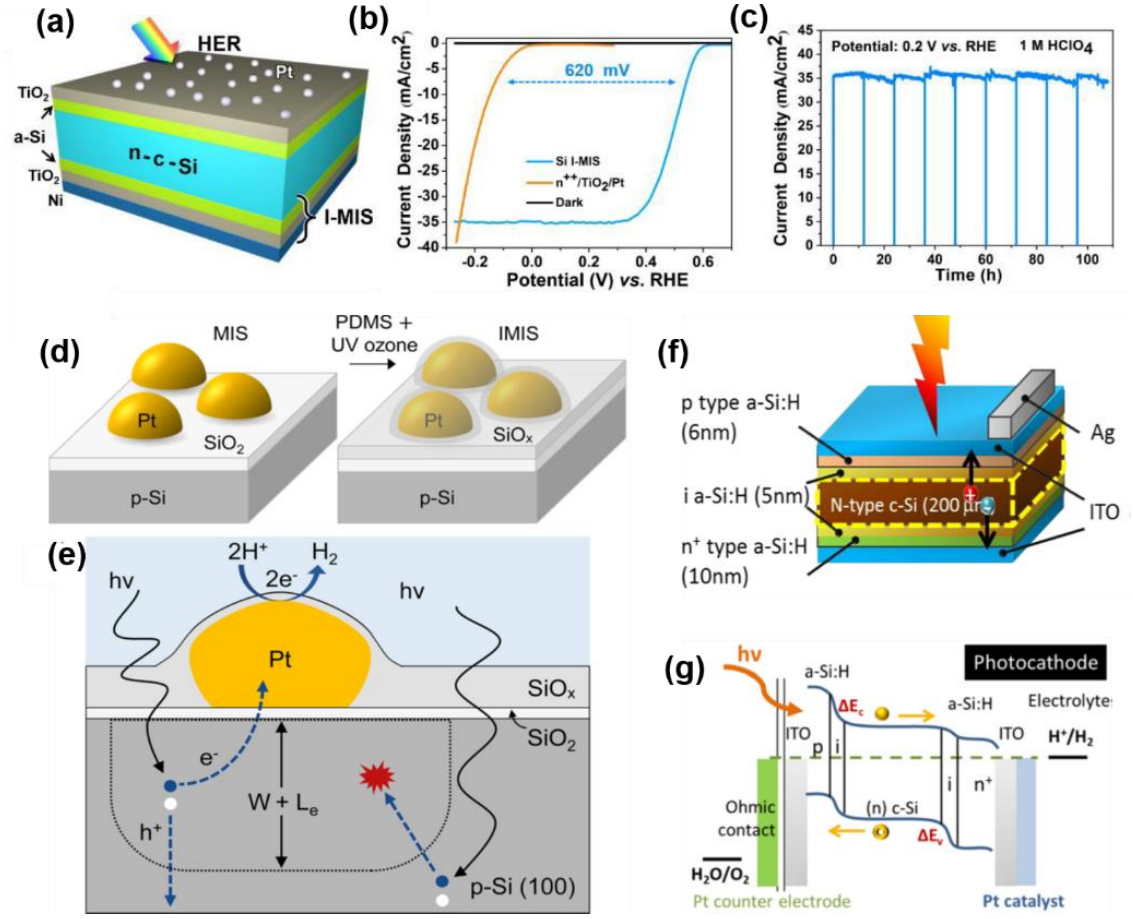

Figure 1.7 (a) Schematic diagram, (b) LSVs, and (c) durability test of the Si I-MIS photocathode.[60] Schematic diagrams of (d) a MIS photocathode and an IMIS photocathode covering a SiO_x layer, and (e) the basic operational process occurring in an IMIS photocathode.[61] (f) Configuration and (g) the energy band diagram of the a-Si/c-Si heterojunction photocathode.[17]

In addition to the buried Si p-n homojunction, tunneling the band bending can be achieved by the metal-insulator-semiconductor (MIS) junction[53]. For example, Talin et al. demonstrated a well-behaved MIS junction photocathode, in which a 2 nm SiO_2 insulator thin-film was grown on p-Si and Pt/Ti bilayer collectors was deposited onto the oxide layer.[59] The SiO_2 layer was obtained by rapid thermal oxidation to guarantee the SiO_2/Si

interface with a low defect density. Besides, the Ti layer with low work function was used as an adhesion layer for the Pt cocatalyst to ensure smooth electron transfer. Notably, there is a trade-off between light absorbance, electron transfer, and protective properties when fabricating MIS junctions. In detail, thick insulators or metal layers block the light absorption of Si, and thick insulators also hinder the charge carrier transport, while thin insulators cannot provide sufficient interfacial passivation. To avoid the parasitic light absorption, Wang and coworkers fabricated an inverted MIS (I-MIS) junction for a Si photocathode with a Pt cocatalyst by moving the MIS junction to the backside of Si substrate, exhibiting a V_{on} of 0.62 V_{RHE} and a stable operation over 108 h illumination (**Figure 1.7**a-c).[60] In addition, modifying the metallic component is also critical to achieve high photovoltage in MIS junction. For example, Esposito et al. used a Pt/SiO_2/Si photocathode as a MIS prototype, and then deposited an additional SiO_x insulating layer on top of the Pt nanoparticle to form an IMIS junction (Figure 1.7d-e).[61] The results suggest that the SiO_x overlayer with mild conductivity reduces the resistance of charge transfer while simultaneously stabilizes electrodeposited Pt nanoparticles.

Integrating Si heterojunction with other functional layers with synergetic advantages is also a promising strategy to achieve higher photovoltage and photocurrent.[62] An n-type CdS film produced by chemical bath deposition on p-Si photocathode, forming a p-Si/n-CdS heterojunction, has been reported to have suitable band alignment.[63] It shows excellent rectification properties as well as brings to a higher Schottky barrier and a thicker depletion layer, thereby promoting the separation of photo-induced electron-hole pairs. Compared with Si/Pt photocathode, the V_{on} and photocurrent density at 0 V_{RHE} of Si/CdS/Pt heterojunction photocathode increased from 0.1 to 0.3 V_{RHE} and from 0.7 to 12.5 mA cm^{-2}, respectively. InAs semiconductor with narrow bandgap and superior electron mobility also became a promising candidate for Si-based heterojunction to realize efficient hydrogen evolution.[64] However, the CdS film produced by by chemical bath deposition would generate surface defects, and the InAs material is chemically unstable in electrolytes. Therefore, they need passivation layers like TiO_2 to enable long-term stability.[64] Moreover, He et al. fabricated an amorphous Si/crystal Si (a-Si/c-Si) heterojunction photocathode to obtain a good surface passivation for robust PEC hydrogen evolution.[17] They found that intrinsic hydrogenated form a-Si:H on the front and back contacts significantly passivated the dangling bonds on the c-Si surface (Figure 1.7f), resulting in high-quality junctions with low densities of surface states. At the same

time, the a-Si:H/c-Si interface have a large band offset (Figure 1.7g), forming a potential barrier to suppress the carrier recombination, that is, an additional field-effect passivation. This a-Si/c-Si heterojunction photocathode with 2 nm sputter-coated Pt cocatalyst presented a V_{on} of 0.64 V_{RHE} at 1 mA cm^{-2} and a STH efficiency of 13.26 % in 1.0 M H_2SO_4.

The junction structures with functional interfaces, such as adhesion, passivation, and tunnel interface on Si photocathodes, have been proven to promote the separation and transport of photoelectrons. Simultaneously, it suggests to fill necessary requirements for the selected component materials within Si junctions, and the following aspects need to be considered: intrinsic chemical and optical properties, regulation of parameters such as morphology, size and thickness, the degree of matching between Si and cocatalyst, as well as the cost and operability of the construction technology.

1.3.3 Cocatalysts for improved HER kinetics

Aiming at the inert active site over the bare Si surface, a universal modification strategy is proposed to improve the surface reaction kinetics and reduce the activation energies of HER by loading a cocatalyst on the Si surface. When introducing a cocatalyst on the Si surface, the band bending becomes complicated at the interface of Si/cocatalyst, which might inhibit the electron transfer when the band bending is upward. Specifically, metal cocatalysts with a lower work function than Si can introduce a built-in electric field through forming a Schottky junction at the metal/Si interface, thereby facilitating the separation and transport of photogenerated charge carriers to the electrolyte for HER. Conversely, metals with a higher work function than Si would be detrimental to the transport of photogenerated electrons. A typical case is that even though Pt is widely regarded as the most beneficial catalyst for HER, its simple decoration onto the Si surface cannot bring an obviously enhanced PEC HER. Besides, it is worth noting that some cocatalyst materials, especially metals with parasitic light absorption, tend to hinder the light collection from the underneath Si. In addition to precious metal cocatalysts, cost-effective HER cocatalysts based on earth-abundant metal elements (Mo, Co, Ni, etc.) have been explored and investigated, such as their alloys or compounds, as better options for practical PEC hydrogen evolution.

1.3.3.1 Metals and alloys

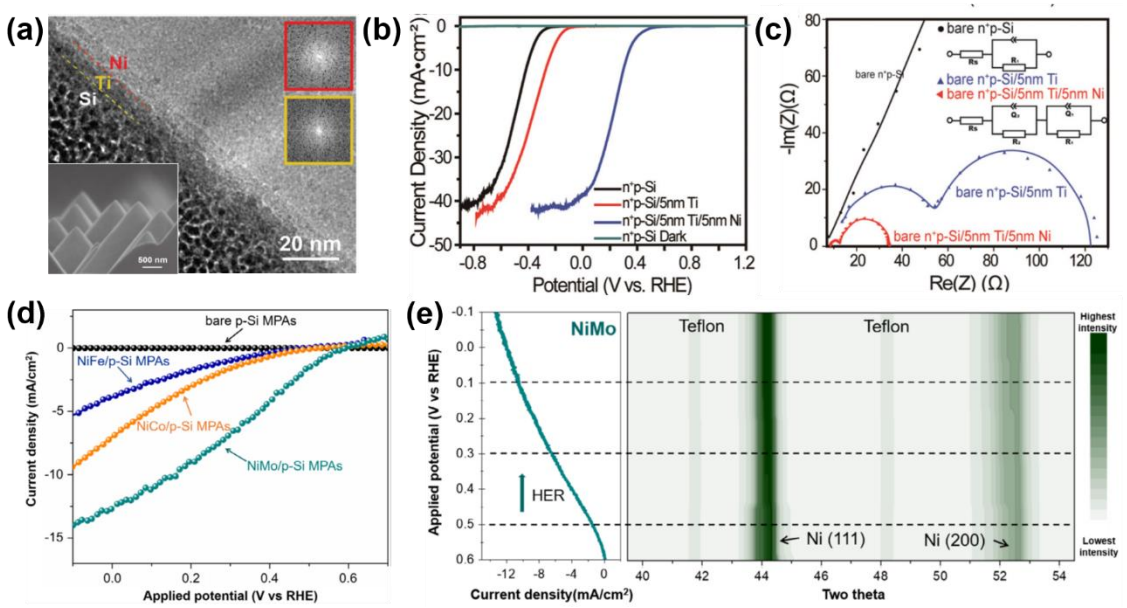

Figure 1.8 (a) TEM image of n^+p-Si/5 nm Ti/5 nm Ni photocathode, FFT images of Ti (yellow) and Ni (red) inset; (b) LSVs and (c) Nyquist plots of bare n^+p-Si, n^+p-Si/5 nm Ti and n^+p-Si/5 nm Ti/5 nm Ni photocathodes, fitted equivalent circuits inset.[65] (d) LSVs of the Ni-based alloys/p-Si MPAs photocathodes and (e) in situ grazing angle X-ray scattering measurements of the NiMo/p-Si MPA photocathode.[49]

The search on non-precious metals and their alloys has attracted great attention for large-scale PEC water reduction. Zhang et al. investigated a 5 nm Ni amorphous layer as an excellent cocatalyst on the 5 nm Ti-protected mircropyramid-like n^+p-Si photocathode (**Figure 1.8**a).[65] The n^+p-Si/5nm Ti/5nm Ni photocathode yields a higher V_{on} of 0.61 V_{RHE} in 1.0 M KOH, while the V_{on} of n^+p-Si/5nm Ti is only –0.03 V_{RHE} (Figure 1.8b). Moreover, n^+p-Si/5nm Ti/5nm Ni photocathode exhibits a photocurrent of –38.7 mA cm^{-2} at 0 V_{RHE}, which is even higher than that of n^+p-Si/5nm Ti/Pt NPs (–20.4 mA cm^{-2}). The better PEC performance is attributed to the superior interface of Si/Ti/Ni with rapid charge transfer kinetics, as proven by electrochemical impedance spectroscopy measurements (Figure 1.8c). Besides, various Ni-M (M=Mo, Fe, and Co) alloys have been investigated as HER cocatalysts onto p-Si micropillar arrays (p-Si MPAs) photocathodes in alkaline electrolytes by Chen and coworkers.[49] The photocurrent of NiMo/p-Si MPA photocathode at 0 V_{RHE} is –12.5 mA cm^{-2}, which is higher than –7.4 mA cm^{-2} for NiCo/p-Si MPAs and –4.0 mA cm^{-2} for NiFe/p-Si MPAs in 1.0 M KOH (Figure 1.8d). An in-situ study based on grazing angle X-ray scattering results supported that two Ni diffraction peaks of

NiMo/p-Si MPAs shift slowly to lower values during HER process, which indicates lattice expansion due to more Mo diffusing into Ni (Figure 1.8e). This lattice strain may be ascribed to increased surface defects, possibly facilitating the generation of active sites for NiMo alloy. Another typical work by Huskens prepared Ni-Mo alloy cocatalysts electrodeposited on n^+p-Si microwire photocathodes and investigated the influences of the selective Ni-Mo coverage over the Si microwires with different pitches.[66] Therefore, the optimal Ni-Mo/n^+p-Si microwire photocathode displays a V_{on} of 0.49 V_{RHE} and a saturated photocurrent of 35.5 mA cm^{-2} in 0.1 M H_2SO_4 (pH 1).

1.3.3.2 Metal compounds

Earth-abundant transition metal (Mo, Co, Ni) compounds (sulfides, phosphides, selenides, etc.) with comparable catalytic activity also have been widely designed and exploited. In the following parts, we focused on the application of transition metal (Mo, Co, Ni) compounds for PEC HER. As one of the most classical earth-abundant HER electrocatalysts, MoS_2 has been extensively investigated to boost the catalysis and stability of Si-based photocathodes in acid electrolytes. Generally, MoS_2 nanoparticles or nanofilms exhibit superior HER activity than bulk MoS_2. An early study by Jaramillo and co-workers has integrated conformal MoS_2 nanolayers cocatalysts on planar n^+p-Si for PEC HER through in-situ sulfurization of sputtered Mo metal films.[67] This as-prepared MoS_2/n^+p-Si photocathode shows a V_{on} of 0.32 V_{RHE} and 100-h excellent stability. Shen et al. also integrated MoS_2 on Al_2O_3 coated n^+p-Si photonic texture, obtaining a saturated photocurrent of 35.65 mA cm^{-2} along with a stable 120-h operation.[68] Furthermore, the chemically exfoliated metallic 1T-MoS_2 shows better electrocatalytic HER activity than the semiconducting 2H-MoS_2.[69, 70] Benefitting from the metallic transport and proliferated active edge sites of 1T-MoS_2 phase, the CVD-grown 1T-MoS_2/Si presented a V_{on} of 0.25 V_{RHE} and a photocurrent of 17.6 mA cm^{-2} at 0 V_{RHE}, which is superior to the CVD-grown 2H-MoS_2/Si (0.23 V_{RHE} and 4.2 mA cm^{-2}) as shown in **Figure 1.9**a.[69] Recently, our group reported an efficient amorphous MoS_x (a-MoS_x) for PEC-HER enhancements via self-reductive assembly on planar p-Si, where p-Si was used as a reducing agent to reduce the $(MoS_4)^{2-}$ anion at room temperature to form a-MoS_x onto the Si surface (Figure 1.9b).[71] As a result, the as-fabricated a-MoS_x/Si photocathode outperforms the PEC performances of 1T-MoS_2 and 2H-MoS_2 cocatalysts on Si.

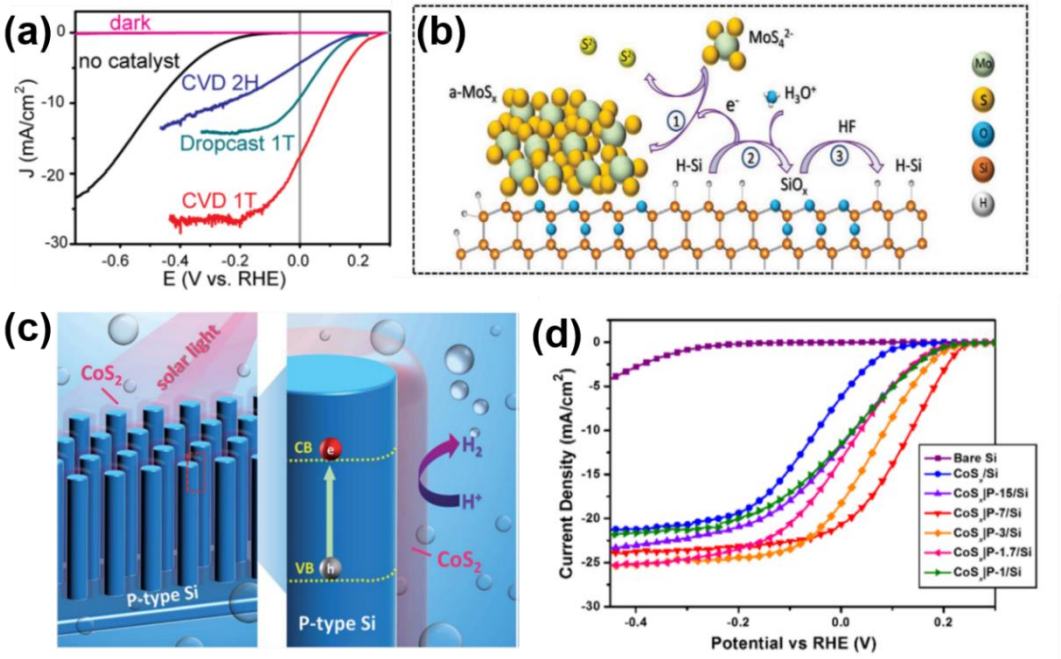

Figure 1.9 (a) LSVs of CVD 2H, CVD 1T, and drop cast 1T MoS_2/Si photocathodes.[69] (b) Schematic diagram of a-MoS_x grown on p-Si via self-reductive assembly process.[71] (c) Schematic illustration of the CoS_2 cocatalyst passivation layer decorated Si MW photocathode.[74] (d) LSVs of bare Si, CoS_x/Si, and CoS_x|P/Si photocathodes.[75]

Co-based compounds, especially Co-P compounds, are the well-known active HER electrocatalysts. Surface-site-averaged TOF calculations by Jaramillo et al. showed that CoP was the most active HER electrocatalyst among transition metal phosphides as of 2015.[72] After metallic Co evaporated on Si wafers followed by a phosphorization treatment of the Co-Si substrates, CoP thin films with high TOF were further loaded on n^+p-Si photocathodes, which achieved excellent PEC activity, with a V_{on} of 0.46 V_{RHE} to reach −0.5 mA cm^{-2} in 0.5 M H_2SO_4. Geyer et al. deposited colloidal CoP_2 nanocrystals on p-Si with Al-ZnO (AZO) passivation layer and TiO_2 protection layer to fabricated a p-Si/AZO/TiO_2/CoP_2 photocathode by modified hot-injection method.[73] For the resulting photocathode, the V_{on} positively shifted to 0.48 V_{RHE} and the photocurrent increased to −16.7 mA cm^{-2} at 0 V and well sustained over 60 h operation in acidic condition. Electrochemically stable CoS_2 was also selected as a cocatalyst to be decorated on p-Si MWs for PEC hydrogen evolution (Figure 1.9c).[74] The optimized V_{on} and photocurrent density at 0 V_{RHE} of CoS_2/Si microwire photocathode were 0.248 V_{RHE} and −3.22 mA cm^{-2}, respectively. Doping P atoms into CoS_x as a cocatalyst was further reported for enhanced Si-based PEC-HER activity. In the case of P-doped CoS_x-decorated Si

micropyramid arrays, Liu and colleagues found that as more P atoms were doped into the CoS_x cocatalyst, an increase in vacancies for unoccupied electronic states was observed.[75] As a result, the optimized P-doped CoS_x/Si photocathode displayed a high photocurrent density of −20.6 mA cm^{-2} at 0 V in 0.5 M H_2SO_4 as shown in Figure 1.9d.

Recent studied explored Ni-S compounds with various crystalline phases as HER cocatalysts in Si-based PEC application. Park et al. explained the role of S content on HER activity, where photocathodes fabricated through growing NiS and $NiS_{1.97}$ nanocrystals on Si NWs, respectively.[76] The NiS/Si yielded a V_{on} of 0.2 V_{RHE} and a photocurrent density of 10 mA cm^{-2} at 0 V_{RHE} in both acid and alkaline electrolytes, outperforming the Si-$NiS_{1.97}$ photocathode. Moreover, a thin film of cubic-NiP_2 synthesized on textured pn^+-Si/Ti photocathode exhibits a great V_{on} of 0.41 V_{RHE} and a photocurrent of about 12 mA cm^{-2} at 0 V_{RHE} in 0.5 M H_2SO_4.[77] Also, operation stability of 6 h can be achieved in both acidic and neutral (pH 9.5) electrolytes. Therefore, it can be found from the above discussion that: 1) among metal compounds, MoS_2 shows exceptionally excellent HER catalytic activity due to its inherent 2D structure with more edge S active sites through exfoliation or doping, 2) the catalytic performances of both Ni- and Co-based cocatalysts for Si photocathodes are weaker than that of MoS_2, mainly reflected in the lower photocurrent.

1.3.3.3 Bimetal compounds

Although monometallic compounds have been used as cocatalysts to effectively improve the sluggish PEC-HER kinetics of Si photocathodes, great efforts are also being made to find earth-abundant and highly active bimetallic HER cocatalysts. This is mainly attributed to the bimetallic catalysts with structural defects, increased active sites, and enhanced conductivity. A previous study reported on adapting the photo-assisted electrodeposition method for amorphous bimetallic $CoMoS_x$ onto planar Si photocathode (Figure 1.10a) by Wong and coworkers, which showed enhanced PEC-HER performance (a V_{on} of 0.25 V_{RHE} and a photocurrent density of −17.5 mA cm^{-2} at 0 V_{RHE} in pH 4.25 solution) compared with a MoS_x/Si photocathode prepared under comparable conditions.[78] The authors found that the $CoMoS_x$ layer displays better electron capture and transfer capabilities as well as enhanced HER catalytic activity than the MoS_x equivalent. Similar to $CoMoS_x$, the $NiCoSe_x$ obtained by photo-assisted electrodeposition on an p-Si nanopillar (NP) array (Figure 1.10b-d) maximizes the utilization of light-harvesting and photogenerated electrons.[79] The photocurrent (−37.5 mA cm^{-2} at 0 V_{RHE})

of $NiCoSe_x$/Si NP photocathode is superior to that achieved by the $NiSe_x$/Si NP and $CoSe_x$/Si NP photocathodes in 0.5 M H_2SO_4. This result might be ascribed to the synergistic function of Ni and Co in $NiCoSe_x$, in terms of delicate active sites, good optical transparency, and improved electronic structure. Photo-assisted electrodeposited NiCoP was also loaded on modified Si photocathodes with TiO_2 nanorods and N-doped graphene nanolayer (C_N) to greatly enhance the charge transfer efficiency and boost HER kinetics in an alkaline electrolyte.[80] As a consequence, the optimum Si/C_N/TiO_2/NiCoP photocathode exhibited a photocurrent density of −19.87 mA cm^{-2} at 0 V_{RHE} and a V_{on} at 0.42 V_{RHE} in 1.0 M KOH.

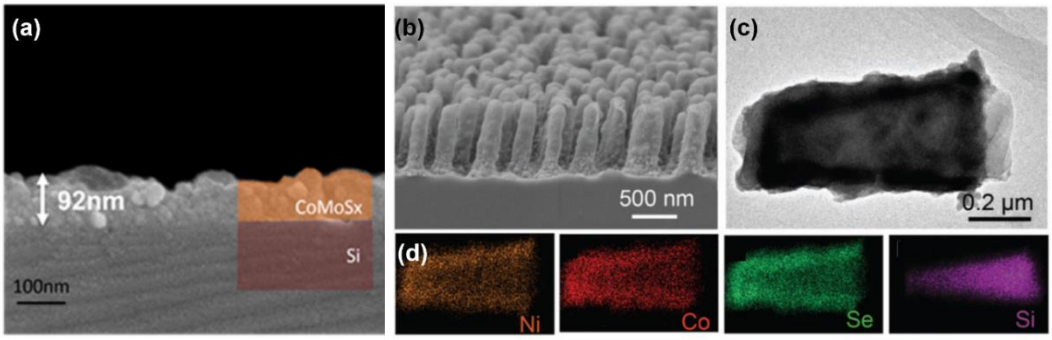

Figure 1.10 (a) SEM image of Si/a-$CoMoS_x$ photocathode.[78] (b) SEM image, (c) TEM image, and (d) elemental mapping images of $NiCoSe_x$/Si NP photoathode.[79]

Besides, Ni-Fe layered double hydroxide (NiFe LDH) is also known for its good stability in the alkaline environment. Zheng et al. deposited NiFe LDH on Ti (5 nm)-coated Si photoabsorbers through hydrothermal method, and the NiFe LDH-catalyzed Si photocathode exhibited a photocurrent of 7 mA cm^{-2} at 0 V_{RHE}, a V_{on} of ~0.3 V_{RHE}, and stability of 24 h in 1.0 M KOH.[81] The efficient alkaline PEC-HER property is credited to the double-layered structure of the deposited NiFe LDH, that is, a dense bottom and a porous surface. The bottom dense layer uniformly covers the underlying Ti/Si substrate with decent interfacial contact for efficient charge transfer and alkaline stability. While the highly porous top layer is composed of interwoven flakes, providing a large contact area with the electrolyte to facilitate surface reaction kinetics. Shen et al. recently reported an impressive alkaline PEC-HER performance using hierarchical MoS_2/Ni_3S_2 cocatalyst by electrodeposition on a Ni-protected Si photocathode. For as-fabricated MoS_2/Ni_3S_2/Ni/Si photocathode, a V_{on} of 0.54 V_{RHE} and an applied bias photon-to-current efficiency of 11.2% were obtained in 1.0 M KOH.[82] The hierarchical MoS_2/Ni_3S_2 structure has higher catalytic activity than MoS_2 or Ni_3S_2 thanks to the strong electronic

interaction and atomic mixing interface between Ni_3S_2 and MoS_2, which can be demonstrated by XPS and DFT calculations, respectively. As a consequence, the $MoS_2/Ni_3S_2/Ni/Si$ photocathode was able to operate at 0 V_{RHE} with saturated current of 41.5 mA cm^{-2} for 172 h.

In comparison with single-metal compound cocatalysts, properly designed bimetal compound cocatalysts can possess synergetic effects of the corresponding individual components, and exhibit better catalytic activity and stability under alkaline conditions. Although a lot of bimetallic electrocatalysts have been developed, there are limited studies on their use in Si-based PEC-HER applications. This is mainly due to the immature integration technology of cocatalysts and Si semiconductors. The above representative reports can exemplify that photo-assisted electrodeposition of cocatalysts is a currently generally efficient and economical method.

1.3.4 Protection/passivation layers for high stability

Exposure of Si surfaces to aqueous electrolytes is sensitive to corrosion and passivation, thereby hindering the transport of photogenerated minority carriers for hydrogen production, and thus a corrosion-resistant protective layer is urgently needed. It is easy to consider that the inherent stability of protective material is one of the key indicators of its protective properties for Si-based photocathodes. When the protective layer material has a more negative self-reduction potential than the photocathode conduction band, the thermodynamic stability can be guaranteed in HER.[30] In addition, other properties of the protective layer, such as electrical conductivity, optical transparency, surface state passivation, and interfacial adhesion to Si are also important factors in evaluating its comprehensive performance. For this purpose, the protective layer is basically produced in a thin film.[83] Generally, noble metal thin films can serve as powerful protection layers for Si-based photocathodes due to their excellent electrical conductivity and intrinsic stability. In recent studies, considering the cost-competitive advantage, non-precious metals, especially Ti and Ni thin films, have become more favored protective layers for Si-based photocathodes. The metal layer has excellent electrical conductivity but poor light transmission, preventing light from reaching the underlying Si substrate. Therefore, transparent conductive metal compound layers have been investigated as alternative protective layers for Si-based photocathodes. CVD and atomic layer deposition (ALD) technologies are usually utilized to get a pinhole-free protective layer to guarantee full coverage of the Si substrate surface.[84]

1.3.4.1 Metal layers

Noble metals have been shown to act as protective layers for Si-based photocathodes due to their outstanding stability, excellent intrinsic conductivity, and simple synthesis process in extreme electrolytes. For instance, Specht et al. reported using Pt as an efficient protective layer and cocatalyst for p-Si photocathodes, achieving impressively stable PEC hydrogen generation over 60 days in the acidic electrolyte.[85] Non-precious metals such as Ti and Ni have also been adopted as alternative functional protection layers. Ti film can be used in either acidic or alkaline electrolytes. Shen et al. used a thin Ti interlayer between an n^+p-Si photoelectrode and the Co-doped WS_2 cocatalyst, achieving 6 days of long-term PEC HER in 1.0 M $HClO_4$.[86] The Ti layer protected the Si surface and reduced charge transfer resistances on the electrode/electrolyte interface. Similarly, Zhang et al. reported a Ti-protected n^+p-Si micropyramids with amorphous NiS_xO_y cocatalyst, obtaining 6 h of PEC HER in 1.0 M KOH.[55] In addition to Ti, Ni is also an attractive interlayer to protect buried junction Si against alkaline corrosion, as it enables good contact with Si and is easily deposited by various techniques. For example, Shen et al. employed a hierarchical MoS_2/Ni_3S_2 cocatalyst on Ni-protected n^+np^+-Si MPy photocathode to display 172-h PEC HER under 41.5 mA cm^{-2} in 1.0 M KOH.[82]

1.3.4.2 Metal oxide layers

Many metallic oxides are well-known to be optically transparent and chemically stable, which paves the way as protection layers for Si-based photocathodes. TiO_2 is stable over a broad pH range from acid to alkaline, along with excellent visible light transmittance due to its large bandgap. Conformal TiO_2 thin films deposited by ALD method have previously been used to stabilize Si-based photocathodes against corrosion in acidic electrolytes.[18, 87] A study by Chorkendorff et al. showed that an ALD-grown TiO_2 (100 nm) protective n^+p Si photocathode could yield a superior durability at 0.3 V_{RHE} for more than 14 days with negligible degradation (<5%) in 1.0 M $HClO_4$ solution.[88] Besides, a 10 nm-thick TiO_2 layer deposited by the e-beam evaporator method was employed as an interface link layer to improve the growth of MoS_2 cocatalyst, and as a passivation layer to suppress the corrosion and oxidation of the Si surface.[89] The $MoS_2/TiO_2/Si$ photocathode attained a continuous 180-h HER operation in 0.5 M H_2SO_4 without noticeable degradation. The broad stability of TiO_2 suggests that it can also be applied to neutral and alkaline electrolytes as confirmed by recent studies. Jang and coworkers

demonstrated a TiO_2 layer grown by ALD effectively passivated the vulnerable InAs/Si heterostructure photocathode, achieving a continuous 20-h HER operation at neutral pH phosphate buffer solution.[64] Zhang et al. fabricated a TiO_2 protected-planar Si photocathode with WP particles cocatalyst and performed PEC hydrogen production under alkaline conditions (**Figure 1.11**a).[90] The resulting TiO_2 necking layer between cocatalyst and semiconductor can facilitate the electron transfer from Si to TiO_2 and then into the WP particles, as illustrated in Figure 1.11b. The obtained WP/TiO_2/Si produced a saturated photocurrent of −35 mA cm^{-2} and a stability of up to 110 h in 1.0 M KOH. Charge transport resistance is one of the main challenges when using the protective layer, since it must not retard the electron transfer. The doping level of the TiO_2 layer is a vital factor for facile charge transport, which can be adjusted during annealing process in vacuum to obtain the appropriate concentration of oxygen defects. For example, using crystalline TiO_2 with graded oxygen defects as protective layer and Pd nanospheres as cocatalyst, Wang and colleagues presented a saturation photocurrent of about 35.3 mA cm^{-2} for black Si photocathodes in 1.0 M NaOH (Figure 1.11c).[91] The high efficiency benefits from the oxygen defects allowing the quick carrier transport. Moreover, the fabricated Si photocathodes exhibited excellent durability of over 100 h at 10 mA cm^{-2} in both alkaline and acid conditions (Figure 1.11d).

Alternatively, other thin metallic oxide insulators, such as native SiO_x, Al_2O_3, $SrTiO_3$, and Ta_2O_5, can be used as protection layers. In general, native SiO_x is removed from Si surface to form stable Si with low surface defects prior to the cocatalyst coating. However, the controlled SiO_x layer can also serve as a functional protective layer.[20] For example, Das and coworkers reported that a native SiO_x interlayer formed by HF etching can defend the Si from further oxidation during the ALD growth of TiO_2 cocatalyst.[92] Lee et al. also adopted SiO_2 layer grown on the Si as a passivation layer by high-temperature rapid thermal oxidation under atmospheric conditions.[93] It should be noted that the series resistance at the SiO_2 tunnelling layer is detrimental to the charge transfer kinetics. Alternatively, Al_2O_3 is a well reported tunnelling insulator that can be adopted as a passivation layer for corrosion-resistant Si-based photocathodes, while the photogenerated electrons can be able to tunnel through.[30] Shen et al. demonstrated a micropyramid-Si photocathode protected by a 4.5 nm ALD-grown Al_2O_3 layer, which performed a 100 h long stable PEC hydrogen evolution in pH 1 electrolyte.[94] They further reduced the thickness of Al_2O_3 to ~2 nm, which not only protects the Si photocathode,

but also exhibits excellent adhesion between the Si semiconductor and the MoS_2 cocatalyst.[68] As a result, a V_{on} of 0.4 V_{RHE} and a superior PEC-HER stability up to 120 h with the photocurrent of 35.6 mA cm^{-2} in 1.0 M $HClO_4$ were obtained for the as-fabricated $MoS_2/Al_2O_3/n^+p$-Si photocathode. Moreover, Ji and coworkers proposed that a thin epitaxial layer of $SrTiO_3$ directly grown on Si with a small lattice match of −1.7% (Si: 3.84 Å and $SrTiO_3$: 3.905 Å) could greatly enhance the photogenerated electron transport, as the conduction band-offset at the Si/$SrTiO_3$ interface was found to be near zero.[95] Inspired by this, Ghosh et al. fabricated a Ta_2O_5-protected Si nanowire photoelectrode, and the introduction of the Ta_2O_5 passivation layer with the low conduction band offset and the negligible lattice mismatch interface effectively facilitated the charge transfer from Si to the electrolyte, thus supporting large photocurrent of −49.5 mA cm^{-2}.[96]

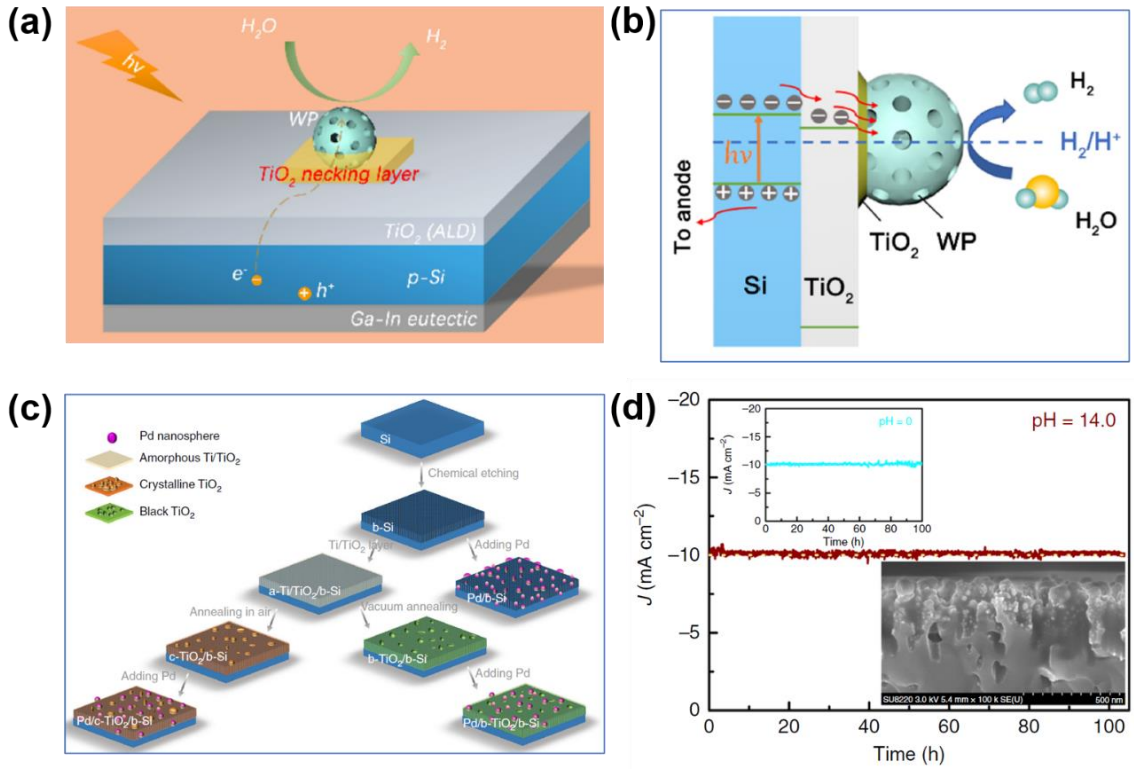

Figure 1.11 (a) Configuration and (b) carrier-transfer mechanism of WP/TiO_2/Si.[90] (c) Schematic diagram of strategies to protect black Si photocathodes, (d) chronoamperometry curves of Pd/b_2-TiO_2/Si held at −0.012 V_{RHE} in 1.0 M NaOH and at −0.124 V_{RHE} in 0.5 M H_2SO_4 (upper-left inset), and the cross-sectional FESEM image of photocathode after 100-h durability test (bottom-right inset).[91]

1.3.4.3 Other layers

Many other materials including MoS_2, carbon[97], GaN, glass layer[98], Si_xN[99], etc., have

also been exploited as protection layer, especially the chemically stable transition metal dichalcogenides. In addition to the HER catalytic activity of MoS_2, it has been previously demonstrated to simultaneously achieve anti-corrosion stability in acidic electrolytes. Layer structure of MoS_2 benefit to fabricate mono or few atomic layers, which have superior electron conductivity and weak inherent light absorption. Chorkendorff et al. designed a MoS_2-protected n^+p-Si photocathode, showing only minor variations after running at 0 V_{RHE} for at least 5 days in 1.0 M $HClO_4$ solution.[100] The resulting MoS_2 layer grown by sputtering Mo onto Si acts as both a protection layer and a HER cocatalyst. In addition to transition metal chalcogenides, GaN has also emerged as an effective protection layer. For example, Mi et al. demonstrated that a photocathode by integrating an n^+p-Si with Pt-decorated N-rich GaN nanostructure exhibited an high stability of 3000 h over 35 mA cm^{-2} in 0.5 M H_2SO_4.[101] The nearly perfect conduction band configuration at GaN/Si heterointerface could enable efficiently extract photogenerated electrons, and the N-rich GaN nanostructures could effectively protect the Si from chemical and photocorrosion.

To date, various types of Si-based protective layers have been evaluated. Among them, metal protective layers with excellent conductivity are also accompanied by the problem of parasitic light absorption, while the chemical stability of TiO_2 over a wide pH range from acidic to basic is particularly prominent in the oxide protective layers. In particular, investigating compatible interfaces created by adding other functional protection layers between Si and HER cocatalyst to minimize carrier loss and maximize photocurrent may also be promising candidates.

1.4 Thesis motivations and organization

Solar-driven PEC water splitting into hydrogen fuel is a promising avenue for renewable energy conversion to overcome energy crises and environmental concerns. On the basis of the above-mentioned overview, the solar-to-hydrogen conversion efficiency of the Si-based PEC system can be controlled by four critical criteria: light-harvesting capability, interface charge transfer, surface HER kinetics, and stability. In this concern, in order to construct a robust Si-based photocathode system for efficient PEC HER, great research efforts should be devoted into the following three aspects: (1) utilizing the Si semiconductor with suitable band structure as prototypes for photocathodes to achieve excellent light absorption; (2) rational design and optimization of suitable HER cocatalysts with numerous active sites for high photovoltage; (3) interface modulation

between the semiconductor and the cocatalyst for rapid charge-transfer kinetics and robust stability.

Therefore, in this thesis, the object mainly focuses on the rational surface/interface engineering strategies over planar p-type Si-based photocathodes towards a highly-efficient and sustainable hydrogen production. Three strategies have been considered for Si-based photocathodes to improve catalytic activity, including the surface modification of Si semiconductors, the selection and optimization of cocatalysts, and the interface engineering between Si semiconductors and cocatalysts. First, a Si junction structure is designed and fabricated by modifying Si surface with another functional semiconductor (amorphous Si) with more favorable band alignment to enhance the light utilization and accelerate the outward migration of photogenerated carriers. Then, cost-effective HER cocatalysts based on earth-abundant metal elements are explored and investigated as better alternatives to noble metal cocatalysts for practical PEC applications. Finally, the insertion of a protection layer at the interface between the Si and the cocatalyst is proposed to optimize the charge transfer and durability of the photocathode, thereby further expanding the PEC-HER application under alkaline conditions. This dissertation is divided into five chapters. A summary of the remaining four chapters is described as below:

Chapter 2 Construction of buried a-Si/c-Si junction photocathodes for boosting photoelectrochemical hydrogen production

As a photocathode for PEC HER, the performance of crystal Si (c-Si) has been crucially limited by inert surface activity, inherent oxidation and photo-corrosion, which lead to sluggish reaction kinetics and severe charge recombination for photo-assisted hydrogen evolution. Notably, loading hydrogen evolution cocatalysts has been regarded as a typically effective approach to enhance the surface reaction kinetics of Si. Pt has been shown to be the most efficient HER electrocatalyst. However, since Pt has a large work function that is more negative than the Fermi level of p-type c-Si, direct loading on the Si surface will form an upward electron transfer barrier and make the electron transfer slow. This problem can be solved by introducing an amorphous Si (a-Si) layer to modify the c-Si surface with reasonable band barriers, but usually using complex and high temperature fabrication processes. In this chapter, a mild solution processed a-Si/c-Si junction photocathode with the co-deposition of Pt nanoparticles was designed to achieve facile electron transfer. The a-Si layer within Pt/a-Si/c-Si can not only act as an electron transfer

mediator but also as a good passivation layer, producing a high-quality a-Si/c-Si buried junction for enhanced photovoltage and photocurrent response. Simultaneously, the large band shift at the a-Si/c-Si interface provides a bulti-in electric field with an additional force, which could suppress carrier recombination and ensures efficient charge transfer. In addition, the a-Si layer serves as the growth substrate of the cocatalyst, which could effectively modulate the size and distribution of Pt nanoparticles to be smaller and more uniform. This feasible manner based on the construction of surface Si junction structures was expected to improve the photoresponse of Si-based photocathodes for enhanced PEC-HER performance.

Chapter 3 Engineering heterogeneous NiS_2/NiS cocatalysts with progressive electron transfer from planar p-Si Photocathodes for solar hydrogen evolution

Targeting inert active sites on bare Si surfaces, supported cocatalysts have been shown to be an effective strategy to improve surface reaction kinetics and lower the activation energy for HER. Compared with noble metal cocatalysts, cost-effective HER cocatalysts based on earth-abundant metal elements are better choices for practical PEC-HER applications. Meanwhile, numerous heterogeneous structure cocatalysts have shown superior HER activity due to the synergetic effects induced by the mono-component counterparts. Furthermore, the optimization of the cocatalyst is also an alternative approach to junction structures to ensure efficient band bending and electron transfer. Based on this, transition metal sulfides are promising to realize such heterogeneous structures because they comprise various forms of compounds that possess tunable chemical and physical properties. In this chapter, a NiS_2/NiS heterojunction (NNH) was prepared in-situ and applied to a planar p-type Si (p-Si) substrate as a cocatalyst to achieve progressive electron transfer. The cocatalyst NNH could play bifunctional roles on planar p-Si, in which the photogenerated electrons could rapidly transfer from the planar p-Si to NiS phase within NNH as progressive media to promote electron transfer, and then smoothly transfer to defect-rich NiS_2 phase within NNH acting as the key cocatalyst rich in the active sites. It can be expected that the proposed heterogeneous metal sulfides cocatalysts could efficiently enhance the PEC performance on the Si photoelectrodes with progressive electron transfer.

Chapter 4 A synergetic strategy to construct anti-reflective and anti-corrosive Co-P/WS_x/Si photocathode for durable hydrogen evolution in alkaline condition

In PEC water splitting, two half-reactions of HER at the photocathode and oxygen

evolution (OER) at the photoanode are generally carried out in highly acidic and alkaline solutions, respectively. The development of commercially applicable Si-based photocathodes for durable PEC HER in alkaline electrolytes is attracting attention because OER requires a higher overpotential to cope with slower kinetics in acid than HER. Since alkaline solutions can cause severe Si etching, there is a great need to develop an appropriate Si protection layer that not only balances the trade-off between alkalic corrosion resistance and light transmittance but matches earth-abundant cocatalysts. Similar concerns about optical impacts also apply to cocatalysts, which require cocatalysts to preserve high catalytic activity while ensuring light penetration into the underneath Si. In this chapter, a synergetic strategy is proposed to deposit an anti-reflective Co-P cocatalyst on a WS_x-stabilized planar p-Si photocathode for efficient and stable PEC-HER performance in an alkaline solution. The introduction of the self-assembled WS_x thin film plays a vital role in supporting the alkali-corrosion resistance of Si semiconductor and providing a nucleation base for Co-P cocatalysts, which forms a robust structure and promotes the electron transfer from Si to Co-P. Meanwhile, the morphology of Co-P cocatalyst could be modulated by the controllable WS_x to possess an anti-reflective effect while maintaining excellent catalytic activity. The complementary integration of Co-P/WSx/Si photocathode were expected to exhibit superior catalytic properties in alkaline media through the synergetic integration of anti-corrosive interlayer and anti-reflective cocatalyst.

Chapter 5 General conclusions and future prospects

This chapter presents an overall summary and conclusion of this dissertation and gives the prospects for future work.

References

1. IEA, Global CO_2 emissions rebounded to their highest level in history in 2021, **2022**.
2. M.Z. Rahman, M.G. Kibria, C.B. Mullins, Metal-free photocatalysts for hydrogen evolution. *Chem. Soc. Rev.,* **2020**, *49* (6), 1887-1931.
3. L. Schlapbach, A. Züttel, Hydrogen-storage materials for mobile applications, *Materials for Sustainable Energy*, **2010**, 265-270.
4. A. Fujishima, K. Honda, Electrochemical Photolysis of Water at a Semiconductor Electrode. *Nature,* **1972**, *238* (5358), 37-38.
5. A. Jena, C.-J. Chen, H. Chang, S.-F. Hu, R.-S. Liu, Comprehensive view on recent

developments in hydrogen evolution using MoS_2 on a Si photocathode: from electronic to electrochemical aspects. *J. Mater. Chem. A,* **2021**, *9* (7), 3767-3785.

6. Y. Yang, S. Niu, D. Han, T. Liu, G. Wang, Y. Li, Progress in Developing Metal Oxide Nanomaterials for Photoelectrochemical Water Splitting. *Adv. Energy Mater.,* **2017**, *7* (19), 1700555.
7. S. Kment, F. Riboni, S. Pausova, L. Wang, L. Wang, H. Han, Z. Hubicka, J. Krysa, P. Schmuki, R. Zboril, Photoanodes based on TiO_2 and α-Fe_2O_3 for solar water splitting – superior role of 1D nanoarchitectures and of combined heterostructures. *Chem. Soc. Rev.,* **2017**, *46* (12), 3716-3769.
8. G. Wang, Y. Ling, H. Wang, L. Xihong, Y. Li, Chemically modified nanostructures for photoelectrochemical water splitting. *Journal of Photochemistry and Photobiology C: Photochemistry Reviews,* **2014**, *19*, 35-51.
9. M.G. Walter, E.L. Warren, J.R. McKone, S.W. Boettcher, Q. Mi, E.A. Santori, N.S. Lewis, Solar Water Splitting Cells. *Chem. Rev.,* **2010**, *110* (11), 6446-6473.
10. J.H. Kim, J.S. Lee, Elaborately modified BiVO4 photoanodes for solar water splitting. *Adv. Mater.,* **2019**, *31* (20), 1806938.
11. K. Park, Y.J. Kim, T. Yoon, S. David, Y.M. Song, A methodological review on material growth and synthesis of solar-driven water splitting photoelectrochemical cells. *RSC Adv.,* **2019**, *9* (52), 30112-30124.
12. T.J. Jacobsson, V. Fjällström, M. Edoff, T. Edvinsson, A theoretical analysis of optical absorption limits and performance of tandem devices and series interconnected architectures for solar hydrogen production. *Sol. Energy Mater Sol. Cells,* **2015**, *138*, 86-95.
13. J. Brillet, J.-H. Yum, M. Cornuz, T. Hisatomi, R. Solarska, J. Augustynski, M. Graetzel, K. Sivula, Highly efficient water splitting by a dual-absorber tandem cell. *Nat. Photonics,* **2012**, *6* (12), 824-828.
14. L.M. Peter, K.G. Upul Wijayantha, Photoelectrochemical Water Splitting at Semiconductor Electrodes: Fundamental Problems and New Perspectives. *ChemPhysChem,* **2014**, *15* (10), 1983-1995.
15. J.-W. Schüttauf, M.A. Modestino, E. Chinello, D. Lambelet, A. Delfino, D. Dominé, A. Faes, M. Despeisse, J. Bailat, D. Psaltis, C. Moser, C. Ballif, Solar-to-Hydrogen Production at 14.2% Efficiency with Silicon Photovoltaics and Earth-Abundant

Electrocatalysts. *J. Electrochem. Soc.,* **2016**, *163* (10), F1177-F1181.

16. A.G. Tamirat, J. Rick, A.A. Dubale, W.-N. Su, B.-J. Hwang, Using hematite for photoelectrochemical water splitting: a review of current progress and challenges. *Nanoscale Horiz.,* **2016**, *1* (4), 243-267.
17. H.-P. Wang, K. Sun, S.Y. Noh, A. Kargar, M.-L. Tsai, M.-Y. Huang, D. Wang, J.-H. He, High-Performance a-Si/c-Si Heterojunction Photoelectrodes for Photoelectrochemical Oxygen and Hydrogen Evolution. *Nano Lett.,* **2015**, *15* (5), 2817-2824.
18. R. Fan, W. Dong, L. Fang, F. Zheng, M. Shen, More than 10% efficiency and one-week stability of Si photocathodes for water splitting by manipulating the loading of the Pt catalyst and TiO_2 protective layer. *J. Mater. Chem. A,* **2017**, *5* (35), 18744-18751.
19. H. Neergaard Waltenburg, J. Yates, Surface Chemistry of Silicon. *Chem. Rev.,* **1995**, *95* (5), 1589-1673.
20. K. Sun, S. Shen, Y. Liang, P.E. Burrows, S.S. Mao, D. Wang, Enabling Silicon for Solar-Fuel Production. *Chem. Rev.,* **2014**, *114* (17), 8662-8719.
21. S.A. Lee, S. Choi, C. Kim, J.W. Yang, S.Y. Kim, H.W. Jang, Si-Based Water Oxidation Photoanodes Conjugated with Earth-Abundant Transition Metal-Based Catalysts. *ACS Mater. Lett.,* **2020**, *2* (1), 107-126.
22. Z. Luo, T. Wang, J. Gong, Single-crystal silicon-based electrodes for unbiased solar water splitting: current status and prospects. *Chem. Soc. Rev.,* **2019**, *48* (7), 2158-2181.
23. D. Zhang, J. Shi, W. Zi, P. Wang, S. Liu, Recent Advances in Photoelectrochemical Applications of Silicon Materials for Solar-to-Chemicals Conversion. *ChemSusChem,* **2017**, *10* (22), 4324-4341.
24. R.N. Dominey, N.S. Lewis, J.A. Bruce, D.C. Bookbinder, M.S. Wrighton, Improvement of photoelectrochemical hydrogen generation by surface modification of p-type silicon semiconductor photocathodes. *J. Am. Chem. Soc.,* **1982**, *104* (2), 467-482.
25. J. Joe, H. Yang, C. Bae, H. Shin, Metal Chalcogenides on Silicon Photocathodes for Efficient Water Splitting: A Mini Overview. *Catalysts,* **2019**, *9* (2).
26. M.B. Raschke, U. Höfer, Chemisorption energy of hydrogen on silicon surfaces.

Phys. Rev. B, **2001**, *63* (20), 201303.

27. S. Trasatti, Work function, electronegativity, and electrochemical behaviour of metals: III. Electrolytic hydrogen evolution in acid solutions. *J. Electroanal. Chem. Interf. Electrochem.,* **1972**, *39* (1), 163-184.

28. A.R. Zeradjanin, J.-P. Grote, G. Polymeros, K.J.J. Mayrhofer, A Critical Review on Hydrogen Evolution Electrocatalysis: Re-exploring the Volcano-relationship. *Electroanalysis,* **2016**, *28* (10), 2256-2269.

29. S. Chen, L.-W. Wang, Thermodynamic Oxidation and Reduction Potentials of Photocatalytic Semiconductors in Aqueous Solution. *Chem. Mater.,* **2012**, *24* (18), 3659-3666.

30. D. Bae, B. Seger, P.C.K. Vesborg, O. Hansen, I. Chorkendorff, Strategies for stable water splitting via protected photoelectrodes. *Chem. Soc. Rev.,* **2017**, *46* (7), 1933-1954.

31. C. Jiang, S.J.A. Moniz, A. Wang, T. Zhang, J. Tang, Photoelectrochemical devices for solar water splitting – materials and challenges. *Chem. Soc. Rev.,* **2017**, *46* (15), 4645-4660.

32. D. Li, J. Shi, C. Li, Transition-Metal-Based Electrocatalysts as Cocatalysts for Photoelectrochemical Water Splitting: A Mini Review. *Small,* **2018**, *14* (23), 1704179.

33. Q. Ding, B. Song, P. Xu, S. Jin, Efficient Electrocatalytic and Photoelectrochemical Hydrogen Generation Using MoS_2 and Related Compounds. *Chem,* **2016**, *1* (5), 699-726.

34. C. Ding, J. Shi, Z. Wang, C. Li, Correction to Photoelectrocatalytic Water Splitting: Significance of Cocatalysts, Electrolyte, and Interfaces. *ACS Catal.,* **2017**, *7* (3), 1706-1706.

35. Q. Wang, C. Pornrungroj, S. Linley, E. Reisner, Strategies to improve light utilization in solar fuel synthesis. *Nat. Energy,* **2022**, *7* (1), 13-24.

36. S. Chandrasekaran, T. Nann, N.H. Voelcker, Nanostructured silicon photoelectrodes for solar water electrolysis. *Nano Energy,* **2015**, *17*, 308-322.

37. D. Liu, J. Ma, R. Long, C. Gao, Y. Xiong, Silicon nanostructures for solar-driven catalytic applications. *Nano Today,* **2017**, *17*, 96-116.

38. Y. Tian, N. Li, M. Bonifazi, A. Fratalocchi, Harnessing complex photonic systems for renewable energy. *Advances in Physics: X,* **2020**, *5* (1), 1768898.

39. L. Zhang, X. Chen, Z. Hao, X. Chen, Y. Li, Y. Cui, C. Yuan, H. Ge, TiO_2/Au Nanoring/p-Si Nanohole Photocathode for Hydrogen Generation. *ACS Appl. Nano Mater.,* **2019**, *2* (6), 3654-3661.

40. M. Lublow, B. Bouabadi, S. Kubala, Au–Pt core–shell nanoemitters on silicon for photoelectrochemical solar energy conversion. *Sol. Energy Mater Sol. Cells,* **2012**, *107*, 56-62.

41. S. Gopalakrishnan, K. Jeganathan, Facile fabrication of silicon nanowires as photocathode for visible-light induced photoelectrochemical water splitting. *Int. J. Hydrogen Energy,* **2017**, *42* (36), 22671-22676.

42. U. Sim, H.-Y. Jeong, T.-Y. Yang, K.T. Nam, Nanostructural dependence of hydrogen production in silicon photocathodes. *J. Mater. Chem. A,* **2013**, *1* (17), 5414-5422.

43. S.M. Thalluri, J. Borme, D. Xiong, J. Xu, W. Li, I. Amorim, P. Alpuim, J. Gaspar, H. Fonseca, L. Qiao, L. Liu, Highly-ordered silicon nanowire arrays for photoelectrochemical hydrogen evolution: an investigation on the effect of wire diameter, length and inter-wire spacing. *Sustain. Energ. Fuels,* **2018**, *2* (5), 978-982.

44. H. Yidong, C.V. Peter, B. Lone, S. Brian, D. Søren, C. Ib, L.A. Billie, H. Konrad, B. Marten, R. Jan, K.N. Jens, P. Thomas, H. Ole, Photoelectrocatalysis and electrocatalysis on silicon electrodes decorated with cubane-like clusters. *J. Photonics Energy,* **2012**, *2* (1), 1-17.

45. Q. Ding, J. Zhai, M. Cabán-Acevedo, M.J. Shearer, L. Li, H.-C. Chang, M.-L. Tsai, D. Ma, X. Zhang, R.J. Hamers, J.-H. He, S. Jin, Designing Efficient Solar-Driven Hydrogen Evolution Photocathodes Using Semitransparent MoQ_xCl_y (Q = S, Se) Catalysts on Si Micropyramids. *Adv. Mater.,* **2015**, *27* (41), 6511-6518.

46. S. Zhao, G. Yuan, Q. Wang, W. Liu, R. Wang, S. Yang, Quasi-hydrophilic black silicon photocathodes with inverted pyramid arrays for enhanced hydrogen generation. *Nanoscale,* **2020**, *12* (1), 316-325.

47. P.P. Kunturu, C. Zachariadis, L. Witczak, M.D. Nguyen, G. Rijnders, J. Huskens, Tandem Si Micropillar Array Photocathodes with Conformal Copper Oxide and a Protection Layer by Pulsed Laser Deposition. *ACS Appl. Mater. Interfaces,* **2019**, *11* (44), 41402-41414.

48. S. Huang, H. Zhang, Z. Wu, D. Kong, D. Lin, Y. Fan, X. Yang, Z. Zhong, S. Huang, Z. Jiang, C. Cheng, Large-Area Ordered P-type Si Nanowire Arrays as Photocathode for Highly Efficient Photoelectrochemical Hydrogen Generation. *ACS Appl. Mater. Interfaces,* **2014**, *6* (15), 12111-12118.

49. C.-W. Tung, C.-H. Hou, H.-T. Lin, Y. Zheng, Y.-P. Huang, Y.-F. Liao, J.-J. Shiue, H.M. Chen, In situ Observation of Electrodeposited Bimetallic p-Si Micropillar Array Photocathode for Solar-Driven Hydrogen Evolution. *Solar RRL,* **2020**, *4* (8), 2000028.

50. J.-Y. Jung, M.J. Choi, K. Zhou, X. Li, S.-W. Jee, H.-D. Um, M.-J. Park, K.-T. Park, J.H. Bang, J.-H. Lee, Photoelectrochemical water splitting employing a tapered silicon nanohole array. *J. Mater. Chem. A,* **2014**, *2* (3), 833-842.

51. T. Han, S. Privitera, R.G. Milazzo, C. Bongiorno, S. Di Franco, F. La Via, X. Song, Y. Shi, M. Lanza, S. Lombardo, Photo-electrochemical water splitting in silicon based photocathodes enhanced by plasmonic/catalytic nanostructures. *Mat. Sci. Eng. B,* **2017**, *225*, 128-133.

52. C.-J. Chen, M.-G. Chen, C.K. Chen, P.C. Wu, P.-T. Chen, M. Basu, S.-F. Hu, D.P. Tsai, R.-S. Liu, Ag–Si artificial microflowers for plasmon-enhanced solar water splitting. *Chem. Commun.,* **2015**, *51* (3), 549-552.

53. T. Zhu, M.N. Chong, Prospects of metal–insulator–semiconductor (MIS) nanojunction structures for enhanced hydrogen evolution in photoelectrochemical cells: A review. *Nano Energy,* **2015**, *12*, 347-373.

54. F. Zhang, X. Yu, J. Hu, L. Lei, Y. He, X. Zhang, Coupling Ru-MoS_2 heterostructure with silicon for efficient photoelectrocatalytic water splitting. *Chem. Eng. J.,* **2021**, *423*, 130231.

55. Q. Jia, C. Yu, W. Liu, G. Zheng, C. Lei, L. Lei, X. Zhang, High performance n^+p-Si/Ti/NiS_xO_y photocathode for photoelectrochemical hydrogen evolution in alkaline solution. *J. Energy Chem. ,* **2019**, *30*, 101-107.

56. D. Bae, T. Pedersen, B. Seger, M. Malizia, A. Kuznetsov, O. Hansen, I. Chorkendorff, P.C.K. Vesborg, Back-illuminated Si photocathode: a combined experimental and theoretical study for photocatalytic hydrogen evolution. *Energy Environ. Sci. ,* **2015**, *8* (2), 650-660.

57. M. Cabán-Acevedo, M.L. Stone, J.R. Schmidt, J.G. Thomas, Q. Ding, H.-C. Chang,

M.-L. Tsai, J.-H. He, S. Jin, Efficient hydrogen evolution catalysis using ternary pyrite-type cobalt phosphosulphide. *Nat. Mater.,* **2015**, *14* (12), 1245-1251.

58. R. Fan, S. Cheng, G. Huang, Y. Wang, Y. Zhang, S. Vanka, G.A. Botton, Z. Mi, M. Shen, Unassisted solar water splitting with 9.8% efficiency and over 100 h stability based on Si solar cells and photoelectrodes catalyzed by bifunctional Ni–Mo/Ni. *J. Mater. Chem. A,* **2019**, *7* (5), 2200-2209.

59. B. Liu, S. Feng, L. Yang, C. Li, Z. Luo, T. Wang, J. Gong, Bifacial passivation of n-silicon metal–insulator–semiconductor photoelectrodes for efficient oxygen and hydrogen evolution reactions. *Energy Environ. Sci. ,* **2020**, *13* (1), 221-228.

60. N.Y. Labrador, X. Li, Y. Liu, H. Tan, R. Wang, J.T. Koberstein, T.P. Moffat, D.V. Esposito, Enhanced Performance of Si MIS Photocathodes Containing Oxide-Coated Nanoparticle Electrocatalysts. *Nano Lett.,* **2016**, *16* (10), 6452-6459.

61. D.V. Esposito, I. Levin, T.P. Moffat, A.A. Talin, H_2 evolution at Si-based metal–insulator–semiconductor photoelectrodes enhanced by inversion channel charge collection and H spillover. *Nat. Mater.,* **2013**, *12* (6), 562-568.

62. S. Vanka, B. Zhou, R.A. Awni, Z. Song, F.A. Chowdhury, X. Liu, H. Hajibabaei, W. Shi, Y. Xiao, I.A. Navid, A. Pandey, R. Chen, G.A. Botton, T.W. Hamann, D. Wang, Y. Yan, Z. Mi, InGaN/Si Double-Junction Photocathode for Unassisted Solar Water Splitting. *ACS Energy Lett.,* **2020**, *5* (12), 3741-3751.

63. S. Liu, Z. Luo, L. Li, H. Li, M. Chen, T. Wang, J. Gong, Multifunctional TiO_2 overlayer for p-Si/n-CdS heterojunction photocathode with improved efficiency and stability. *Nano Energy,* **2018**, *53*, 125-129.

64. S. Choi, J. Hwang, T.H. Lee, H.-H. Kim, S.-P. Hong, C. Kim, M.-J. Choi, H.K. Park, S.S.M. Bhat, J.M. Suh, J. Lee, K.S. Choi, S.-H. Hong, J.C. Shin, H.W. Jang, Photoelectrochemical hydrogen production at neutral pH phosphate buffer solution using TiO_2 passivated InAs Nanowire/p-Si heterostructure photocathode. *Chem. Eng. J.,* **2020**, *392*, 123688.

65. C. Yu, Q. Jia, H. Zhang, W. Liu, X. Yu, X. Zhang, Enhancing photoelectrochemical hydrogen production of a n^+p-Si hetero-junction photocathode with amorphous Ni and Ti layers. *Inorg. Chem. Front.,* **2019**, *6* (2), 527-532.

66. W. Vijselaar, P. Westerik, J. Veerbeek, R.M. Tiggelaar, E. Berenschot, N.R. Tas, H. Gardeniers, J. Huskens, Spatial decoupling of light absorption and catalytic activity

of Ni–Mo-loaded high-aspect-ratio silicon microwire photocathodes. *Nat. Energy,* **2018**, *3* (3), 185-192.

67. J.D. Benck, S.C. Lee, K.D. Fong, J. Kibsgaard, R. Sinclair, T.F. Jaramillo, Designing Active and Stable Silicon Photocathodes for Solar Hydrogen Production Using Molybdenum Sulfide Nanomaterials. *Adv. Energy Mater.,* **2014**, *4* (18), 1400739.

68. R. Fan, J. Mao, Z. Yin, J. Jie, W. Dong, L. Fang, F. Zheng, M. Shen, Efficient and Stable Silicon Photocathodes Coated with Vertically Standing Nano-MoS_2 Films for Solar Hydrogen Production. *ACS Appl. Mater. Interfaces,* **2017**, *9* (7), 6123-6129.

69. Q. Ding, F. Meng, C.R. English, M. Cabán-Acevedo, M.J. Shearer, D. Liang, A.S. Daniel, R.J. Hamers, S. Jin, Efficient Photoelectrochemical Hydrogen Generation Using Heterostructures of Si and Chemically Exfoliated Metallic MoS_2. *J. Am. Chem. Soc.,* **2014**, *136*, 8504.

70. M.A. Lukowski, A.S. Daniel, F. Meng, A. Forticaux, L. Li, S. Jin, Enhanced Hydrogen Evolution Catalysis from Chemically Exfoliated Metallic MoS_2 Nanosheets. *J. Am. Chem. Soc.,* **2013**, *135* (28), 10274-10277.

71. H. Lin, S. Li, G. Yang, K. Zhang, D. Tang, Y. Su, Y. Li, S. Luo, K. Chang, J. Ye, In Situ Assembly of MoS_x Thin-Film through Self-Reduction on p-Si for Drastic Enhancement of Photoelectrochemical Hydrogen Evolution. *Adv. Funct. Mater.,* **2021**, *31* (3), 2007071.

72. C.-J. Chen, P.-T. Chen, M. Basu, K.-C. Yang, Y.-R. Lu, C.-L. Dong, C.-G. Ma, C.-C. Shen, S.-F. Hu, R.-S. Liu, An integrated cobalt disulfide (CoS_2) co-catalyst passivation layer on silicon microwires for photoelectrochemical hydrogen evolution. *J. Mater. Chem. A,* **2015**, *3* (46), 23466-23476.

73. C.-J. Chen, C.-W. Liu, K.-C. Yang, L.-C. Yin, D.-H. Wei, S.-F. Hu, R.-S. Liu, Amorphous Phosphorus-Doped Cobalt Sulfide Modified on Silicon Pyramids for Efficient Solar Water Reduction. *ACS Appl. Mater. Interfaces,* **2018**, *10* (43), 37142-37149.

74. T.R. Hellstern, J.D. Benck, J. Kibsgaard, C. Hahn, T.F. Jaramillo, Engineering Cobalt Phosphide (CoP) Thin Film Catalysts for Enhanced Hydrogen Evolution Activity on Silicon Photocathodes. *Adv. Energy Mater.,* **2016**, *6* (4), 1501758.

75. H. Li, P. Wen, D.S. Itanze, M.W. Kim, S. Adhikari, C. Lu, L. Jiang, Y. Qiu, S.M. Geyer, Phosphorus-Rich Colloidal Cobalt Diphosphide (CoP_2) Nanocrystals for

Electrochemical and Photoelectrochemical Hydrogen Evolution. *Adv. Mater.,* **2019**, *31* (24), 1900813.

76. J. Yoo, I.H. Kwak, I.S. Kwon, K. Park, D. Kim, J.H. Lee, S.A. Lim, E.H. Cha, J. Park, Nickel sulfide nanocrystals for electrochemical and photoelectrochemical hydrogen generation. *J. Mater. Chem. C,* **2020**, *8* (9), 3240-3247.

77. F. Chen, Q. Zhu, Y. Wang, W. Cui, X. Su, Y. Li, Efficient Photoelectrochemical Hydrogen Evolution on Silicon Photocathodes Interfaced with Nanostructured NiP_2 Cocatalyst Films. *ACS Appl. Mater. Interfaces,* **2016**, *8* (45), 31025-31031.

78. Y. Chen, P.D. Tran, P. Boix, Y. Ren, S.Y. Chiam, Z. Li, K. Fu, L.H. Wong, J. Barber, Silicon Decorated with Amorphous Cobalt Molybdenum Sulfide Catalyst as an Efficient Photocathode for Solar Hydrogen Generation. *ACS Nano,* **2015**, *9* (4), 3829-3836.

79. H. Zhang, Q. Ding, D. He, H. Liu, W. Liu, Z. Li, B. Yang, X. Zhang, L. Lei, S. Jin, A p-Si/$NiCoSe_x$ core/shell nanopillar array photocathode for enhanced photoelectrochemical hydrogen production. *Energy Environ. Sci.,* **2016**, *9* (10), 3113-3119.

80. X. Sun, C. Liu, P. Zhang, L. Gong, M. Wang, Interface-engineered silicon photocathodes with a NiCoP catalyst-modified TiO_2 nanorod array outlayer for photoelectrochemical hydrogen production in alkaline solution. *J. Power Sources,* **2021**, *484*, 229272.

81. J. Zhao, L. Cai, H. Li, X. Shi, X. Zheng, Stabilizing Silicon Photocathodes by Solution-Deposited Ni–Fe Layered Double Hydroxide for Efficient Hydrogen Evolution in Alkaline Media. *ACS Energy Lett.,* **2017**, *2* (9), 1939-1946.

82. R. Fan, J. Zhou, W. Xun, S. Cheng, S. Vanka, T. Cai, S. Ju, Z. Mi, M. Shen, Highly efficient and stable Si photocathode with hierarchical MoS_2/Ni_3S_2 catalyst for solar hydrogen production in alkaline media. *Nano Energy,* **2020**, *71*, 104631.

83. C. Ros, T. Andreu, J.R. Morante, Photoelectrochemical water splitting: a road from stable metal oxides to protected thin film solar cells. *J. Mater. Chem. A,* **2020**, *8* (21), 10625-10669.

84. A.T. Sivagurunathan, S. Adhikari, D.-H. Kim, Strategies and implications of atomic layer deposition in photoelectrochemical water splitting: Recent advances and prospects. *Nano Energy,* **2021**, *83*, 105802.

85. C.U. Maier, M. Specht, G. Bilger, Hydrogen evolution on platinum-coated p-silicon photocathodes. *Int. J. Hydrogen Energy,* **1996**, *21* (10), 859-864.

86. R. Fan, G. Huang, Y. Wang, Z. Mi, M. Shen, Efficient n^+p-Si photocathodes for solar H_2 production catalyzed by Co-W-S and stabilized by Ti buffer layer. *Appl. Catal. B Environ.,* **2018**, *237*, 158-165.

87. D. Bae, T. Pedersen, B. Seger, B. Iandolo, O. Hansen, P.C.K. Vesborg, I. Chorkendorff, Carrier-selective p- and n-contacts for efficient and stable photocatalytic water reduction. *Catal. Today,* **2017**, *290*, 59-64.

88. B. Seger, D.S. Tilley, T. Pedersen, P.C.K. Vesborg, O. Hansen, M. Grätzel, I. Chorkendorff, Silicon protected with atomic layer deposited TiO_2: durability studies of photocathodic H_2 evolution. *RSC Adv.,* **2013**, *3* (48), 25902-25907.

89. D.M. Andoshe, G. Jin, C.-S. Lee, C. Kim, K.C. Kwon, S. Choi, W. Sohn, C.W. Moon, S.H. Lee, J.M. Suh, S. Kang, J. Park, H. Heo, J.K. Kim, S. Han, M.-H. Jo, H.W. Jang, Directly Assembled 3D Molybdenum Disulfide on Silicon Wafer for Efficient Photoelectrochemical Water Reduction. *Adv. Sust. Syst. ,* **2018**, *2* (3), 1700142.

90. F. Li, Y. Yuan, X. Feng, J. Liu, S. Chen, Y. Lin, Y. Sun, H. Chen, L. Zhao, X. Song, P. Zhang, L. Gao, Coating of Phosphide Catalysts on p-Silicon by a Necking Strategy for Improved Photoelectrochemical Characteristics in Alkaline Media. *ACS Appl. Mater. Interfaces,* **2021**, *13* (17), 20185-20193.

91. J. Zheng, Y. Lyu, R. Wang, C. Xie, H. Zhou, S.P. Jiang, S. Wang, Crystalline TiO_2 protective layer with graded oxygen defects for efficient and stable silicon-based photocathode. *Nat. Commun.,* **2018**, *9* (1), 3572.

92. C. Das, M. Kot, K. Henkel, D. Schmeisser, Engineering of Sub-Nanometer SiOx Thickness in Si Photocathodes for Optimized Open Circuit Potential. *ChemSusChem,* **2016**, *9* (17), 2332-2336.

93. J.-Y. Jung, J.-Y. Yu, J.-H. Lee, Dynamic Photoelectrochemical Device Using an Electrolyte-Permeable $NiO_x/SiO_2/Si$ Photocathode with an Open-Circuit Potential of 0.75 V. *ACS Appl. Mater. Interfaces,* **2018**, *10* (9), 7955-7962.

94. R. Fan, W. Dong, L. Fang, F. Zheng, X. Su, S. Zou, J. Huang, X. Wang, M. Shen, Stable and efficient multi-crystalline n^+p silicon photocathode for H_2 production with pyramid-like surface nanostructure and thin Al_2O_3 protective layer. *Appl. Phys. Lett.,* **2015**, *106* (1), 013902.

95. L. Ji, M.D. McDaniel, S. Wang, A.B. Posadas, X. Li, H. Huang, J.C. Lee, A.A. Demkov, A.J. Bard, J.G. Ekerdt, E.T. Yu, A silicon-based photocathode for water reduction with an epitaxial $SrTiO_3$ protection layer and a nanostructured catalyst. *Nat. Nanotechnol.,* **2015**, *10* (1), 84-90.

96. S. Riyajuddin, J. Sultana, S.A. Siddiqui, S. Kumar, D. Badhwar, S.S. Yadav, S. Goyal, A. Venkatesan, S. Chakraverty, K. Ghosh, Silicon nanowire–Ta_2O_5–NGQD heterostructure: an efficient photocathode for photoelectrochemical hydrogen evolution. *Sustain. Energ. Fuels,* **2022**.

97. S. Zhang, H. Zhao, X. Li, Y. Li, Y. Jin, X. Liu, G. Shi, P.K. Wong, A hierarchical SiPN/CN/MoS_x photocathode with low internal resistance and strong light-absorption for solar hydrogen production. *Appl. Catal. B Environ.,* **2022**, *300*, 120758.

98. L. Han, I.A. Digdaya, T.W.F. Buijs, F.F. Abdi, Z. Huang, R. Liu, B. Dam, M. Zeman, W.A. Smith, A.H.M. Smets, Gradient dopant profiling and spectral utilization of monolithic thin-film silicon photoelectrochemical tandem devices for solar water splitting. *J. Mater. Chem. A,* **2015**, *3* (8), 4155-4162.

99. Z. Mei, Y. Chen, S. Tong, Y. Li, J. Liu, L. Sun, W. Zhong, X. Dong, Y. Ji, Y. Lin, H. Chen, F. Pan, High-Performance Si Photocathode Enabled by Spatial Decoupling Multifunctional Layers for Water Splitting. *Adv. Funct. Mater.,* **2021**, *n/a* (n/a), 2107164.

100. A.B. Laursen, T. Pedersen, P. Malacrida, B. Seger, O. Hansen, P.C.K. Vesborg, I. Chorkendorff, MoS_2—an integrated protective and active layer on n^+p-Si for solar H_2 evolution. *Phys. Chem. Chem. Phys.,* **2013**, *15* (46), 20000-20004.

101. S. Vanka, K. Sun, G. Zeng, T.A. Pham, F.M. Toma, T. Ogitsu, Z. Mi, Long-term stability studies of a semiconductor photoelectrode in three-electrode configuration. *J. Mater. Chem. A,* **2019**, *7* (48), 27612-27619.

Chapter 2 Construction of Buried a-Si/c-Si Junction Photocathodes for Boosting Photoelectrochemical Hydrogen Production

2.1 Introduction

Hydrogen fuel, as a clean and storable alternative, is critical to alleviating global environmental issues and maintaining sustainable energy systems, which can be derived from the water splitting via inexhaustible solar energy supply.[1] As one of the techniques for solar-driven water splitting, semiconductor-based photoelectrochemical (PEC) water splitting into hydrogen fuel has attracted increasing interest from researchers worldwide.[2-4] In particular, benefiting from a small bandgap of 1.1 eV for sufficient light absorption and suitable energy level of conduction band minimum above the hydron reduction potential, p-type crystal Si (c-Si) semiconductor has been extensively studied as a photocathode to facilitate efficient PEC hydrogen evolution reaction (HER).[4-9] With other significant advantages, such as non-toxicity, earth-abundant, and industrial-scale production, c-Si is expected to remain the dominant semiconductor for PEC HER application. However, the inert surface activity of the c-Si surface for HER presents sluggish hydrogen evolution kinetics, suggesting the necessary assistance of a cocatalyst .[10-12] In addition, the inherent oxidation and photo-corrosion of the c-Si in electrolytes are detrimental to realizing a durable PEC HER performance, which on most occasions needs a protective layer to isolate the c-Si with the electrolyte.[13-15] Both the two crucial challenges require using external materials, typically through the Si surface modification with a cocatalyst or a protective layer, while introducing the external materials brings the issues of electron transfer that are generally relative to the intrinsic band bending of the c-Si surface.[16, 17]

There is a representative case of c-Si decorated with Pt cocatalyst, in which the electron transfer is sluggish from c-Si to Pt even though Pt had been proven the most efficient electrocatalyst for HER.[18] Since Pt has a large work function located more negative than the Fermi level of the p-type c-Si, an upward electron transfer barrier is formed at the surface of Si when contacting Pt.[19] Fortunately, the problem can be solved using a mediate layer with a small work function or a high Fermi level, such as an n^+ emitter layer in a buried Si p-n junction further decorated with Pt[20-22], a metal layer like Au or Ag co-

deposited with Pt[23-25], or an insulator layer in a metal-insulator-semiconductor (MIS) structure[26, 27]. Considerable progress has been made in developing such heterostructures in order to enhance the electron transfer kinetics or obtain high photovoltage via a reasonable band barrier.[16, 28, 29] However, the complex heterostructure requires a strict fabrication process in most cases. For instance, building a buried Si p-n junction needs high temperatures and controllable time for doping phosphorous elements over the c-Si surface[30-32], and the MIS structure faces a major concern that insulators must have an approximate thickness to provide sufficient interfacial passivation but not hinder the electron transport[33].

Besides, introducing a mediator layer onto c-Si always brings concerns about defect states located at the interface of c-Si and the mediator layer, in which the defect states act as the recombination sites for the electron-hole carriers. In this respect, some studies have proposed that using an amorphous Si (a-Si) layer would reduce the detrimental effects.[34] For instance, Wang and coworkers fabricated an a-Si passivation layer for Si-based MIS junction via plasma-enhanced chemical vapor deposition (CVD) method to eliminate surface recombination defects of c-Si and interfacial defects at the c-Si/metal cocatalyst interface.[27] The a-Si also applied to directly decorated with Pt without any further mediator layer.[35-37] The above cases demonstrated that the a-Si layer not only acts as a passivation layer but also serves as a semiconducting component to modify band bending for rapid electron transfer kinetics. Although notably, a plasma-enhanced CVD method was commonly used to fabricate the above-exemplified photocathodes decorated with a-Si layers, which is time-consuming and high-cost.[38] Furthermore, the layer-by-layer fabrication method also brings the concerns of electron transfer at the multiple interfaces. Therefore, considering robust interface coupling between the multiple functional layers from the c-Si substrate to the cocatalyst is critical for photocathode preparation in practical applications.

In order to reduce the effect of interface defect states over the electron transfer to the greatest extent, in this work, an a-Si layer was directly co-deposited with Pt nanoparticles onto a planar p-type c-Si substrate through an electroless method to form a Pt/a-Si/c-Si photocathode. The resulting Pt/a-Si/c-Si photocathode presented an onset potential of +0.42 V_{RHE} and a photocurrent density of 35.0 mA cm^{-2} at 0 V_{RHE} in 0.5 M H_2SO_4 under simulated irradiation of 100 mW cm^{-2}. Furthermore, the optimum half-cell solar-to-hydrogen (STH) efficiency reached 3.98%. The enhanced hydrogen evolution property

was attributed to the buried a-Si layer between the c-Si substrate and the Pt nanoparticles, which acts as an electron transfer mediator and a passivation layer. The resulting a-Si/c-Si interface has a large energy band offset, providing a strong built-in electric field with a potential barrier to suppress carrier recombination and ensure charge transfer. The proposed strategy gives great potential to fabricate other photocathodes for PEC applications, such as CO_2 reduction, by tuning the component of metal cocatalyst and their size and morphology.

2.2 Experiment section

2.2.1 Materials preparation

Preparation of (hydrogen-terminated) H-terminated p-Si substrates: The pretreatment of boron-doped Si wafers (p-Si: 0.5 mm thickness, 1–10 ohm cm^{-1} resistivity) was adapted from previous literature.[39] The planar p-Si wafers were immersed in H_2O_2: H_2SO_4 (1:2) solution at 60 ºC for 30 min and washed by deionized water (DW), then etched in 0.5% HF at room temperature for 5 min and washed by DW, and then etched in HCl: H_2O_2: H_2O (1:1:4) solution at 60 ºC for 25 min and washed by DW. After that, the H-terminated p-Si substrates were obtained through immersed in a 40% NH_4F solution for 5 min and washed by DW.

Synthetic procedure of Pt particles: 60 mg $NaBH_4$ were dissolved in 10 mL DW to form fresh $NaBH_4$ aqueous solution. 25 mM H_2PtCl_6 solution were subsequently reduced with as-prepared $NaBH_4$ aqueous solution under vigorous stirring to obtain platinum particles. The resulting products were washed using ethanol and DW several times.

Fabrication of Pt/a-Si/c-Si and Pt/c-Si photocathodes: The H-terminated p-type c-Si substrates were prepared adapting procedures from previous literature.[39] As-prepared H-terminated p-Si wafer was immersed in 1.0 mM Na_2PtCl_6-containing 40% NH_4F aqueous solution for 1 h to prepare Pt/a-Si/c-Si junction photocathode. For comparison, two additional photocathodes were prepared. (1) The Pt/c-Si photocathode was obtained by the H-terminated p-type c-Si immersed in 2.0 mM H_2PtCl_6-containing 0.5% HF aqueous solution for 5 min. (2) The drop-casted Pt/c-Si (d-Pt/c-Si) photocathode was obtained through 2 steps: the synthesized Pt particles was first ultrasonically distributed in ethanol (1 mg mL^{-1}), the dispersion was then dropped onto the H-terminated p-type c-Si wafer (10 μg cm^{-2}) and dried at 60 ºC for over 2 hours under vacuum.

2.2.2 Material characterization

The crystal structures and surface valence states were measured by X-ray film diffraction and X-ray photoelectron spectroscopy (XPS, VG-ESCA Mark II) with monochromatized Al Kα radiation. The morphologies of the as-prepared samples were determined through scanning electron microscopy (SEM, JSM-6701F), focused ion beam-scanning electron microscope (FIB-SEM) system, and transmission electron microscope (TEM, JEM-2100F). A spectrophotometer (UV-2600, Shimadzu, Japan) was applied to obtain the ultraviolet-visible (UV-vis) absorption spectra of target samples. Photoluminescence (PL) emission (FP-6500) was utilized to investigate the charge carrier transfer and separation of the as-prepared samples.

2.2.3 Photoelectrochemical measurement

The PEC measurements, including linear sweep voltammograms (LSV), chronoamperometry curves, Mott–Schottky curves, and electrochemical impedance spectroscopy (EIS), were carried out on an electrochemical workstation (ALS/CH model 660D) using a three-electrode cell system at AM 1.5 G solar simulation (100 mW cm^{-2}). A graphite rod was used as the counter electrode and an Ag/AgCl (3M KCl) electrode was utilized as the reference electrode. The available area of the photocathode was 0.4 cm^2. The onset potential (V_{on}) is defined as the potential that produces a photocurrent density of −0.1 mA cm^{-2}. All the potentials could be transformed to the RHE using the equation: $E_{RHE} = E - IR + 0.059\times pH + E_{Ag/AgCl}$, where E is the experimental potential, $E_{Ag/AgCl}$ is equal to +0.197 V_{RHE} at ambient temperature of 25 °C, I and R are the photocurrent density (mA cm^{-2}) and the internal resistance (Ω) of electrolyte contact, respectively. Mott–Schottky curves were performed from –0.2 to +0.6 V_{RHE} at 2000 Hz. EIS tests were obtained at various conditions of 0.01–100 000 Hz. The hypothetical half-cell STH efficiency was was calculated using the equation half-cell $STH=|I|\times(E_{RHE}-E)/P_{Sun}\times 100\%$, where E is 0 V_{RHE} and P_{Sun} is 100 mW cm^{-2}.[40] Incident photon to electron conversion efficiency (IPCE) was measured using a motorized monochromator (M10; Jasco Corp.), which was calculated using the equation. $IPCE = I\times 1240/(\lambda \times P_{light})\times 100\%$, where I is the photocurrent density (mA cm^{-2}) obtained from the electrochemical workstation. λ and P_{light} refer to the incident light wavelength (nm) and the power density obtained at a specific wavelength (mW cm^{-2}), respectively.

2.3 Results and discussion

2.3.1 Synthesis and characterization of Pt/a-Si/c-Si photocathode

A common electroless method for Pt/c-Si photocathode preparation is hydrogen-terminated c-Si with the ability to reduce the precursor H_2PtCl_6 to Pt onto the Si surface in a strongly acidic HF aqueous solution.[41] The $PtCl_6^{2-}$ anion was reduced by Si^0 to form Pt nanoparticles, while Si^0 was oxidized to SiO_x, further etched by HF into SiF_6^{2-} anion. It was proposed that in the aqueous solutions with pH < 2, the HF species dominates, while HF_2^- and F^- ions then prevail at pH < 6 and pH > 6, respectively.[41] Increasing the pH would decrease the etching rate of Si, which can use NH_4F instead of HF. This work alternatively obtained controllable Pt nanoparticles through hydrogen-terminated p-type c-Si immersed in a $PtCl_6^{2-}$-containing NH_4F aqueous solution, and at the same time, an a-Si layer was formed between the c-Si and Pt nanoparticles. The self-assembly procedure of the Pt/a-Si/c-Si photocathode is shown in **Figure 2.1**.

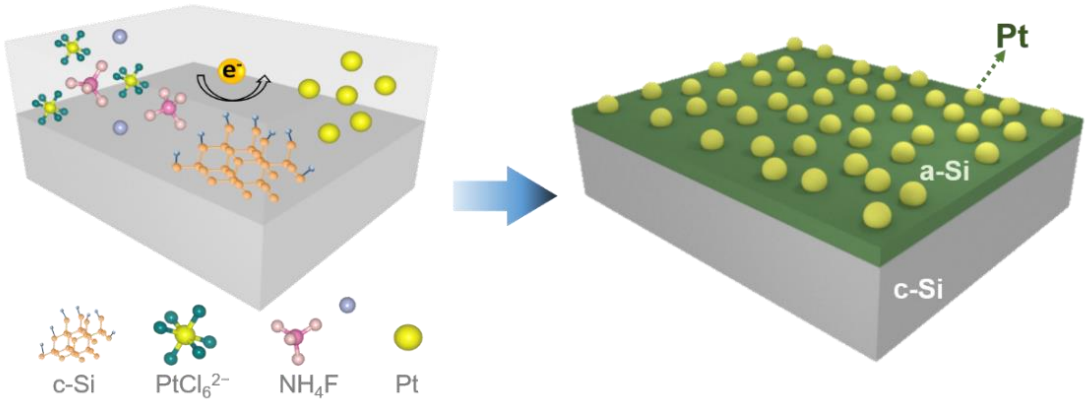

Figure 2.1 Schematic for preparing a Pt/a-Si/c-Si photocathode in an NH_4F aqueous solution with $PtCl_6^{2-}$ anion.

As shown in the top-view scanning electron microscopy (SEM) image of **Figure 2.2**a, the Pt particles with a diameter of about 50 nm were formed with uniform distribution on Pt/a-Si/c-Si photocathode using a mild NH_4F solution. In contrast, the Pt particles within the Pt/c-Si photocathode using an HF solution showed a bigger and uneven size (Figure 2.2b). To investigate the effect of two liquid-phase reaction environments, HF and NH_4F, on the size and distribution of the deposited Pt cocatalysts, a series of orthogonal comparative experiments with varying concentrations of the $PtCl_6^{2-}$ reactant and reaction time were performed. It was found that when the reaction solution was HF and the

reaction time was 5 min, an increase in the concentration of the $PtCl_6^{2-}$ reactant (from 0.2 to 1.0, 2.0, and 10 mM) would result in a significantly increased size of Pt particles (**Figure 2.3**). Especially at a large concentration of 10 mM, the diameter of most Pt particles grew to more than 100 nm, and agglomeration occurred. On the other hand, the Pt particles did not grow to excessive size or agglomerate under the same conditions when NH_4F was used as the reaction solution (**Figure 2.4**). Furthermore, the diameters of Pt particles grown in NH_4F solution were smaller and more uniform than those in HF solution at each concentration of $PtCl_6^{2-}$ reactant.

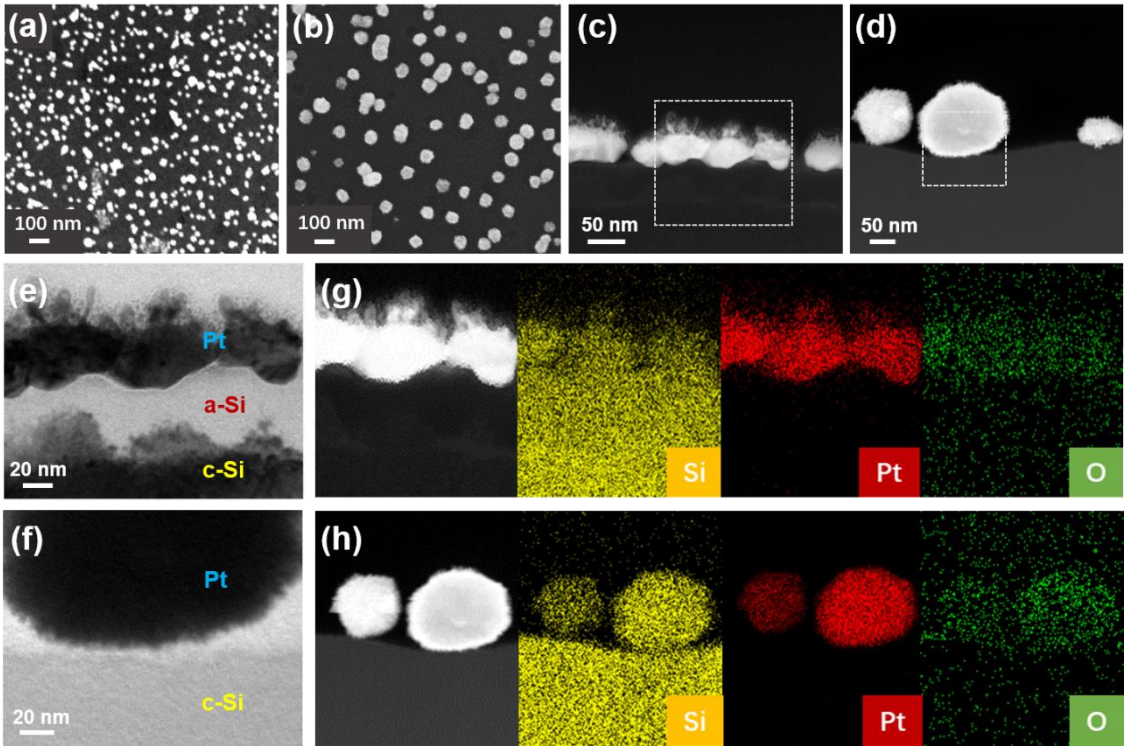

Figure 2.2 (a, b) SEM images, (c, d) HAADF-STEM images, (e, f) TEM images, and the corresponding (g, h) EDS mapping images of Pt/a-Si/Si and Pt/c-Si, respectively.

In addition, when the reaction time was increased from 5 min to 60 min and 120 min, the size and distribution of Pt particles grown with NH_4F almost remained unchanged, while the diameter of Pt particles grown under HF increased from about 80 nm to about 200 nm (**Figure 2.5**). And the number of loaded Pt particles was drastically reduced, most likely due to a large number of pits on the Si surface caused by the prolonged etching by the HF solution at low pH. Therefore, the milder NH_4F condition not only reduces the etching damage of the Si surface during the cocatalyst deposition process, but also avoids the inhomogeneity of the cocatalyst particles caused by the change of the reactant concentration during the redox deposition process.

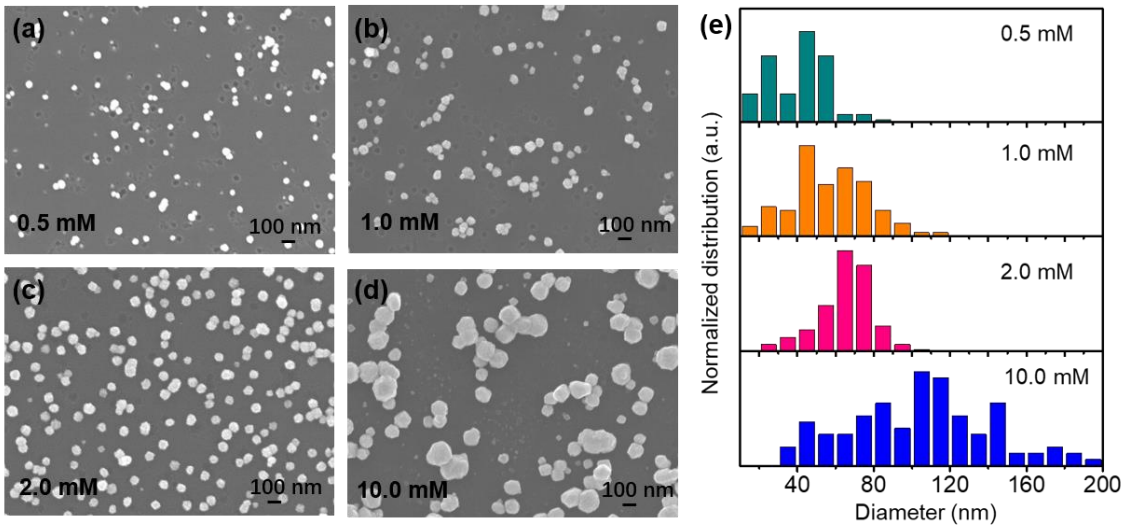

Figure 2.3 SEM images of various Pt/c-Si samples by electroless deposition method in HF solutions with (a) 0.5, (b) 1.0, (c) 2.0, and (d) 10.0 mM $PtCl_6^{2-}$ reactant for 5 min reaction duration. (e) Particle size distribution of corresponding Pt/c-Si samples.

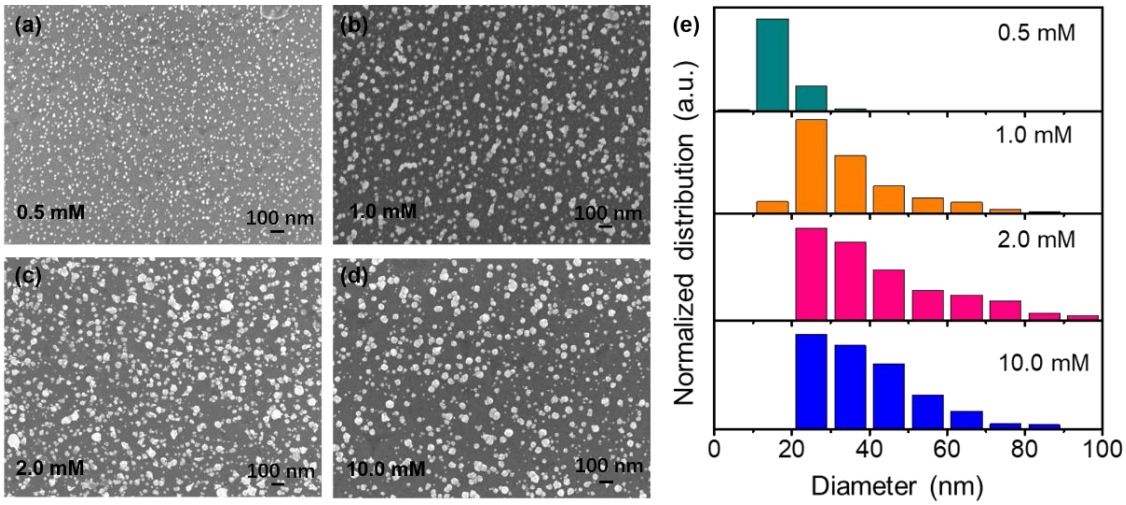

Figure 2.4 SEM images of various Pt/a-Si/c-Si samples by electroless deposition method in NH_4F solutions with (a) 0.5, (b) 1.0, (c) 2.0, and (d) 10.0 mM $PtCl_6^{2-}$ reactant for 5 min reaction duration. (e) Particle size distribution of corresponding Pt/a-Si/c-Si samples.

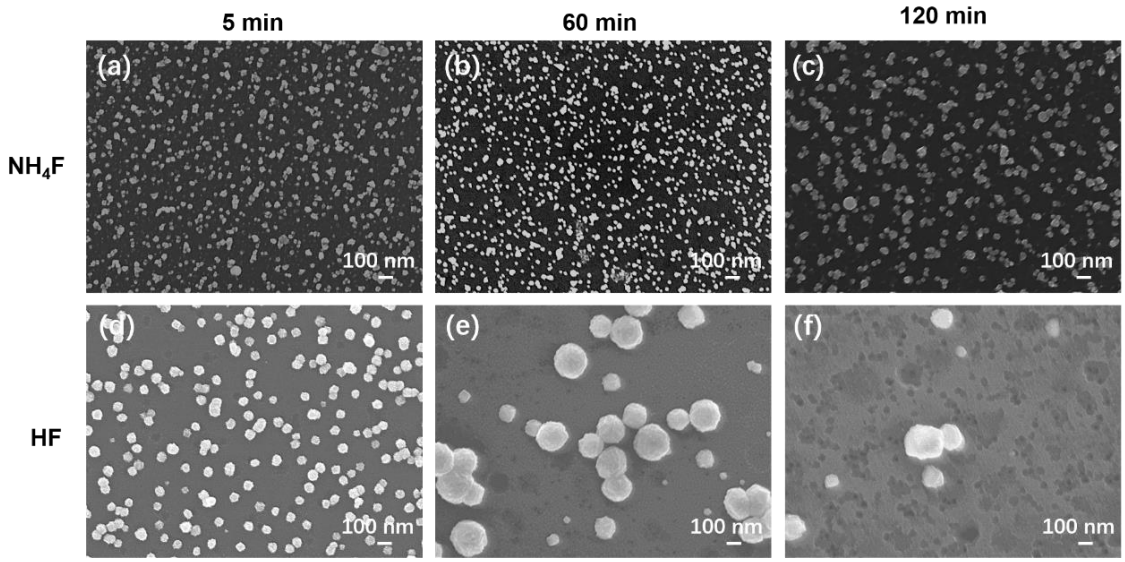

Figure 2.5 SEM images of (a-c) Pt/a-Si/c-Si in 1.0 mM $PtCl_6^{2-}$-NH_4F solution and (d-f) Pt/c-Si in 2.0 mM $PtCl_6^{2-}$-HF solution with increased reaction durations from 5 to 60 and 120 min.

The cross-section view of the high-angle annular dark-field scanning transmission electron microscopy (HAADF-STEM) and transmission electron microscopy (TEM) images are shown in Figure 2.2c and 2.2e, along with the corresponding magnified image and the energy-dispersive spectroscopy (EDS) mapping images in Figure 2.2g. As observed, a layered structure consisting of three layers was formed. First, the top layer mainly consists of Pt elements from the EDS mapping. Combining with the high-resolution TEM (HR-TEM) images in **Figure 2.6** that indicate the typical d-space of 0.226 nm of the (111) direction of Pt, which is obtained by measuring the average of 10 layers, the top layer is confirmed as Pt. Interestingly, some signals of the Si element in element mapping are found from the top layer. It is reported that there is a direct chemical reaction between Pt and Si to form platinum silicate during the electroless deposition.[42] However, from the X-ray diffraction (XRD) patterns in **Figure 2.7**, all of the diffraction peaks at 39.9°, 46.3°, 67.6°, 81.4°, and 85.9° correspond to the (111), (200), (220), (311) and (222) diffraction planes, which are indexed to the cubic phase of Pt (JCPDS No. 04-0802). Therefore, we proposed the first layer is mainly composed of Pt. Second, the middle layer is amorphous from Figure 2.6. The EDS mapping indicates only Si elements without O elements, suggesting the middle layer is most likely an amorphous Si (a-Si) layer. Third, the bottom layer is obviously the crystalline Si since there is only Si and the interplanar space of 0.312 nm corresponds to the (111) direction of c-Si (Figure 2.6c).

Therefore, the successful construction of the Pt/a-Si/c-Si multi-interfacial structure is confirmed, in which the thickness of the a-Si layer is approximately 25 nm when the reaction time is 60 min.

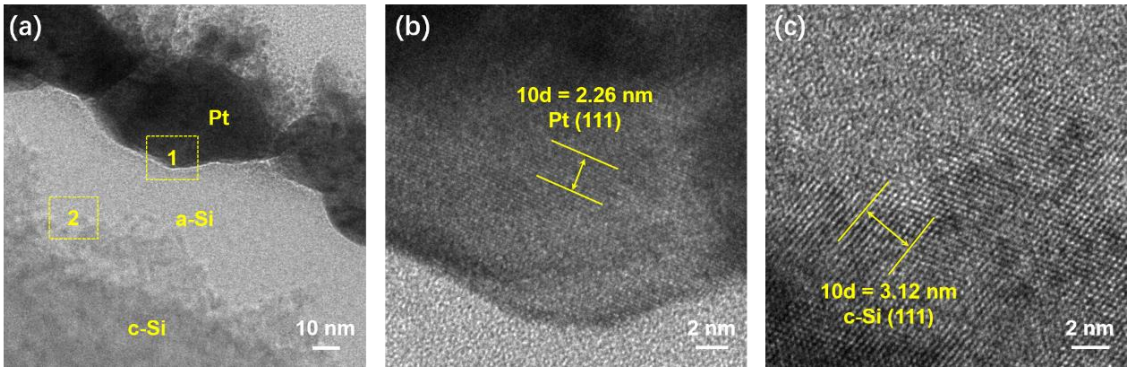

Figure 2.6 (a) HR-TEM images of Pt/a-Si/c-Si, and the related magnified images (b) and (c) corresponding to rectangular marked regions 1 and 2, respectively.

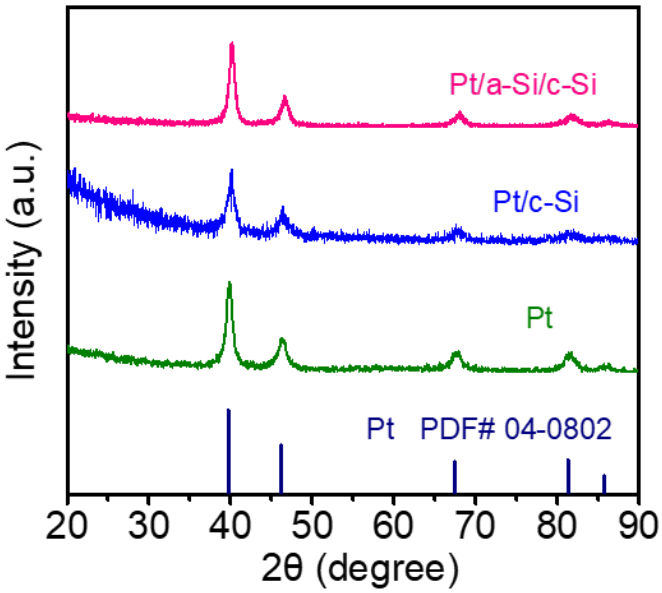

Figure 2.7 The thin-film XRD patterns of Pt/a-Si/Si, Pt/c-Si, and synthesized Pt.

In comparison, as observed from the cross-section HAADF-STEM and TEM images of Pt/c-Si in Figure 2.2d and 2.2f, the electroless deposition of Pt over Si in HF solution only results in a bilayer structure. The HR-TEM image in **Figure 2.8** indicates the typical interplanar space of 0.226 nm of the Pt (111) for the top layer and the interplanar space of 0.312 nm of the c-Si (111) for the bottom layer, corresponding to the XRD results in Figure 2.7. It is speculated that the different behavior of electroless Pt deposition over Si in HF and NH_4F is due to the distinct pH. As mentioned, the HF molecule dominates when pH is lower than 2, and the F^- ions prevail then when pH is higher than 6.[41] The F^-

ions have a much smaller radius of about 133 pm than 225 pm of HF molecule, which is prone to diffuse into the Si lattice and make Si amorphous. As a result, the thickness of the a-Si layer in the Pt/a-Si/c-Si structure varies with the increasing reaction time, from ~12 nm at 5 min to ~25 nm at 60 min and ~45 nm at 120 min, respectively, as shown in **Figure 2.9**.

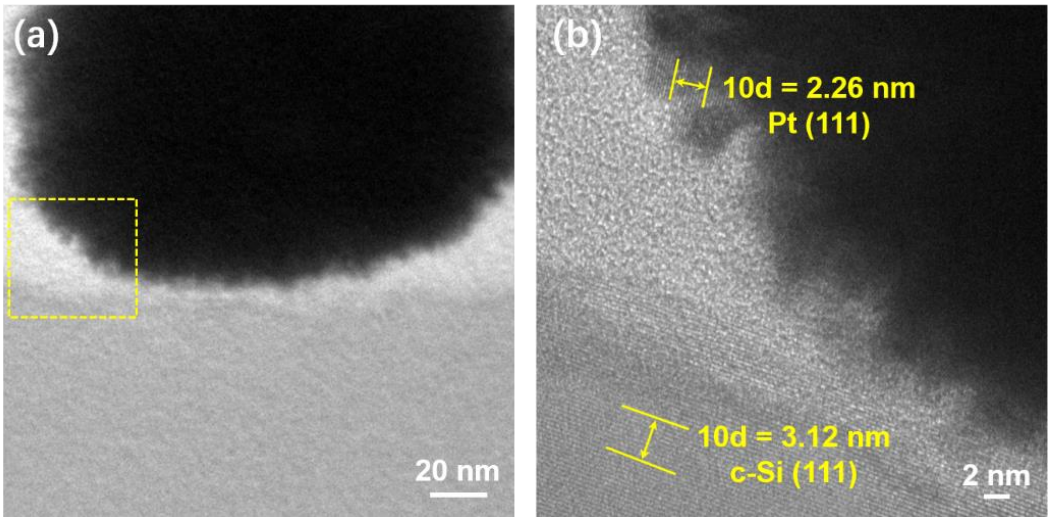

Figure 2.8 (a) HR-TEM image of Pt/c-Si, and the related magnified image (b) corresponding to rectangular marked region.

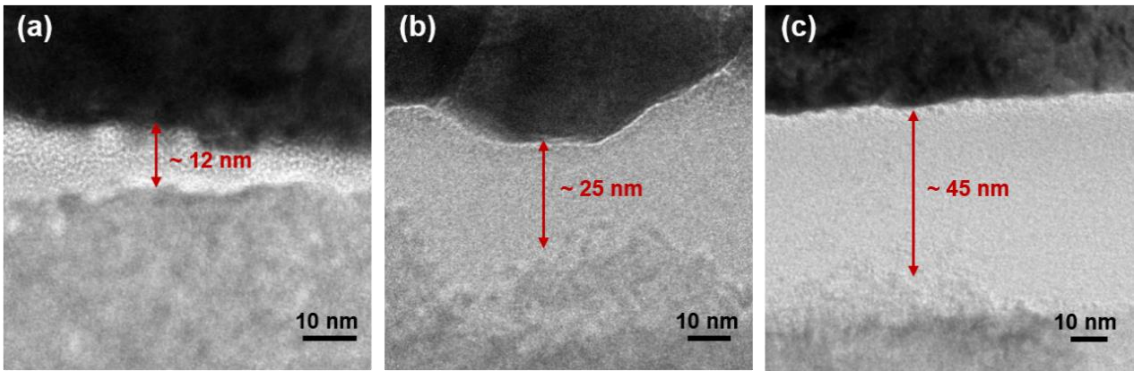

Figure 2.9 HR-TEM images of Pt/a-Si/c-Si in 1.0 mM $PtCl_6^{2-}$-NH_4F solution with increasing reaction time from (a) 5 min to (b) 60 min and (c) 120 min.

Apart from the distinct structures, Si signals in EDS mappings were found on the Pt particles of both Pt/a-Si/c-Si and Pt/c-Si samples (Figure 2g, h), where the Si content was estimated to be less than 5% of the atomic ratios in the EDS estimation (**Figure 2.10**). X-ray photoelectron spectroscopy (XPS) was employed to determine the chemical bonding states and surface elements. **Figure 2.11** shows the high-resolution XPS spectra of the Si 2p and Pt 4f regions for the as-prepared samples of Pt/a-Si/c-Si, Pt/c-Si, and synthesized

Pt particles. In Figure 2.11a for the high-resolution Si 2p spectra, two peaks at 99.6 eV and 103.3 eV correspond to Si^0 2p and Si^{4+} 2p are observed for both Pt/a-Si/c-Si and Pt/c-Si samples. The Si^{4+} 2p peak suggests the partial oxidation of Si substrate during the redox reaction of Pt deposition, which is similar to previously reported research. The Pt 4f XPS spectra (Figure 2.11b) also show two major peaks, 70.9 eV for Pt^0 $4f_{7/2}$ and 74.2 eV for Pt^0 $4f_{5/2}$. The combined results of XRD and XPS indicated that the nanoparticles are mainly composed of Pt.

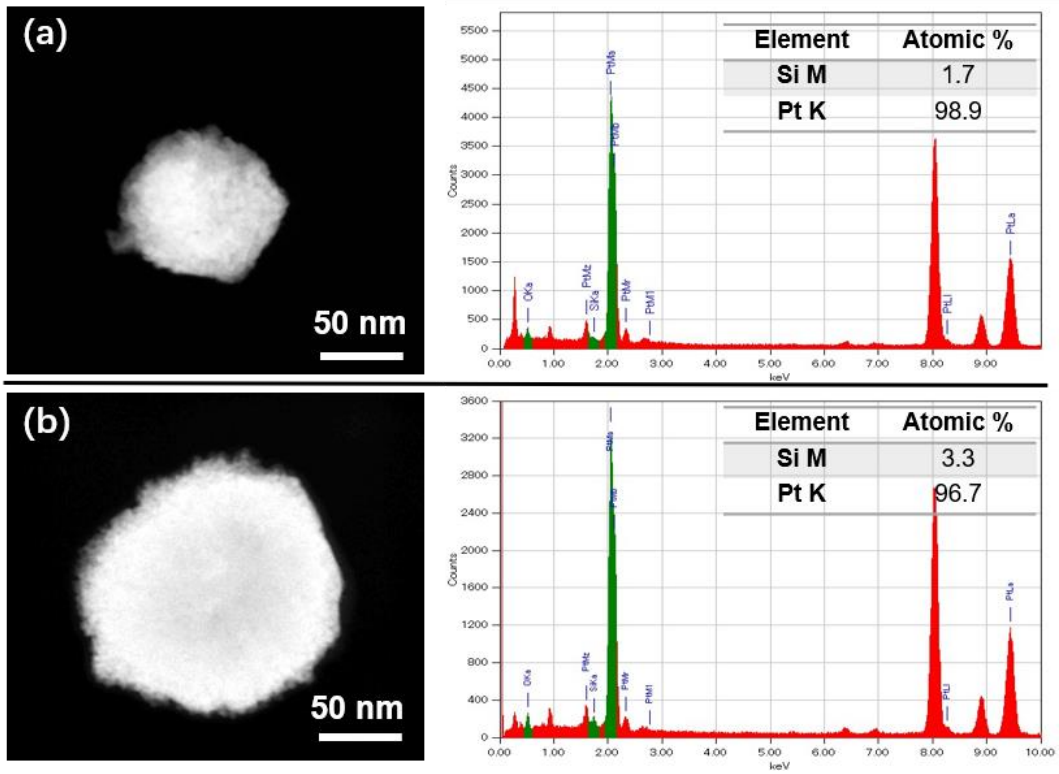

Figure 2.10 EDS images of (a) Pt/a-Si/c-Si and (b) Pt/c-Si

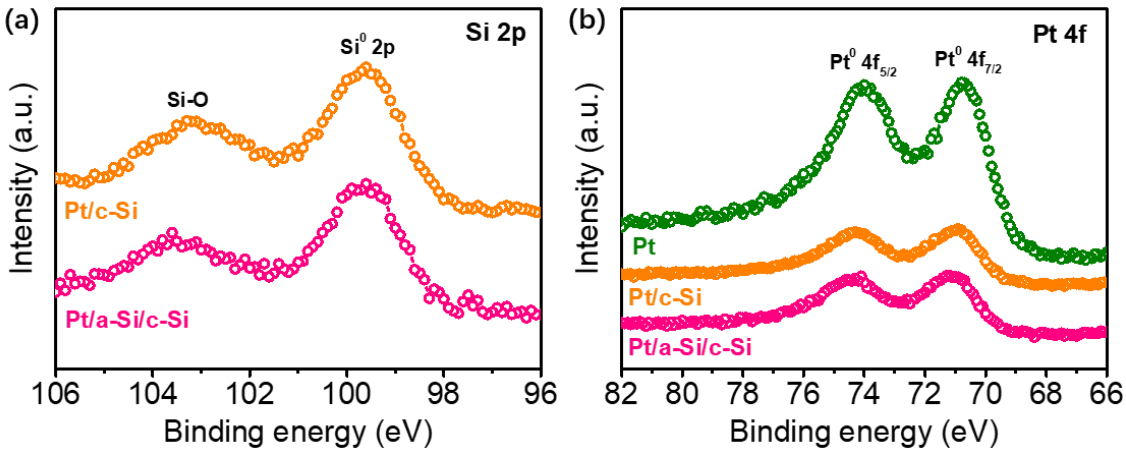

Figure 2.11 High-resolution XPS spectra of (a) Si 2p and (b) Pt 4f for Pt/a-Si/c-Si, Pt/c-Si, and synthesized Pt.

2.3.2 PEC-HER performances and mechanism analysis

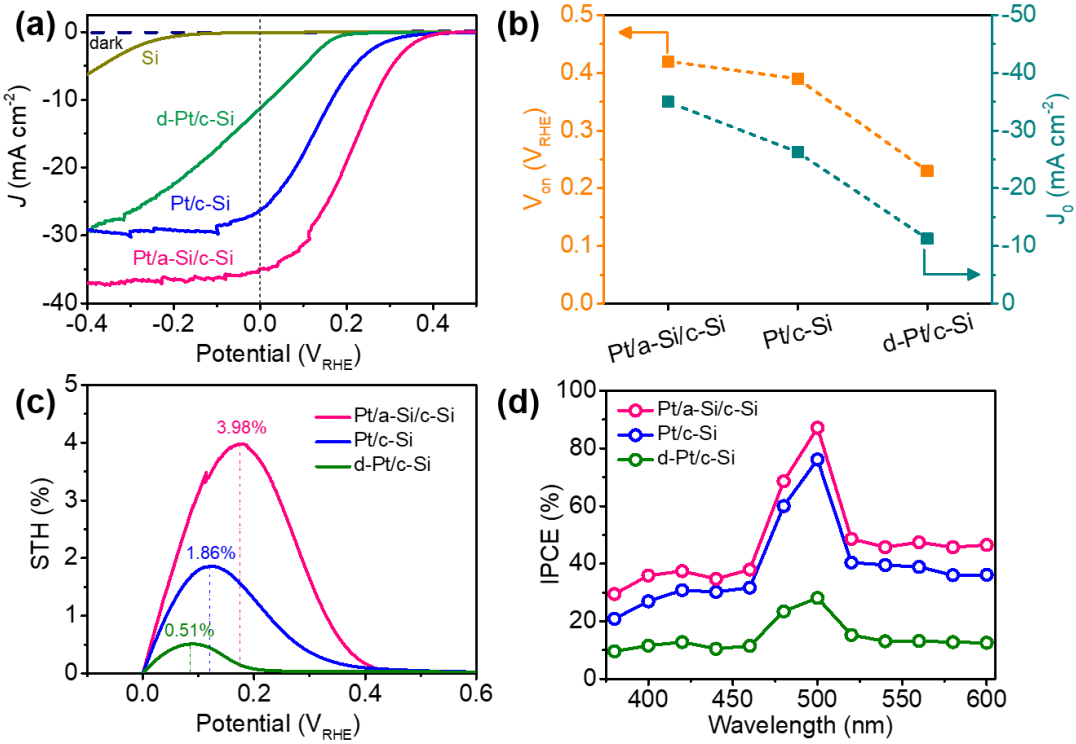

Figure 2.12 (a) LSV curves, (b) comparison of onset potentials (V_{on}) and photocurrent densities at 0 V_{RHE} (J_0), (c) half-cell STH efficiency, and (d) IPCE of Pt/a-Si/Si, Pt/c-Si, and d-Pt/c-Si photocathodes.

The PEC HER performances of the bare Si, the drop-casted Pt/c-Si (d-Pt/c-Si), the Pt/c-Si, and the Pt/a-Si/c-Si photocathodes, were evaluated using three-electrode electrochemical cell in a 0.5 M H_2SO_4 solution under front illumination by AM 1.5G (one-sun solar simulator). **Figure 2.12**a shows the best performance for Pt/a-Si/c-Si, achieving an onset potential of +0.42 V vs. reversible hydrogen electrode (V_{RHE}) and a photocurrent density of −35.0 mA cm^{-2} at 0 V_{RHE}. The obtained performance is significantly higher than +0.39 V_{RHE} and −26.3 mA cm^{-2} for Pt/c-Si, and +0.23 V_{RHE} and −11.3 mA cm^{-2} for d-Pt/c-Si under identical measurement conditions, as summarized in Figure 2.12b. It is worth noting that these performances were obtained on the photocathodes after optimizing the preparation parameters, including the concentration of $PtCl_6^{2-}$ reactant and the reaction time, as shown in **Figure 2.13−2.15.** Specifically, Pt/a-Si/c-Si refers to the optimized conditions of 1.0 mM $PtCl6^{2-}$-NH_4F solution and 60 min reaction time, and Pt/c-Si refers to the optimized conditions of 2.0 mM $PtCl6^{2-}$-HF solution and 5 min reaction time, while d-Pt/c-Si refers to the optimized Pt loading of 10 μg cm^{-2}.

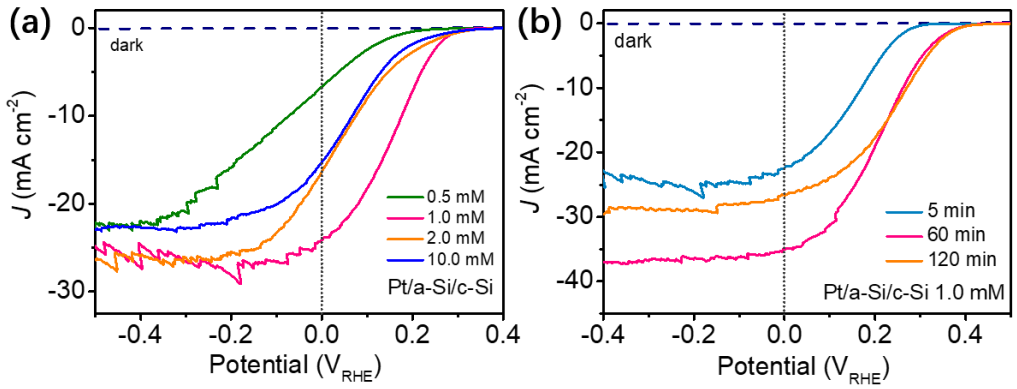

Figure 2.13 LSV curves of Pt/a-Si/c-Si obtained (a) in NH_4F solution with different concentration of $PtCl_6^{2-}$ reactants for 5 min, and (b) in 1.0 mM $PtCl_6^{2-}$-NH_4F solution with increasing reaction time.

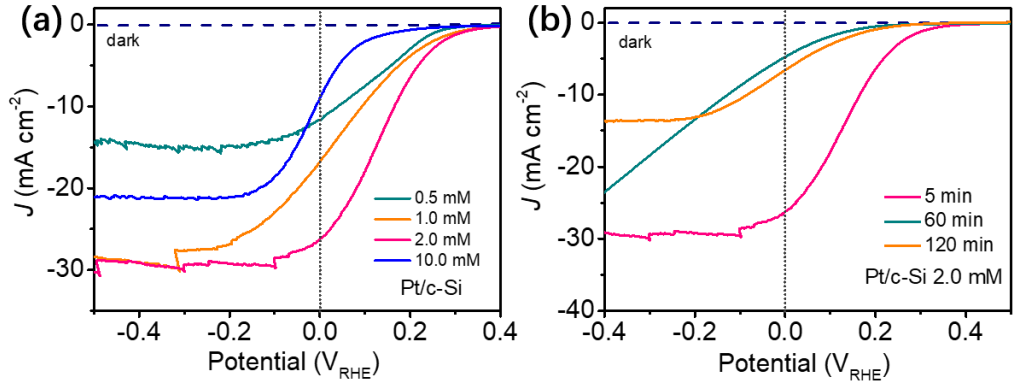

Figure 2.14. LSV curves of Pt/c-Si obtained (a) in HF solution with different concentration of $PtCl_6^{2-}$ reactants for 5 min, and (b) in 2.0 mM $PtCl_6^{2-}$-HF solution with increasing reaction time.

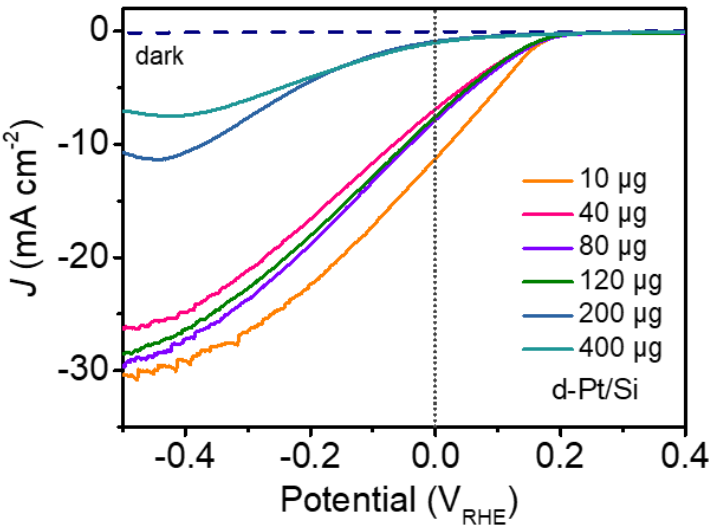

Figure 2.15 LSV curves of d-Pt/c-Si obtained with different Pt loadings.

Furthermore, the Pt/a-Si/c-Si photocathode had a higher saturated photocurrent density of −37.2 mA cm^{-2} than that of −30.0 mA cm^{-2} for Pt/c-Si, displaying its admirable light-harvesting capability. The UV-vis absorption spectra of the Pt/a-Si/c-Si and the Pt/c-Si photocathodes are shown in **Figure 2.16**. Two main pieces of information were obtained after analyzing the spectra. First, in addition to the typical light absorption by c-Si below 1100 nm, Pt/a-Si/c-Si extends the light absorption above 1100 nm due to the distinct optical advantage of a-Si[43], while Pt/c-Si has little light absorption in that region. Second, the light absorption capability below 1100 nm of Pt/a-Si/c-Si is higher than that of Pt/c-Si for the whole wavelength region, which may benefit from the integration of excellent rectification properties of the a-Si/c-Si buried junction with small-sized and uniformly distributed Pt nanoparticles. The two factors ultimately contribute to improving the saturated photocurrent density.

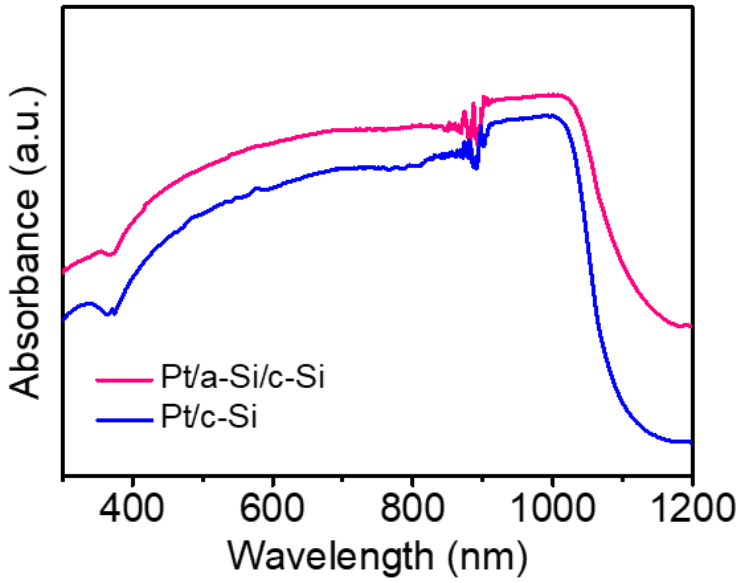

Figure 2.16. UV-vis spectra of Pt/a-Si/c-Si and Pt/c-Si.

As shown in Figure 2.12c, the optimum half-cell solar-to-hydrogen (STH) efficiency of 3.98% was obtained at 0.17 V_{RHE} by Pt/a-Si/c-Si, followed by Pt/c-Si with 1.86% at 0.12 V_{RHE}, and d-Pt/c-Si with 0.51% at 0.08 V_{RHE}. Besides, the increased values of STH efficiency by as-prepared photocathodes are consistent with their positive shifts in onset potentials, which implies the facilitated charge transfer in Pt/a-Si/c-Si photocathode. Furthermore, a noteworthy enhancement of incident photon-to-current efficiency (IPCE) was observed on the Pt/a-Si/c-Si over the wavelength range of 380−600 nm, with a maximum IPCE value of 87.2% at 500 nm (Figure 2.12d). Such high IPCE of Pt/a-Si/c-

Si can be explained by the good light utilization efficiency and rapid electron transfer, mainly owing to the passivation effect of the a-Si layer within the Si junction structure.

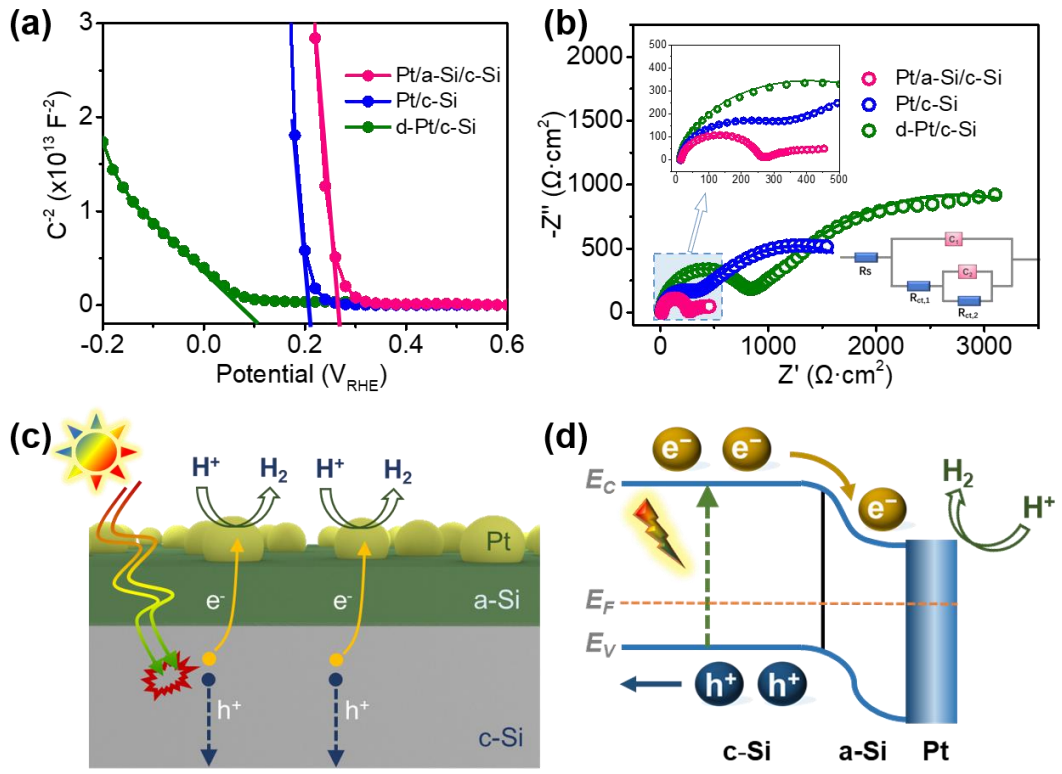

Figure 2.17 (a) Mott-Schottky plots under dark and (b) Nyquist plots and fitting figures (solid lines) of Pt/a-Si/Si, Pt/c-Si, and d-Pt/c-Si photocathodes. (c) Schematic and (d) the energy band diagrams of the Pt/a-Si/Si photocathode.

Mott-Schottky measurements were employed to examine why Pt/a-Si/c-Si can significantly improve the PEC-HER performance. As shown in **Figure 2.17**a, the flat-band potential (the intersection of tangent and x-axis) of Pt/a-Si/c-Si (0.28 V_{RHE}) is higher than those of the Pt/c-Si (0.21 V_{RHE}) and d-Pt/c-Si (0.11 V_{RHE}), which corresponds precisely to the positive shifting trend of their onset potentials as analyzed above. Electrochemical impedance spectroscopy (EIS) is a valid tool to determine the separation and transfer behavior of photogenerated carriers in Si-based photocathodes. Figure 2.17b shows the EIS measurements of Pt/a-Si/c-Si, Pt/c-Si, and d-Pt/c-Si photocathodes measured under illumination at +0.20 V_{RHE} to evaluate the charge-transfer resistances at different interfaces. All Nyquist plots have two arcs that can be fitted using an equivalent circuit, as shown in the inset of Figure 4b, where the fitting results are represented by solid lines. The equivalent circuit consists a series of resistances (Rs), two constant phase elements of the Si substrate (C_1) and cocatalyst (C_2), as well as two charge-transfer

resistances of R_{ct1} and R_{ct2}. The semicircle in the high-frequency area (R_{ct1}) represents the charge-transfer resistance from Si to the top cocatalyst, and the semicircle in the low-frequency region (R_{ct2}) reflects the resistance at the cocatalyst/electrolyte interface, corresponding to the surface catalytic kinetics.[6, 44] **Table 2.1** displays the fitted values of R_s, R_{ct1}, and R_{ct2}. Precisely, the R_s values of all the as-prepared photocathodes are small and comparable, indicating that the electrolyte resistivity is similar between these working and reference electrodes. The values of both R_{ct1} and R_{ct2} decrease in the order of d-Pt/c-Si, Pt/c-Si, and Pt/a-Si/c-Si. In particular, the R_{ct1} and R_{ct2} values of Pt/a-Si/c-Si are 238 and 302 Ω cm^2, respectively, which are much lower than that of other photocathodes (enlarged inset in Figure 2.17b). This result suggests that 1) compared with drop-coated method, the two photocathodes Pt/c-Si and Pt/a-Si/c-Si obtained by in-situ deposition possessed better coupling between Si and Pt to reduce the electron transfer resistance from the semiconductor to the cocatalyst, 2) the a-Si layer within a-Si/c-Si junction as a passivation layer could further efficiently accelerate the charge transfer at the Si/cocatalyst interface, 3) the even and small Pt nanoparticles grown on the a-Si layer promoted the electron transfer from the cocatalyst to the electrolyte, confirming the improved PEC-HER activities of Pt/a-Si/c-Si.

Table 2.1 The charge-transfer resistance values of Pt/a-Si/c-Si, Pt/c-Si, and d-Pt/c-Si photocathodes.

Photocathodes	**R_S (Ω·cm^2)**	**$R_{ct,1}$ (Ω·cm^2)**	**$R_{ct,2}$ (Ω·cm^2)**
Pt/a-Si/c-Si	14.1	238	302
Pt/c-Si	14.5	323	1889
d-Pt/c-Si	12.5	735	4029

Based on the above analysis, the better coupling of the a-Si/c-Si junction with Pt and its higher catalytic HER activity results in a superior PEC performance for the Pt/a-Si/c-Si. The schematic for the PEC-HER process of the Pt/a-Si/c-Si is shown in Figures 2.17c and 2.17d. First, the strong coupling of the a-Si/c-Si junction with Pt is due to the uniform assembly of the Pt nanoparticles onto a-Si/c-Si in a gentle condition, rather than the aggregated morphology of the as-prepared d-Pt/c-Si by the drop-casting method or the Pt/c-Si through a strongly acid environment. Second, the higher catalytic HER activity with high onset potential and photocurrent density of the photocathode possibly originates from the presence of an a-Si layer acting as a good passivation layer with moderately

conductive and providing pathways through which minority carriers can reach the Pt nanoparticles. Third, the resulting a-Si/c-Si junction has a large energy band shift of the valence band and the conduction band at interface to form a potential barrier, which can effectively suppress carrier recombination and ensure charge transfer.[36] Therefore, the above results indicate the feasibility of this buried a-Si/c-Si junction by utilizing the a-Si layer as carrier transfer mediator for an effective c-Si photocathode in the PEC-HER system.

2.4 Conclusions

In summary, this study has described a room-temperature and mild-condition strategy for modulating co-deposited Pt nanoparticle cocatalyst on the buried a-Si/c-Si junction photocathode for solar hydrogen evolution. Compared with the Pt/c-Si photocathode, the a-Si layer within Pt/a-Si/c-Si can not only act as an electron transfer mediator but also as a good passivation layer, producing a high-quality a-Si/c-Si buried junction for enhanced photovoltage and photocurrent response. Simultaneously, the large band shift at the a-Si/c-Si interface provides a bulti-in electric field with an additional force, which could suppress carrier recombination and ensures efficient charge transfer. In addition, the a-Si layer serves as the growth substrate of the cocatalyst, which could effectively modulate the size and distribution of Pt nanoparticles to be smaller and more uniform. This Pt/a-Si/c-Si photocathode presented an onset potential of +0.42 V_{RHE} and a photocurrent density of 35.0 mA cm^{-2} at 0 V_{RHE} in 0.5 M H_2SO_4. Based on this, we expect that the a-Si/c-Si junction structure will be widely applicable to improve the efficiency of Si-based photocathodes for PEC HER.

References

1. H. Song, S. Luo, H. Huang, B. Deng, J. Ye, Solar-Driven Hydrogen Production: Recent Advances, Challenges, and Future Perspectives. *ACS Energy Lett.,* **2022**, *7* (3), 1043-1065.
2. I. Roger, M.A. Shipman, M.D. Symes, Earth-abundant catalysts for electrochemical and photoelectrochemical water splitting. *Nat. Rev. Chem.,* **2017**, *1* (1), 0003.
3. E. Samuel, B. Joshi, M.-W. Kim, M.T. Swihart, S.S. Yoon, Morphology engineering of photoelectrodes for efficient photoelectrochemical water splitting. *Nano Energy,* **2020**, *72*, 104648.

4. R. Fan, Z. Mi, M. Shen, Silicon based photoelectrodes for photoelectrochemical water splitting. *Opt. Express,* **2019**, *27* (4), A51-A80.

5. K. Sivula, R. van de Krol, Semiconducting materials for photoelectrochemical energy conversion. *Nat. Rev. Mater. ,* **2016**, *1* (2), 15010.

6. Q. Ding, F. Meng, C.R. English, M. Cabán-Acevedo, M.J. Shearer, D. Liang, A.S. Daniel, R.J. Hamers, S. Jin, Efficient Photoelectrochemical Hydrogen Generation Using Heterostructures of Si and Chemically Exfoliated Metallic MoS_2. *J. Am. Chem. Soc.,* **2014**, *136* (24), 8504-8507.

7. Y. Hou, B.L. Abrams, P.C.K. Vesborg, M.E. Björketun, K. Herbst, L. Bech, A.M. Setti, C.D. Damsgaard, T. Pedersen, O. Hansen, J. Rossmeisl, S. Dahl, J.K. Nørskov, I. Chorkendorff, Bioinspired molecular co-catalysts bonded to a silicon photocathode for solar hydrogen evolution. *Nat. Mater.,* **2011**, *10* (6), 434-438.

8. H. Neergaard Waltenburg, J. Yates, Surface Chemistry of Silicon. *Chem. Rev.,* **1995**, *95* (5), 1589-1673.

9. S. Li, H. Lin, G. Yang, X. Ren, S. Luo, X.-s. Wang, Z. Chang, J. Ye, A synergetic strategy to construct anti-reflective and anti-corrosive Co-P/WS_x/Si photocathode for durable hydrogen evolution in alkaline condition. *Appl. Catal. B Environ.,* **2022**, *304*, 120954.

10. J. Joe, H. Yang, C. Bae, H. Shin, Metal Chalcogenides on Silicon Photocathodes for Efficient Water Splitting: A Mini Overview. *Catalysts,* **2019**, *9* (2).

11. K. Sun, S. Shen, Y. Liang, P.E. Burrows, S.S. Mao, D. Wang, Enabling Silicon for Solar-Fuel Production. *Chem. Rev.,* **2014**, *114* (17), 8662-8719.

12. S. Chen, L.-W. Wang, Thermodynamic Oxidation and Reduction Potentials of Photocatalytic Semiconductors in Aqueous Solution. *Chem. Mater.,* **2012**, *24* (18), 3659-3666.

13. D. Bae, B. Seger, P.C.K. Vesborg, O. Hansen, I. Chorkendorff, Strategies for stable water splitting via protected photoelectrodes. *Chem. Soc. Rev.,* **2017**, *46* (7), 1933-1954.

14. R. Fan, G. Huang, Y. Wang, Z. Mi, M. Shen, Efficient n^+p-Si photocathodes for solar H_2 production catalyzed by Co-W-S and stabilized by Ti buffer layer. *Appl. Catal. B Environ.,* **2018**, *237*, 158-165.

15. F. Li, Y. Yuan, X. Feng, J. Liu, S. Chen, Y. Lin, Y. Sun, H. Chen, L. Zhao, X. Song,

P. Zhang, L. Gao, Coating of Phosphide Catalysts on p-Silicon by a Necking Strategy for Improved Photoelectrochemical Characteristics in Alkaline Media. *ACS Appl. Mater. Interfaces,* **2021**, *13* (17), 20185-20193.

16. Z. Luo, T. Wang, J. Gong, Single-crystal silicon-based electrodes for unbiased solar water splitting: current status and prospects. *Chem. Soc. Rev.,* **2019**, *48* (7), 2158-2181.

17. I.-H. Yoo, Y.-J. Lee, S.S. Kalanur, H. Seo, Assembly of nonstoichiometric molybdenum oxide on Si as p-n junction photocathode for enhanced hydrogen evolution. *Appl. Catal. B Environ.,* **2020**, *264*, 118542.

18. C.U. Maier, M. Specht, G. Bilger, Hydrogen evolution on platinum-coated p-silicon photocathodes. *Int. J. Hydrogen Energy,* **1996**, *21* (10), 859-864.

19. S. Trasatti, Work function, electronegativity, and electrochemical behaviour of metals: III. Electrolytic hydrogen evolution in acid solutions. *J. Electroanal. Chem. Interf. Electrochem.,* **1972**, *39* (1), 163-184.

20. S.W. Boettcher, E.L. Warren, M.C. Putnam, E.A. Santori, D. Turner-Evans, M.D. Kelzenberg, M.G. Walter, J.R. McKone, B.S. Brunschwig, H.A. Atwater, N.S. Lewis, Photoelectrochemical Hydrogen Evolution Using Si Microwire Arrays. *J. Am. Chem. Soc.,* **2011**, *133* (5), 1216-1219.

21. R. Fan, W. Dong, L. Fang, F. Zheng, M. Shen, More than 10% efficiency and one-week stability of Si photocathodes for water splitting by manipulating the loading of the Pt catalyst and TiO_2 protective layer. *J. Mater. Chem. A,* **2017**, *5* (35), 18744-18751.

22. W. Cui, W. Niu, R. Wick-Joliat, T. Moehl, S.D. Tilley, Operando deconvolution of photovoltaic and electrocatalytic performance in ALD TiO2 protected water splitting photocathodes. *Chemical Science,* **2018**, *9* (28), 6062-6067.

23. J. Kye, M. Shin, B. Lim, J.-W. Jang, I. Oh, S. Hwang, Platinum Monolayer Electrocatalyst on Gold Nanostructures on Silicon for Photoelectrochemical Hydrogen Evolution. *ACS Nano,* **2013**, *7* (7), 6017-6023.

24. Z. Mei, Y. Chen, S. Tong, Y. Li, J. Liu, L. Sun, W. Zhong, X. Dong, Y. Ji, Y. Lin, H. Chen, F. Pan, High-Performance Si Photocathode Enabled by Spatial Decoupling Multifunctional Layers for Water Splitting. *Adv. Funct. Mater.,* **2022**, *32* (2), 2107164.

25. F. Urbain, V. Smirnov, J.-P. Becker, U. Rau, J. Ziegler, B. Kaiser, W. Jaegermann, F.

Finger, Application and modeling of an integrated amorphous silicon tandem based device for solar water splitting. *Sol. Energy Mater Sol. Cells,* **2015**, *140*, 275-280.

26. D.V. Esposito, I. Levin, T.P. Moffat, A.A. Talin, H_2 evolution at Si-based metal–insulator–semiconductor photoelectrodes enhanced by inversion channel charge collection and H spillover. *Nat. Mater.,* **2013**, *12* (6), 562-568.

27. B. Liu, S. Feng, L. Yang, C. Li, Z. Luo, T. Wang, J. Gong, Bifacial passivation of n-silicon metal–insulator–semiconductor photoelectrodes for efficient oxygen and hydrogen evolution reactions. *Energy Environ. Sci. ,* **2020**, *13* (1), 221-228.

28. S. Vanka, B. Zhou, R.A. Awni, Z. Song, F.A. Chowdhury, X. Liu, H. Hajibabaei, W. Shi, Y. Xiao, I.A. Navid, A. Pandey, R. Chen, G.A. Botton, T.W. Hamann, D. Wang, Y. Yan, Z. Mi, InGaN/Si Double-Junction Photocathode for Unassisted Solar Water Splitting. *ACS Energy Lett.,* **2020**, *5* (12), 3741-3751.

29. S. Choi, J. Hwang, T.H. Lee, H.-H. Kim, S.-P. Hong, C. Kim, M.-J. Choi, H.K. Park, S.S.M. Bhat, J.M. Suh, J. Lee, K.S. Choi, S.-H. Hong, J.C. Shin, H.W. Jang, Photoelectrochemical hydrogen production at neutral pH phosphate buffer solution using TiO_2 passivated InAs Nanowire/p-Si heterostructure photocathode. *Chem. Eng. J.,* **2020**, *392*, 123688.

30. Q. Jia, C. Yu, W. Liu, G. Zheng, C. Lei, L. Lei, X. Zhang, High performance n^+p-Si/Ti/NiS_xO_y photocathode for photoelectrochemical hydrogen evolution in alkaline solution. *J. Energy Chem. ,* **2019**, *30*, 101-107.

31. F. Zhang, X. Yu, J. Hu, L. Lei, Y. He, X. Zhang, Coupling Ru-MoS_2 heterostructure with silicon for efficient photoelectrocatalytic water splitting. *Chem. Eng. J.,* **2021**, *423*, 130231.

32. H. Li, B. Liu, S. Feng, H. Li, T. Wang, J. Gong, Construction of uniform buried pn junctions on pyramid Si photocathodes using a facile and safe spin-on method for photoelectrochemical water splitting. *J. Mater. Chem. A,* **2020**, *8* (1), 224-230.

33. T. Zhu, M.N. Chong, Prospects of metal–insulator–semiconductor (MIS) nanojunction structures for enhanced hydrogen evolution in photoelectrochemical cells: A review. *Nano Energy,* **2015**, *12*, 347-373.

34. D. Zhang, J. Shi, W. Zi, P. Wang, S. Liu, Recent Advances in Photoelectrochemical Applications of Silicon Materials for Solar-to-Chemicals Conversion. *ChemSusChem,* **2017**, *10* (22), 4324-4341.

35. K. Ueda, Y. Nakato, Y. Sakai, M. Matsumura, H. Tsubomura, n-type amorphous (or microcrystalline) silicon/p-type crystalline silicon heterojunction electrodes for efficient and stable solar-to-chemical conversion. *J. Appl. Phys.,* **1988**, *64* (3), 1513-1518.

36. H.-P. Wang, K. Sun, S.Y. Noh, A. Kargar, M.-L. Tsai, M.-Y. Huang, D. Wang, J.-H. He, High-Performance a-Si/c-Si Heterojunction Photoelectrodes for Photoelectrochemical Oxygen and Hydrogen Evolution. *Nano Lett.,* **2015**, *15* (5), 2817-2824.

37. K. Ueda, Y. Nakato, H. Sakamoto, Y. Sakai, M. Matsumura, H. Tsubomura, Efficient Solar to Chemical Conversion with an n-Type Amorphous Silicon/p-Type Crystalline Silicon Heterojunction Electrode. *Chemistry Letters,* **1987**, *16* (4), 747-750.

38. A.T. Sivagurunathan, S. Adhikari, D.-H. Kim, Strategies and implications of atomic layer deposition in photoelectrochemical water splitting: Recent advances and prospects. *Nano Energy,* **2021**, *83*, 105802.

39. H. Lin, S. Li, G. Yang, K. Zhang, D. Tang, Y. Su, Y. Li, S. Luo, K. Chang, J. Ye, In Situ Assembly of MoS_x Thin-Film through Self-Reduction on p-Si for Drastic Enhancement of Photoelectrochemical Hydrogen Evolution. *Adv. Funct. Mater.,* **2021**, *31* (3), 2007071.

40. Y.F. Tay, H. Kaneko, S.Y. Chiam, S. Lie, Q. Zheng, B. Wu, S.S. Hadke, Z. Su, P.S. Bassi, D. Bishop, T.C. Sum, T. Minegishi, J. Barber, K. Domen, L.H. Wong, Solution-Processed Cd-Substituted CZTS Photocathode for Efficient Solar Hydrogen Evolution from Neutral Water. *Joule,* **2018**, *2* (3), 537-548.

41. G.V. Kuznetsov, V.A. Skryshevsky, T.A. Vdovenkova, A.I. Tsyganova, P. Gorostiza, F. Sanz, Platinum Electroless Deposition on Silicon from Hydrogen Fluoride Solutions: Electrical Properties. *J. Electrochem. Soc.,* **2001**, *148* (8), C528.

42. P. Gorostiza, J. Servat, J.R. Morante, F. Sanz, First stages of platinum electroless deposition on silicon (100) from hydrogen fluoride solutions studied by AFM. *Thin Solid Films,* **1996**, *275* (1), 12-17.

43. A. Feltrin, R. Bartlome, C. Battaglia, M. Boccard, G. Bugnon, P. Buehlmann, O. Cubero, M. Despeisse, D. Domine, F.J. Haug, F. Meillaud, X. Niquille, G. Parascandolo, T. Soederstroem, B. Strahm, V. Terrazzoni, N. Wyrsch, C. Ballif, An Introduction To The Technology Of Thin Film Silicon Photovoltaics. *Informacije*

MIDEM-Journal of Microelectronics Electronic Components And Materials, **2009**, *39*, 231-236-231-236.

44. G. Yang, S. Li, X. Wang, B. Ding, Y. Li, H. Lin, D. Tang, X. Ren, Q. Wang, S. Luo, J. Ye, A universal strategy boosting photoelectrochemical water oxidation by utilizing MXene nanosheets as hole transfer mediators. *Appl. Catal. B Environ.,* **2021**, *297*, 120268.

Chapter 3 Engineering Heterogeneous NiS_2/NiS cocatalysts with Progressive Electron Transfer from Planar p-Si Photocathodes for Solar Hydrogen Evolution

3.1 Introduction

As a promising approach to renewable energy conversion, solar-driven photoelectrochemical (PEC) water splitting into hydrogen fuel has triggered many exploring studies.[1-3] Among the numerous attractive photoelectrodes, the silicon semiconductor has been widely studied and proven to facilitate efficient PEC hydrogen evolution reaction (HER) because of its suitable band gap (1.1 eV) that absorbs sufficient visible light.[3-6] Generally, Si requires an external cocatalyst for HER because it possesses sluggish surface kinetics. Extensive studies have demonstrated that an interphase structure between Si and the cocatalyst is vital for PEC performance since it affects the transfer kinetics of the photogenerated electron from Si to the cocatalyst.[6-10] Therefore, to achieve efficient electron transfer, several complex processes have been employed to modify the interphase structures by forming the various junctions (pn^+, n^+p, n^+np^+, etc.), buffer layers, or surface textures (nanowires, microwires, micropillars, etc.),[11-17] which essentially modify the band bending at the interphase. Particularly driven by the large built-in potentials of the junction structures, the structuring of the Si substrates with buried p-n junctions has been widely adopted to induce increased band bending at the n/p interface and enhanced photovoltage, which further facilitates the fast transfer of electrons from the Si semiconductor to the cocatalyst, thereby improving HER performance.[13, 18] However, such modifications mainly focus on the Si substrate and ignore the cocatalyst, which is generally an alternative method for effective band bending and electron transfer. As the modification of the cocatalyst involves employing atomic layer deposition or photo-assisted electrodeposition to fabricate a thin metal layer or a heterogeneous cocatalyst structure, respectively.[19, 20] Numerous heterogeneous cocatalyst structures have demonstrated promising prospects with excellent HER performance.[17, 20-23] Among the effective cocatalysts, transition metal sulfides are promising for achieving such heterogeneous structures because they comprise various forms of compounds that possess adjustable chemical and physical properties.[9, 21, 24, 25]

Nickel sulfides (NiS_x), a family of transition metal sulfides, have recently attracted

tremendous attention as promising candidates to replace Pt in electrochemical (EC) HER because of their superior catalytic properties.[15, 20, 26-31] Further, NiS_2 and NiS (the two typical crystalline phases of NiS_x) have been studied for their good HER catalytic activity.[28-31] Particularly, NiS_2 exhibits enhanced HER catalytic performance.[27, 32] Furthermore, the in-situ NiS_2/NiS heterostructure possesses integrated properties because of its mono-component counterparts and exhibits synergistically enhanced kinetics that was attributed to the concurrent promotion of the charge transfer and varied the active sites, thus demonstrating superior HER activities compared with the individual components or physical mixtures.[28, 31] However, there are very few relative works on the application of such excellent NiS_x as cocatalysts in Si-based photocathodes for the fields of PEC-HER probably because of the sluggish kinetics of the electron transfer from Si to NiS_x. Very recently, the application of NiS or $NiS_{1.97}$ as a cocatalyst on Si nanowire array photocathodes was reported to achieve an optimized photocurrent of 10 mA cm^{-2} at 0 V_{RHE} and an onset potential of 0.2 V_{RHE} in a pH = 0 medium, while this PEC-HER performance was still limited in such a complex fabrication of nanowire arrays.[33] Thus, it is expected that the fabrication of heterogenic NiS_2 and NiS nanostructures on a planar Si photocathode will be an operative pathway toward achieving effective electron transfer. Owing to the difference in their band structures, it is more feasible to modify the band bending when the planar Si photocathode is decorated with a heterogenic NiS_x nanostructure that combines the NiS_2 and NiS phases. Besides, the similar elements in NiS_2 and NiS promote the feasibility of the in-situ fabrication of such a heterojunction.

Here, a novel NiS_2/NiS heterojunction (NNH) with an n-type semiconducting property was designed and successfully fabricated in-situ. Thereafter, NNH was applied as a cocatalyst on the planar p-Si photocathode for PEC-HER. The resulting NNH/Si photocathode exhibited an onset potential of 0.28 V_{RHE} and a photocurrent density of −18.9 mA cm^{-2} at 0 V_{RHE} under simulated irradiation of 100 mW cm^{-2} with an AM 1.5 G filter. Furthermore, the optimum half-cell solar-to-hydrogen (HC-STH) efficiency reached 0.9%. The enhanced hydrogen evolution was attributed to the promotion of the electron transfer through a progressive transfer system that was favored by the heterogenic nanostructure of NNH in which some of the photogenerated electrons were transferred from planar p-Si to Ni^{2+} in the NiS phase and Ni^{2+} and/or S_2^{2-} in the defect-rich NiS_2 phase. Contrary to the re-doping of the p-Si surface to form the pn^+ junctions to modify the surface band bending[11, 12, 14], the synergetic integration of NNH with planar p-

Si afforded bifunctional roles in inducing a local electric field that acted as a progressive electron transfer medium, as well as affording the active sites. It is expected that this progressive manner would elucidate other non-noble metal sulfide cocatalysts with PEC-HER applications from the viewpoint of progressive electron transfer through engineering the heterogeneous architectures.

3.2 Experimental Section

3.2.1 Materials preparation

The synthetic procedure of Ni-Precursors: 0.45 g $NiCl_2 \cdot 6H_2O$ and 1.8 g Urea were firstly dissolved in 90 mL ultrapure deionized water (DW) with 0.5 h stirring, the aqueous solution was moved in a 150 mL Teflon-lined autoclave, which put into a heating oven at 180 ºC for10 h. The green product (named Ni-Pre-2) was thoroughly cleaned with DW and ethanol (3 times respectively) followed by drying at 70 ºC for 12 h. For comparison, the Ni-Pre-1 was prepared with 1.8 g $NiCl_2 \cdot 6H_2O$ and 0.45 g Urea through the same procedure of the Ni-Pre-2 sample just the heating process at 150 ºC.

The synthetic procedure of NNH, NiS_2, and NiS: 40 mg Ni-Pre-2 and 0.12 g thioacetamide (TAA) were uniformly distributed in 40 mL ethanol after 1 h sonication, then transferred to 50 mL Teflon-lined autoclave at 120 ºC for 6 h. The final products were washed using ethanol several times and then dried overnight at 70 ºC (named NNH). At the same procedure of NNH, the product of Ni-Pre-1 with TAA was named NiS_2. And the obtained NiS_2 sample was calcined in a tubular furnace in Ar atmosphere, at 650 ºC for 2 h with 5 ºC min^{-1} (named NiS).

Fabrication of NNH, NiS_2, and NiS cathodes: The as-synthesized NNH catalyst (10 mg) was first ultrasonically distributed in DW (1 mL). Then, the liquid was moved onto the glassy carbon electrode (200 μL cm^{-2}) by a measured drop-casting method, and the solvent was evaporated at 60 °C for 5 h. The NNH cathode was fabricated as the working electrode, and the NiS_2 and NiS cathodes were prepared through the same procedure.

Fabrication of planar p-Si photocathodes: The pretreatment of Silicon (Si) wafers was adapted from previous literature.[7] Briefly, the p-type (111) Si wafers (area: 1 cm × 1 cm; thickness: 0.5 mm; resistivity: 1–10 ohm cm^{-1}; boron-doped) were immersed in a piranha solution of H_2O_2/H_2SO_4 (1:2, v/v) at 60 ºC for 30 min and rinsed with DW, then etched in 0.5% HF at ambient temperature for 5 min and rinsed with to remove the oxide layer and organic contamination. After that, the planar p-Si substrate was etched in the solution

containing HCl: H_2O_2: H_2O (1:1:4, v/v/v) at 60 °C for about 25 min and rinsed with DW. Subsequently, the planar p-Si substrate was immersed in a 40% NH_4F solution for 5 min and washed by DW. After that, the backside of the planar p-Si substrate was coated with the eutectic gallium–indium alloy to achieve Ohmic contact, then the planar p-Si substrate above attached to a Cu plate and sealed with resin. The planar p-Si photocathode was obtained to serve as a working electrode.

Fabrication of NNH/Si, NiS_2/Si, and NiS/Si photocathodes: The as-synthesized NNH cocatalyst (1 mg) was first ultrasonically distributed in ethanol (1 mL). Then, the dispersion was dropped onto the planar p-Si photocathode (10 μg cm^{-2}) and dried at 60 °C for over 2 hours under vacuum. The NNH/Si photocathode was obtained, and the NiS_2/Si and NiS/Si photocathodes were prepared through the same procedure of the NNH/Si photocathode.

3.2.2 Materials Characterization

The crystal structures were investigated by an X-ray powder diffraction (XRD, D/MAX-2500, Rigaku, Japan) and Raman spectra (Raman Touch-VIS-NIR). Surface valence states were observed by an X-ray photoelectron spectroscopy (XPS, VG-ESCA Mark II) with monochromated Al Kα radiation and the reference of C 1s peak at 284.8 eV. The specific surface areas of the precursor samples were obtained via nitrogen adsorption-desorption measurements (BELSORP-mini II). The morphologies of as-obtained samples were observed by utilizing scanning electron microscopy (FESEM, JSM-6701F), and (high-resolution) transmission electron microscope (HR-TEM, JEM-2100F), the energy dispersive spectrometer (EDS), as well as selected area electron diffraction (SAED). Ultraviolet–visible (UV–vis) absorption spectra were determined using a spectrophotometer (UV-2600, Shimadzu, Japan). Thermogravimetric analysis (TGA, TA-60WS PCSET) was investigated from ambient temperature to 900 °C with 10 °C min^{-1} in air, defining the ratio of NiS_2 to NiS within the NNH sample. Briefly, approximately 31% weight loss is related to the oxidation and burning-out of the NNH, and the final oxidation product at 950 °C in the air atmosphere is NiO, corresponding with the XRD pattern in the inset of Figure 3.2c. According to the principle of mass conservation, the detailed calculation of the mole ratio of NiS_2 to NiS within the NNH are shown as following:

$$\text{Ni wt\%} = (1\text{-}z\ \text{wt\%})/M_{(NiO)} \times M_{(Ni)}$$

$$n_{(S)} = (1\text{- Ni wt\%})/M_{(S)}$$

$$x + y = \text{Ni wt\%}/\ M_{(Ni)}$$

$$2x + y = n_{(S)}$$

Where z wt% is the weight loss of NNH; $M_{(NiO)}$, $M_{(Ni)}$, and $M_{(S)}$ are the mass fraction of NiO, Ni, and S elements, respectively; $n_{(S)}$, x, and y are the amounts of substance of S element, NiS_2, and NiS in the NNH, respectively. Hence, the molar ratio of NiS_2 to NiS within the NNH sample is x: y, that is 1:1.

3.2.3 Electrochemical and photoelectrochemical measurements

The EC and PEC measurements were carried out using a three-electrode cell system under an inert atmosphere (argon) and AM 1.5 G solar simulation (100 mW cm^{-2}), which contained a graphite rod as the counter electrode and an Ag/AgCl (3M KCl) electrode as the reference electrode. The exposure area of the working electrode immersed in the electrolyte is 1.0 cm^2. Linear sweep voltammograms (LSV) were obtained on an electrochemical workstation (ALS/CH model 660D). Mott–Schottky curves were performed from –0.2 to 0.4 V_{RHE} at 1000 Hz. Electrochemical impedance spectroscopy (EIS) tests were obtained at various conditions (0.01–100 000 Hz). All the potentials could be transformed to the RHE using the equation: $E_{RHE} = E_{Ag/AgCl} – IR + 0.059 \times pH + E^0_{Ag/AgCl}$, where $E_{Ag/AgCl}$ is the experimental potential; I and R are the photocurrent density (mA cm^{-2}) and the internal resistance (Ω) of electrolyte contact, respectively. The hypothetical HC-STH was calculated using the equation $\text{HC-STH} = |I| \times (E_{RHE}\text{-}E)/P_{Sun} \times 100\%$, where E is 0 V_{RHE} and P_{Sun} is 100 mW cm^{-2}.[34] Different kinds of electrolytes were used: (1) For the pH 0 solution, 6.8 mL 18.4 M H_2SO_4 were added to 250 mL water, which is 0.5M H_2SO_4 aqueous solution; (2) For the pH 6.2 solution, 7.1 g Na_2SO_4 was dissolved in 100 mL water, which is 1 M Na_2SO_4 (pH 6.2); (3) For the pH 2.2 solution, 0.5 M H_2SO_4 was dropped into 1 M Na_2SO_4 aqueous solution to reach the desired pH; (4) For the pH 4.2 solution, 50 mM H_2SO_4 was dropped into 1 M Na_2SO_4 aqueous solution to reach the desired pH. The pHs of differrent solutions were measured with a benchtop Mettler Toledo pH meter.

3.2.4 Computational details

The first principle calculation was performed using PWSCF code from the Quantum

ESPRESSO package.[35, 36] The exchange and correlation potential were used in the generalized gradient approximation (GGA) in the scheme of Perdew, Burke and Ernzerrof (PBE).[37] All the geometry structures were relaxed until energy is converged to 1×10^{-6} Ry. A cutoff energy of 60 Ry was set for the real-space integration grid. Brillouin zone was sampled by 3×3×3 k-points grid for optimization and 5×5×5 for electronic structures. The DFT-D2 method was employed for van der Waals correction.[38, 39]

3.3 Results and discussion

3.3.1 Characterization of the in-situ heterogenic NNH cocatalysts

NNH was designed, as shown in **Figure 3.1**. First, by tuning the ratio of Ni^{2+} to urea in the precursor reactants, the self-assembled spherical-like Ni precursor-1 (Ni-Pre-1) and flake-like Ni precursor-2 (Ni-Pre-2) were obtained by the hydrothermal method. The X-ray powder diffraction (XRD) pattern disclosed the phases of both Ni precursors (**Figure 3.2**a). Next, Ni-Pre-1 and Ni-Pre-2 were transformed into pure NiS_2 and NNH via the sulfonation reaction under the same conditions. Additionally, NiS was obtained through the calcination of NiS_2 at a high temperature, as described in the experimental section.

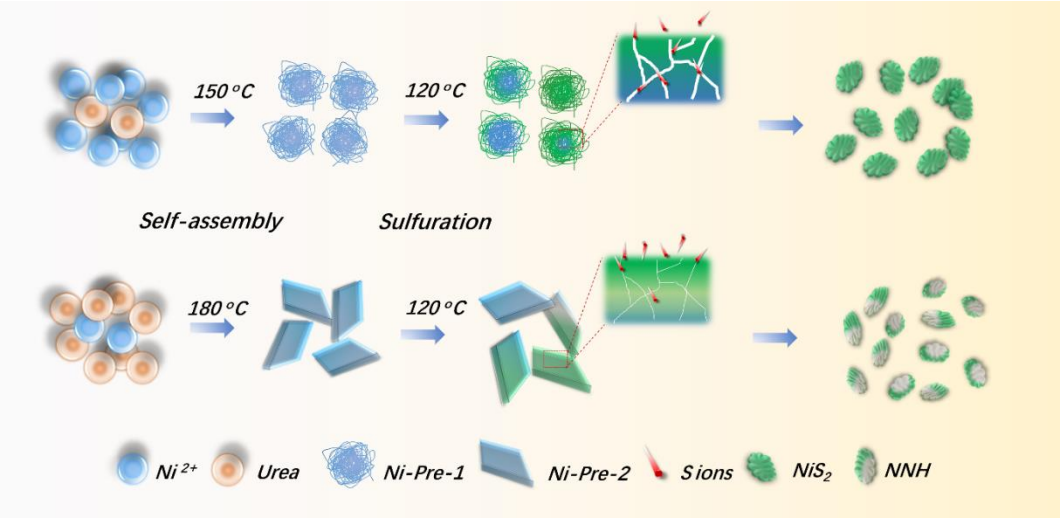

Figure 3.1 Schematic diagram of the synthetic mechanism for NNH and NiS_2.

The crystal structures of the as-designed products were characterized by XRD (Figure 3.2b). The XRD patterns indicated the successful syntheses of pure NiS_2 (JCPDS No. 65-3325), NiS (JCPDS No. 12-0041), and NNH consisting of NiS_2 (JCPDS No. 65-3325) and NiS (JCPDS Nos. 02-1280 and 12-0041). The molar ratio of NiS_2 to NiS within the NNH sample was further evaluated to be 1:1 by thermogravimetric analysis (TGA), as

shown in Figure 3.2c (the detailed calculation is shown in Experimental Section). The structural features of the as-prepared samples were investigated by Raman spectroscopy. As shown in Figure 3.2d, the NiS_2 sample exhibited characteristic peaks at 476 and 557 cm^{-1}, and the NiS sample exhibited several characteristic peaks with two dominant peaks at 238 and 342 cm^{-1}.[14, 40, 41] Contrarily, the NNH sample exhibited a wide-ranging peak around 493 cm^{-1} and an unintelligible peak around 200 cm^{-1}, which are likely due to the approximately equivalent contributions from NiS_2 and NiS.[42]

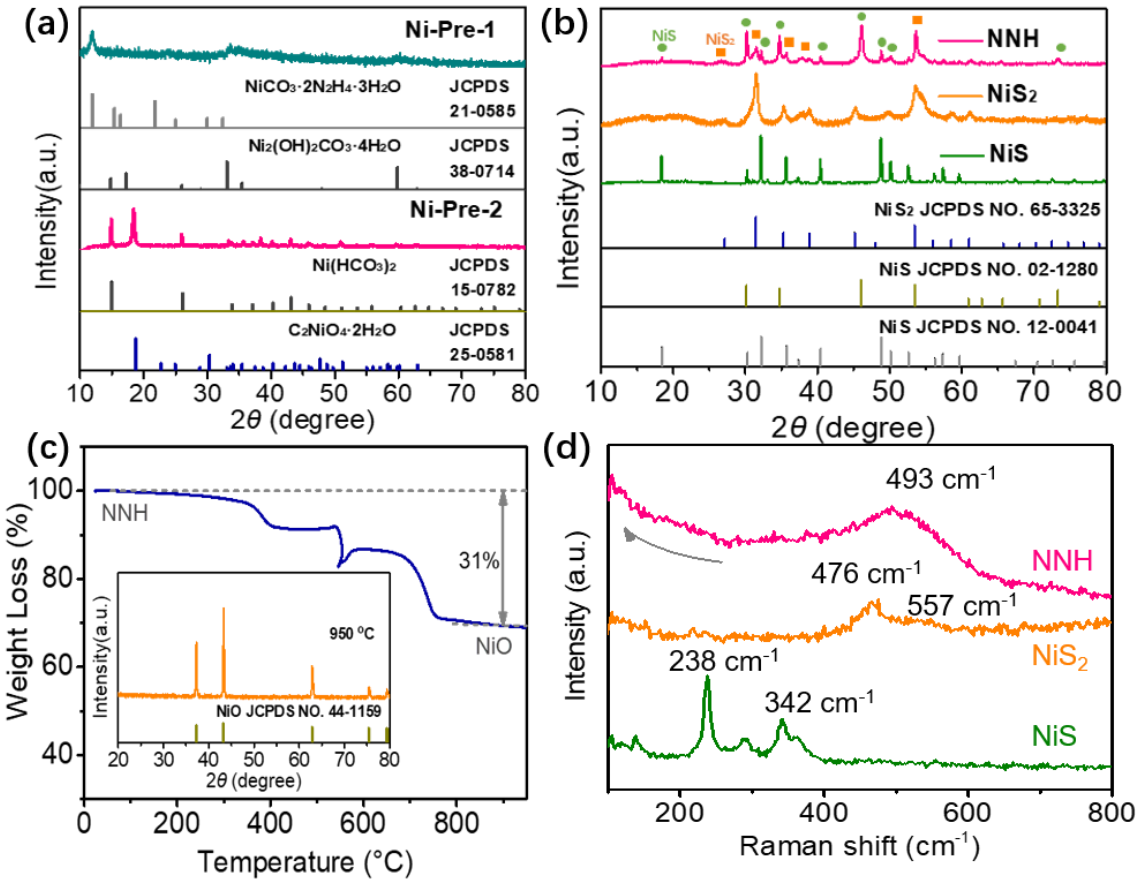

Figure 3.2 XRD patterns of (a) Ni-Pre-1/2, (b) of NNH, NiS_2, and NiS. (c) TG curve of NNH. (d) Raman spectra of NNH, NiS_2, and NiS.

The intriguing morphologies and structures of the as-prepared products were investigated by scanning electron microscopy (SEM, **Figure 3.3**). The NNH nanoparticles were observed to exhibit a fluffy morphology of ~100 nm, while the NiS_2 sample agglomerated into a larger size, which was mainly due to the different specific surface areas of the precursors (**Figure 3.4**). It was expected that Ni-Pre-1 with larger specific surface area (216.5 m^2g^{-1}) afforded more channels for the transport of the S ions for the subsequent full sulfurization to form NiS_2 (Figure 3.3b), while Ni-Pre-2 (22.0

m^2g^{-1}) reduced the immersion of the S ions, thus reducing the degree of sulfurization to form NNH (Figure 3.3a). Hence, a uniform NNH nanoparticle was successfully formed in-situ by engineering the structure of the precursors. For comparison, pure NiS was obtained by calcinating the as-prepared NiS_2 sample (Figure 3.3c). Additionally, the different morphologies of the cocatalysts could significantly influence PEC-HER performance. The fluffy NNH (25.4 m^2g^{-1}) possessed the largest surface area, followed by the agglomerated NiS_2 (19.9 m^2g^{-1}) and the blocky NiS (6.2 m^2g^{-1}), as confirmed by the N_2 adsorption–desorption measurements shown in **Figure 3.5**. Thus, the larger surface area, the more exposed active sites would be, and this corresponds to the improved catalytic activities of NNH/Si for PEC-HER.

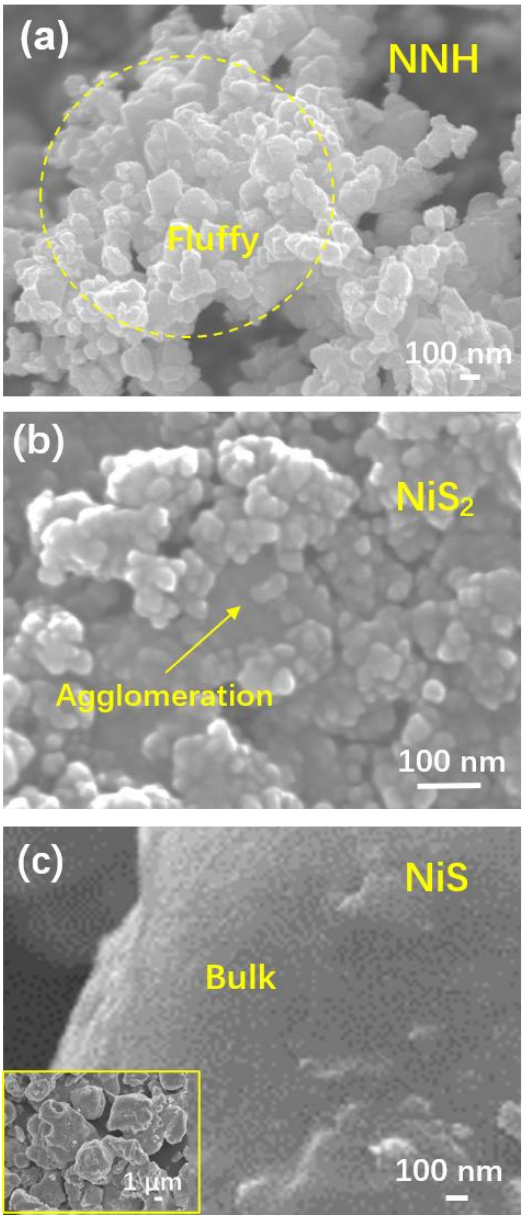

Figure 3.3 SEM images of (a) NNH, (b) NiS_2, and (c) NiS.

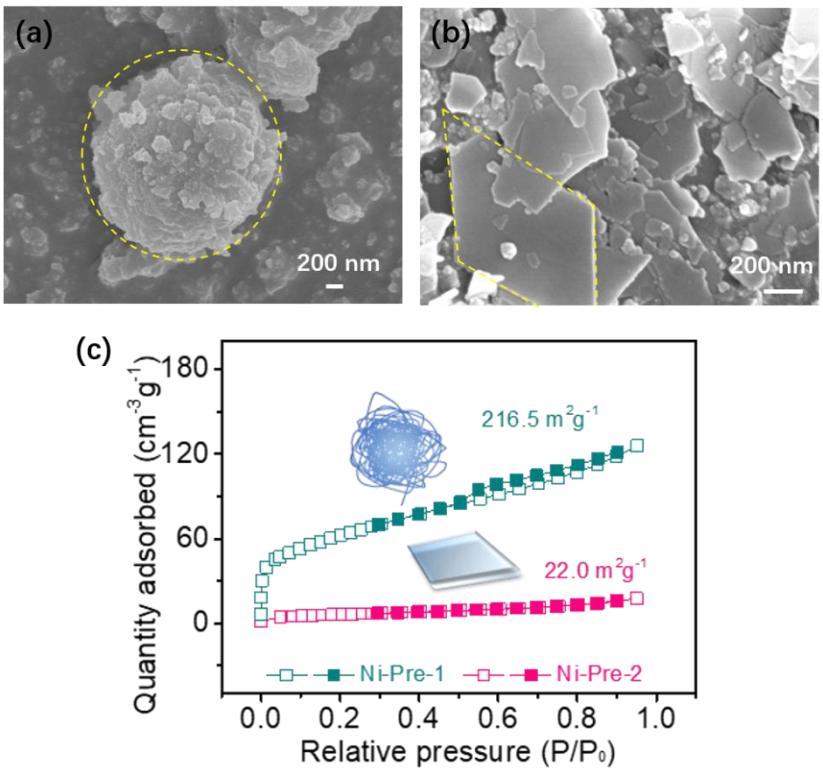

Figure 3.4. SEM images of (a) Ni-Pre-1 and (b) Ni-Pre-2, and their (c) N_2 adsorption and desorption isotherms curves.

The corresponding high-resolution transmission electron microscopy (HR-TEM) images were further investigated to determine the detailed internal structures of the as-prepared materials and constructed heterogenic NNH. In **Figure 3.6**c (showing the hexagonal phase of NiS), it is clear that the d-space (0.24 nm) was associated with the (220) plane. As shown in Figure 3.6b, NiS_2 exhibited different light and dark distributions, which represent the agglomeration edge between the particles. Their lattice spacings were ~0.33 and 0.25 nm, matching the (111) and (210) faces of the cubic-phase NiS_2, respectively. In the case of NNH (Figure 3.6a), the d-spaces of 0.20 and 0.54 nm were matched with the (102) face of NiS and (100) face of the NiS_2, respectively. Therefore, the intimate contact of the two distinct phases of NiS_2 and NiS within the NNH sample were distinguished by their corresponding lattice spacings, which is expected to improve the PEC-HER properties through the so-called "synergistic effect."[31] Furthermore, the surface defects in the NiS_2 phase could be identified in the NNH sample (inset of Figure 3.6a). Such an exposed defect domain, as a derivation of the catalytic properties of metal-based materials, not only favored an improved electron transfer rate; it also generated additional effective active sites for PEC-HER.[43-45] Compared with the selected area electron diffraction (SAED) images of the pure-phase NiS_2 or NiS (insets of Figures 3.6b

and 3.6c), the diffraction rings of NNH were indexed to (100), (111), and (221) for NiS_2, and those of NiS (300) and (211) are displayed in **Figure 3.7**a. Moreover, the elemental mapping images (Figure 3.7b–d) of NNH revealed a uniform distribution of the Ni element (red) and the evident inhomogeneous distribution of the S element (green) in the host structure in which the density of the S element was equal to that of the Ni element in some areas, while it was significantly denser than the Ni element in the other adjacent areas. It was also confirmed that NiS_2 and NiS were distributed within NNH in divergent patterns.

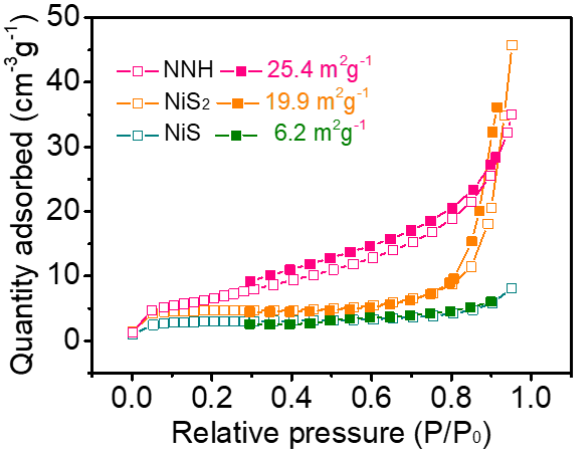

Figure 3.5 N_2 adsorption and desorption isotherms curves of the NNH, NiS_2, and NiS.

X-ray photoelectron spectroscopy (XPS) was employed to observe the chemical bonding states and surface elements of the as-prepared materials. All the observed signals of the Ni and S elements were compared, as displayed in the survey spectra of NiS_2, NiS, and NNH in **Figure 3.8**. The high-resolution Ni 2p peaks (**Figure 3.9**a) could be deconvoluted into two doublets (Ni $2p_{1/2}$ and Ni $2p_{3/2}$) and two satellites (named "Sat.") by the Gaussian fitting method.[46] The two peaks at ~871.4 and 853.6 eV corresponded to Ni^{2+}–S_2^{2-}, while the two other peaks around 874.0 and 855.9 eV were attributed to Ni^{2+}–S^{2-}. Compared with Ni^{2+}–S_2^{2-} and Ni^{2+}–S^{2-} (the dominant peaks in pure NiS_2 and NiS), the peak intensities of Ni^{2+}–S_2^{2-} and Ni^{2+}–S^{2-} were similar in the as-prepared NNH sample. For the S 2p peaks (Figure 3.9b), the peaks located at ~161.2 ($2p_{1/2}$) and 160.5 eV ($2p_{3/2}$) were ascribed to S^{2-}, while the peaks centered at ~163.4 ($2p_{1/2}$) and 162.1 eV ($2p_{3/2}$) corresponded to S_2^{2-}, which comply with the results of reported research.[28] Additionally, the peaks at ~168.1 eV were associated with the S–O species because of oxidation in the air.[47] Similar to the analyses of the Ni 2p peaks, the main peaks in NiS_2 matched with those of S_2^{2-}, although the characteristic peaks of S^{2-} in NiS demonstrated

the leading role. Moreover, the peaks, S^{2-} and S_2^{2-}, in the NNH sample were well-matched regarding their intensities, thus demonstrating the equal coexistence of the NiS_2 and NiS phases in the as-prepared NNH, and this is consistent with the aforementioned characteristics. Therefore, Ni^{2+}–S_2^{2-} in the defect-rich NiS_2 phase within NNH was the key active sites-rich cocatalyst, and Ni^{2+}–S^{2-} in the NiS phase significantly favored the charge transfer. Furthermore, the close synergistic effect of the Ni^{2+}–S_2^{2-} and Ni^{2+}–S^{2-} species might also account for the accelerated PEC-HER kinetics, which would be confirmed below.

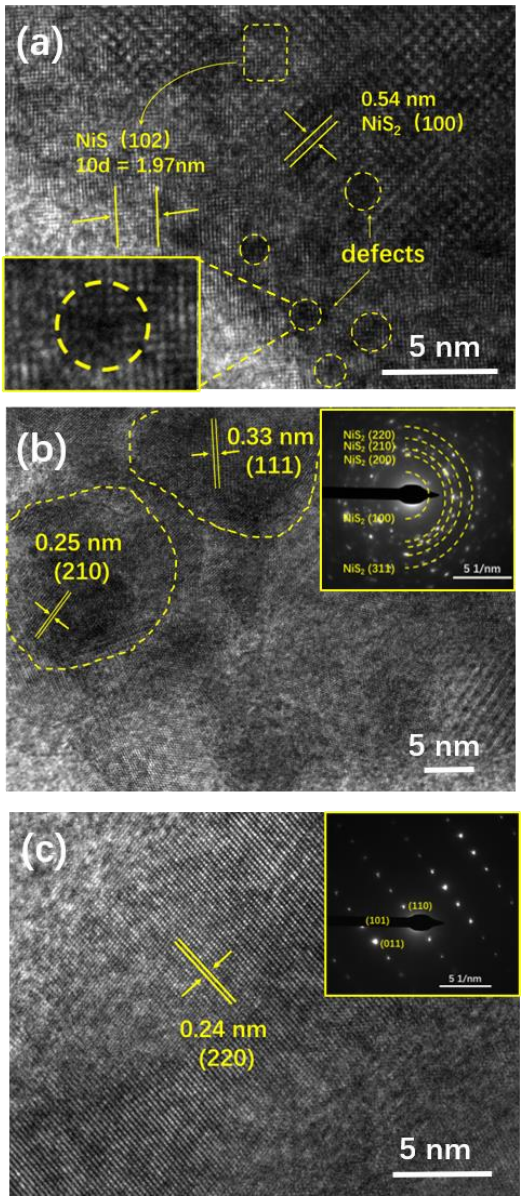

Figure 3.6 HR-TEM images and the corresponding the SAED images inset of (a) NNH, (b) NiS_2, and (c) NiS.

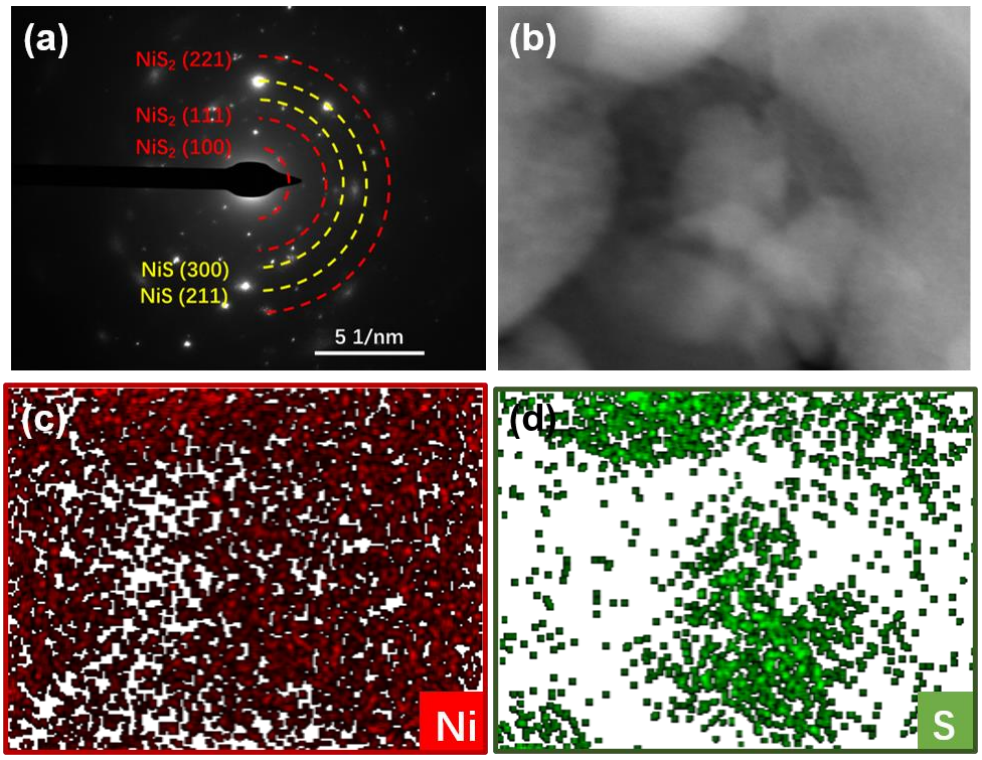

Figure 3.7 (a) SAED image and (b-d) the element mappings of NNH.

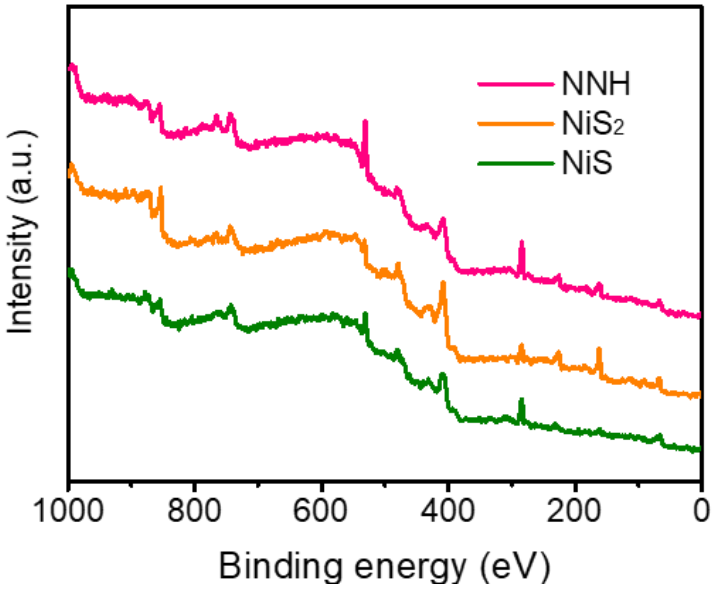

Figure 3.8 The XPS survey spectra of NNH, NiS_2, and NiS.

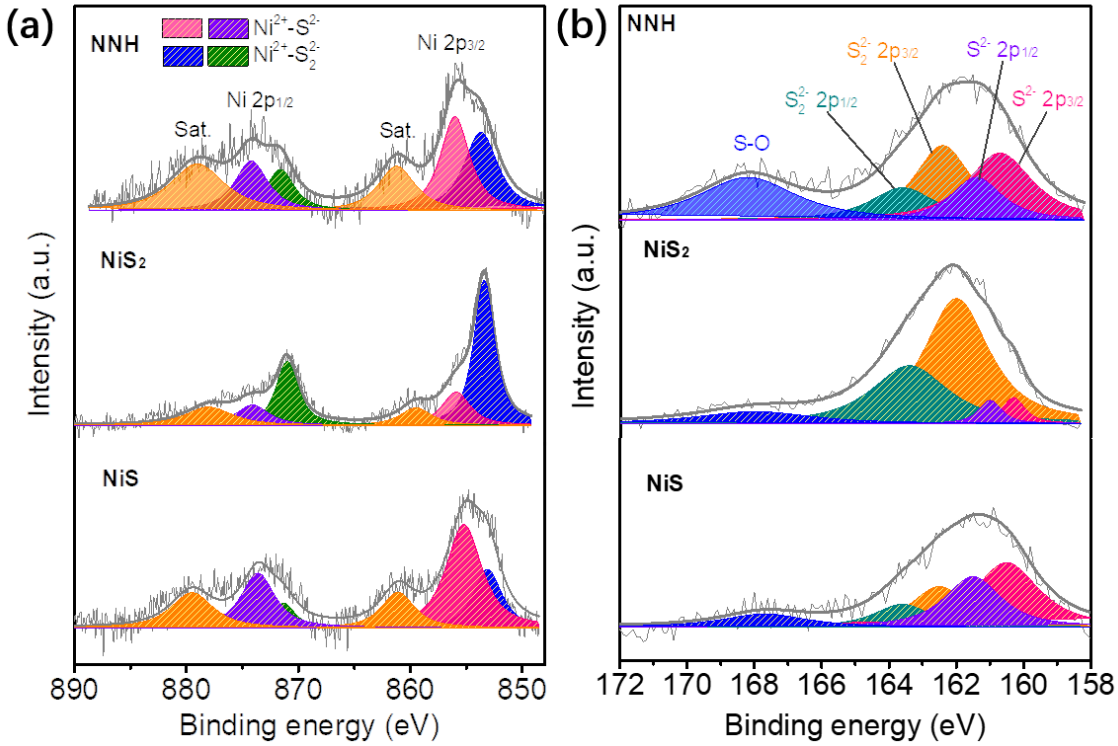

Figure 3.9 XPS spectra of NNH, NiS_2, and NiS: (a)Ni 2p, (b)S 2p.

3.3.2 PEC-HER performances

Following the full characterizations, NiS, NiS_2, and NNH were drop-casted as cocatalysts onto the planar p-Si photocathodes (the corresponding SEM images are shown in **Figure 3.10**) study the solar-driven hydrogen evolution. The PEC performances of NNH/Si, NiS_2/Si, NiS/Si, as well as the bare Si photocathodes for HER were investigated utilizing the linear sweep voltammetry (LSV) curves obtained in a 0.5 M H_2SO_4 electrolyte under 100 mW cm^{-2} (1 sun) illumination (**Figure 3.11**a). No current was detected for any photocathode under the dark condition. Compared with the onset potential at −0.08 V_{RHE} of the bare Si photocathode, those of the NiS/Si and NiS_2/Si photocathodes demonstrated positive shifts around +0.05 and +0.20 V_{RHE}, respectively (Figure 3.11b). However, the saturated photocurrent of the NiS/Si photocathode was 33.4 mA cm^{-2} at −0.50 V_{RHE}, which was higher than that of the NiS_2/Si photocathode (28.2 mA cm^{-2} at −0.34 V_{RHE}). It is known that a low onset voltage and high saturated current density would imply that high incoming light reached the Si semiconductor but with a less-valid catalytic activity, indicating that a single cocatalyst generally features its drawbacks because of the intrinsic difference in the catalytic property. Alternatively, the as-grown NNH/Si photocathode harmonized the properties of the NiS/Si and NiS_2/Si

photocathodes and was demonstrated a considerably enhanced PEC-HER activity with a saturated photocurrent of 30.2 mA cm^{-2} at −0.23 V_{RHE}, and the photocurrent increased to 18.9 mA cm^{-2} at 0 V_{RHE} and a 0.9% HC-STH. Moreover, the onset potential (Figure 3.11b) positively shifted to +0.28 V_{RHE}, which was 0.08 and 0.23 V more positive than the NiS_2/Si and NiS/Si photocathodes, respectively.

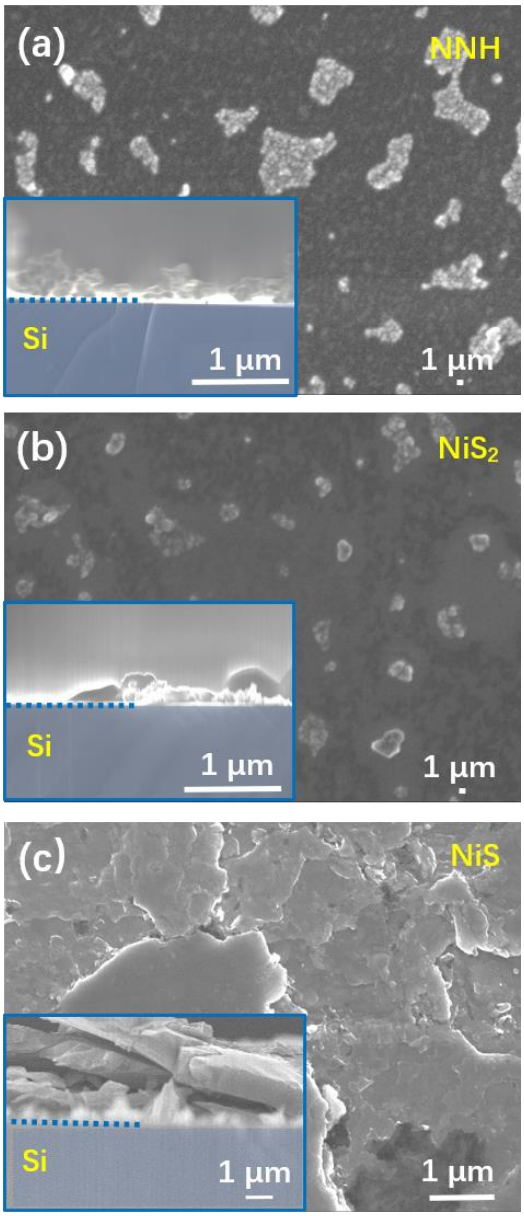

Figure 3.10 SEM images of (a)NNH/Si, (b) NiS_2/Si and (c) NiS/Si.

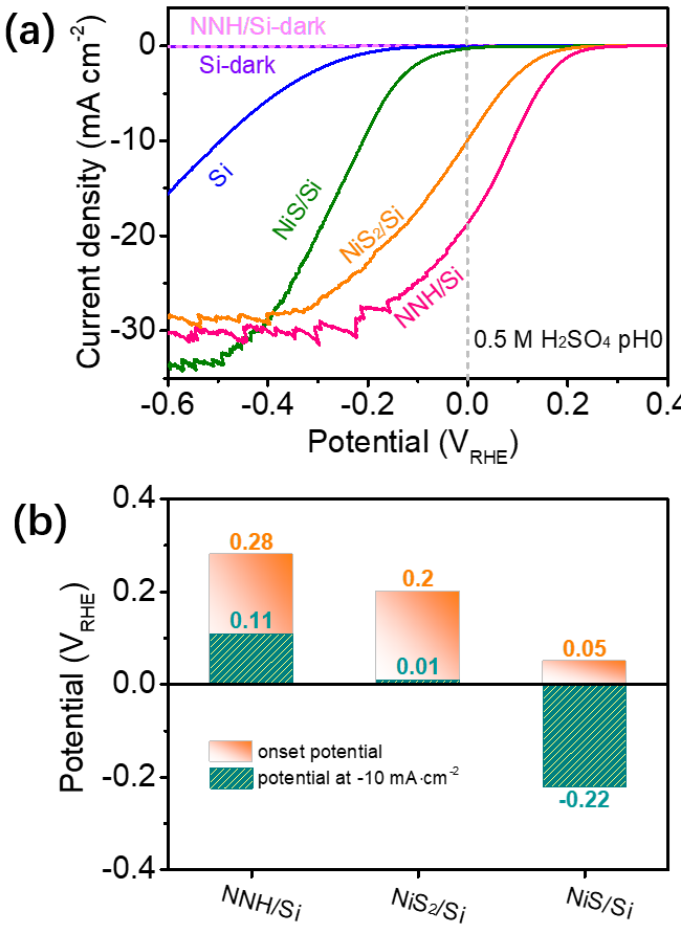

Figure 3.11 (a) LSV curves, (b) comparation of onset potential and the potential at −10 mA cm^{-2}.

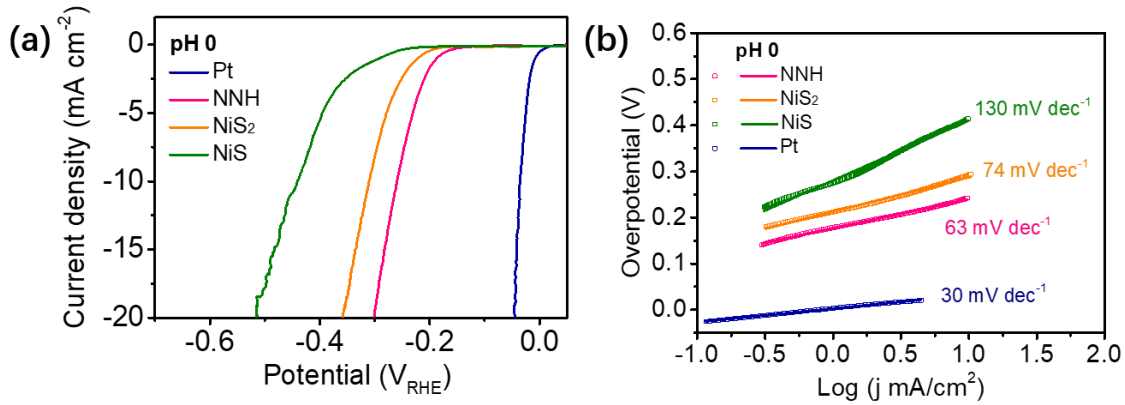

Figure 3.12 (a) LSV curves and (b) Tafel plots of NNH, NiS_2, NiS and Pt in 0.5 M H_2SO_4 at pH 0.

Actually, NNH and NiS_2 could function as efficient cocatalysts for EC-HER (**Figure 3.12**). In the 0.5 M H_2SO_4 electrolyte, NNH (−248 mV at −10 mA cm^{-2}) exhibited a reduced overpotential of 30 mV compared with that of NiS_2 (−277 mV at −10 mA cm^{-2}).

However, the reduced overpotential (30 mV) in EC-HER was significantly smaller than that in PEC HER (100 mV) for NNH/Si (+110 mV at −10 mA cm^{-2}) compared with that of NiS_2/Si (+10 mV at −10 mA cm^{-2}). The more favorable performances of PEC-HER compared with those of EC-HER employing NNH and NiS_2 are potentially due to the heterostructure of NNH, which could effectively modify the surface band bending of planar p-Si for progressive electron transfer. The PEC-HER performance of the NNH/Si photocathode in this work was compared with those of other Ni-based cocatalysts on the Si photocathodes, as summarized in **Table 3.1**. Without building the p-n junction in the Si photocathode and employing extra supports, such as a Ti layer, as the adhesion and protection layers, the PEC-HER performance of the NNH/Si photocathode exhibited unsurpassed compatibility between the planar p-Si semiconductor and NiS_x cocatalyst, which could significantly simplify the processing of the Si wafer and reduce the costs for favorable industrialization. Additionally, the current–time profiles at 0 V_{RHE} of the as-prepared samples indicate that the durability of NNH/Si for >7 h is much better than those of the other two photocathodes (**Figure 3.13**). It was observed that there was largely no shift in the Ni 2p peaks in XPS spectra after the catalytic process (**Figure 3.14**), indicating the considerable stability of the cocatalyst, NNH. Moreover, a recession still occurred at the later period because of the detachment of a certain amount of the NNH cocatalyst from the planar p-Si wafer after a prolonged catalytic process, as confirmed by the contrast SEM images of the NNH/Si photocathode before and after the current–time test for 7 h (**Figure 3.15**).

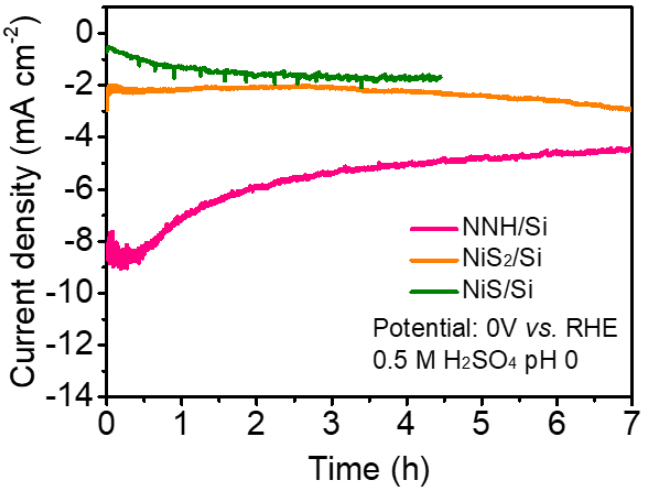

Figure 3.13 Current-time profiles of NNH/Si, NiS_2/Si, and NiS/Si at a constant potential of 0 V_{RHE}.

Table 3.1 Summary of Ni-based PEC catalysts for HER. [a]

Ni-based catalysts	Geometry of Si	J_{0V} (mA cm^{-2}) AM 1.5G (100 mW cm^{-2})	V_{op} (V_{RHE})	pH	Ref.
MoS_2/Ni_3S_2	n^+np^+-Si/Ni	41.5	0.54	13.6	47
Ni-rich NiO_x	n^+p-Si	20	0.55	14	14
NiS_xO_y	n^+p-Si/Ti	26	0.5	14	48
NiP_2	pn^+-Si/Ti	12	0.41	0	18
Ni-Fe layered double hydroxide	pn^+-Si	7	~0.3	14	11
Ni-Mo/TiO_2	n^+p-Si MWs	14.3	0.42	0	12
Ni-Mo	n^+p-Si MWs	9.1	0.46	4.5	13
Ni-Mo	p^+-Si MWs	6.8	0.145	4.5	49
$Ni_{12}P_5$	p-Si MWs	21	0.4	0	50
Ni-B	p-Si MWs	15.6	0.44	7	51
NiS	p-Si MWs	10	0.2	0/14	33
$NiS_{1.97}$		5.3	0.2	0	
$NiCoSe_x$	p-Si NPs	37.5	0.25	0	52
Ni	p-Si/Ti (~225 mW cm^{-2})	~20	0.3	14	53
		~5	0.25	9.5	
Ni_3Se_2/Co_9S_8/EG	MSi	2.68 (-0.6 V)	0.14	14	54
Ni_2P	p-Si	10	0.6	0	55
Pd-Ni/ CNT	p-Si	~13	~0.2	0	56
$Ni(TEOA)_2Cl_2$	p-Si	5.57	0.11	0.3	57
NNH	**planar p-Si**	**18.9**	**0.28 V**	**0**	**This work**

[a] Note, J_{0V} is the current density at an applied bias of 0 V_{RHE}; V_{op} is the onset potential; Si MWs are microwire array of silicon; Si NPs are nanopillar array of silicon; EG is the electrochemically exfoliated graphene; CNT is the carbon nanotube.

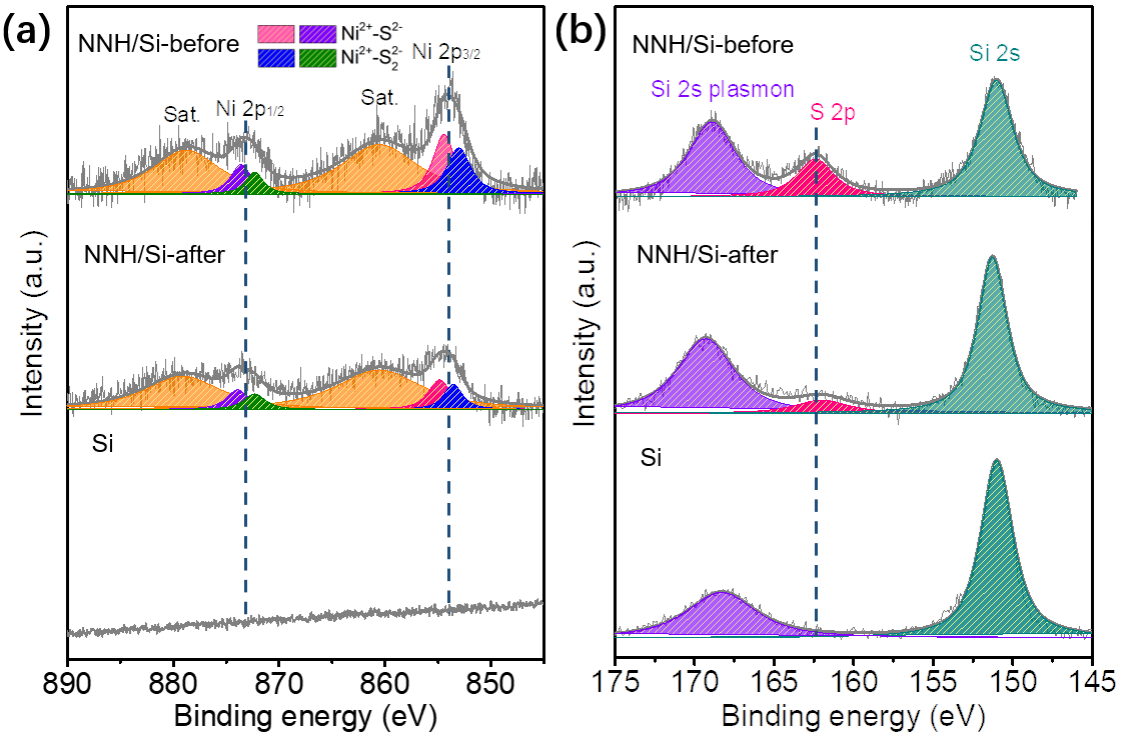

Figure 3.14 The contrast XPS spectra of bare Si and NNH/Si-before/after current-time test of 7 hours.

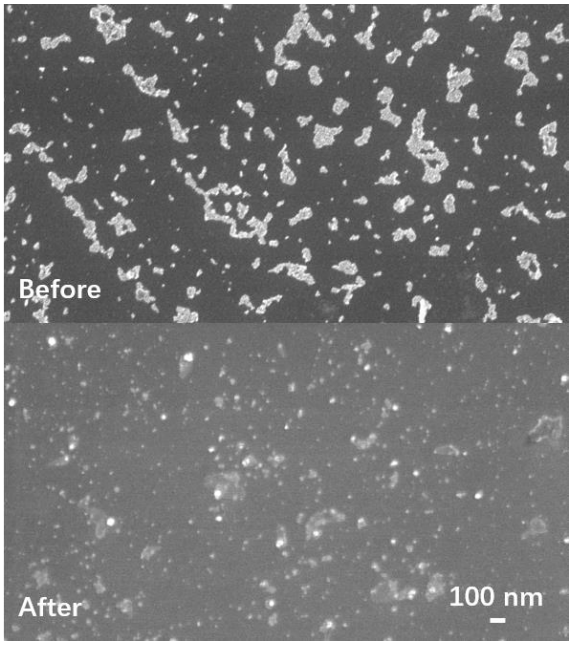

Figure 3.15 The contrast SEM images of NNH/Si before and after current–time test of 7 hours.

To confirm the PEC-HER property, the EIS spectra of the circuit model fitting at 0.24 V_{RHE} of the bare Si, NiS/Si, NiS_2/Si, and NNH/Si photocathodes are illustrated in **Figure 3.16**. The EIS spectrum of the bare Si photocathode displayed a single arc that

corresponded to the charge transfer to the electrolyte, which could be modeled with a capacitance of a constant phase element (CPE) consisting of a planar p-Si semiconductor (CPE_{Si}), and single series resistance, Rs, that are parallel to the charge-transfer resistance from planar p-Si to the cocatalyst to the electrolyte, $R_{ct, Si}$. Contrarily, the EIS spectra of the NiS/Si, NiS_2/Si, and NNH/Si photocathodes could be fitted to an equivalent circuit (inset of Figure 4d) utilizing CPE_{Si} and CPE of the cocatalyst ($CPE_{cocatalyst}$), Rs, and $R_{ct, Si}$, where the first arc in the high-frequency range represented the interface of the Si/cocatalyst ($R_{ct, Si}$), and the second in the low-frequency range corresponds to the interface of the cocatalyst/electrolyte ($R_{ct, cocatalyst}$), and this is consistent with the reported cocatalyst-semiconductor system.[5, 58, 59] Noteworthily, the $R_{(ct, Si)}$ and $R_{ct, cocatalyst}$ values reflected the efficient coupling of planar p-Si and cocatalyst and the catalytic property of the cocatalyst, respectively. The fitted $R_{(ct, Si)}$ and $R_{ct, cocatalyst}$ values are listed in **Table 3.2**. First, the NNH/Si photocathode exhibited a much lower R_{ct} (0.46 kΩ·cm^2) from NNH to the electrolyte ($R_{ct, cocatalyst}$) compared with those of NiS/Si (8.13 kΩ·cm^2) and NiS_2/Si (6.15 kΩ·cm^2), thus confirming the improved catalytic activities of NNH/Si for PEC HER, which correspond to the EC-HER measurement. Next, R_{ct} from planar p-Si to the NNH ($R_{ct, Si}$) of NNH/Si (0.41 kΩ·cm^2) was also much smaller compared with those of NiS/Si (3.53 kΩ·cm^2) and NiS_2/Si (2.31 kΩ·cm^2), probably because of the modification of the band bending of planar p-Si by the heterogenic configuration in NNH, which could promote electron transfer from the planar p-Si to the cocatalyst. Briefly, the improved PEC-HER performance of NNH/Si was not only due to the improved HER catalytic property of NNH. It was also due to the more efficient electron transfer from planar p-Si to the NNH cocatalyst compared with the single cocatalysts of NiS_2 or NiS on planar p-Si.

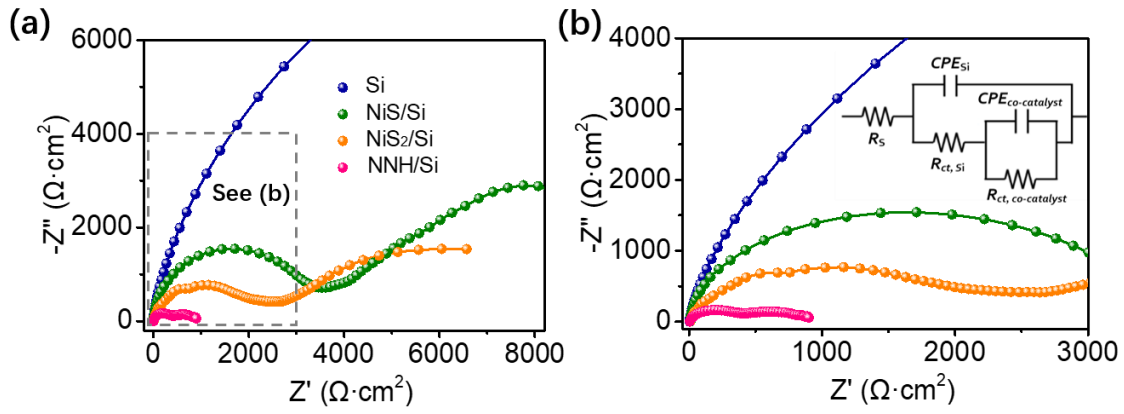

Figure 3.16 Nyquist plots of NNH/Si, NiS_2/Si, NiS/Si, and bare Si in 0.5 M H_2SO_4 at pH 0.

Table 3.2 The charge-transfer resistance values of NNH/Si, NiS_2/Si, and NiS/Si photocathodes.

Photocathodes	$R_{ct, Si}$ ($k\Omega \cdot cm^2$)	$R_{ct, co\text{-}catalyst}$ ($k\Omega \cdot cm^2$)
NNH/Si	0.41	0.46
NiS_2/Si	2.31	6.15
NiS/Si	3.53	8.13

To investigate the essential origin of NNH for the planar p-Si photocathode during the PEC-HER process, the band structures of the NiS_2 and NiS phases were first evaluated since the introduced n-type semiconducting cocatalysts on the surface of planar p-Si were expected to change the band bending and benefit the subsequent hydrogen evolution. The ultraviolet–visible (UV–Vis) absorption spectrum of NiS and its derived Tauc plot (**Figures 3.17**a–b) indicated that the band gap of NiS was ~2.2 eV, which is consistent with the evaluation employing the density functional theory (DFT) calculation from the Γ point in the Brillouin zone (**Figure 3.19**b). Its Fermi energy level (E_f) was ~0.1 V_{RHE}, as determined by the Mott–Schottky measurement (Figure 3.17c), which also confirmed that it exhibited an n-type semiconductor property (n-NiS). The valence-band maximum (VBM) was approximately a 1.5 eV gap from the E_f, as determined by VB XPS (Figure 3.17d) after the C 1s calibration (Figure 3.17e). These values suggested that VBM was at the 1.6 V_{RHE} position. Thereafter, the determined conduction-band minimum (CBM) was −0.6 V_{RHE}. Therefore, the band structure of NiS was fully ascertained, as shown in Figure 3.17f. Similarly, the band structure of NiS_2 is shown in **Figure 3.18**, where the n-type semiconducting NiS_2 (n-NiS_2) exhibited semi-metallic absorption with a small band gap (0.7 eV). The semi-metallic property of NiS_2 was presented at the Γ point in the Brillouin zone (Figure 3.19a), which is in good agreement with the increasing absorption peak at a wavelength that was >400 nm in the UV–vis spectrum (Figure 3.18a). E_f of n-NiS_2 was approximately −0.3 V_{RHE}, and VBM and CBM were observed at the 0.3 and −0.4 V_{RHE} positions, respectively. Notably, CB of n-NiS_2 was contributed by Ni and S, as shown by the partial density of states (DOSs) (Figure 3.19a), although CB of n-NiS was largely contributed by Ni, as shown by the partial DOS (Figure 3.19b). These results suggest that n-NiS_2 can transfer electrons to Ni and S, whereas n-NiS can only accept electrons from Ni. This will aid the explanation of the conceptual routes of electron transfer from the surface of planar p-Si to NNH by combining the n-NiS_2 and n-NiS phases.

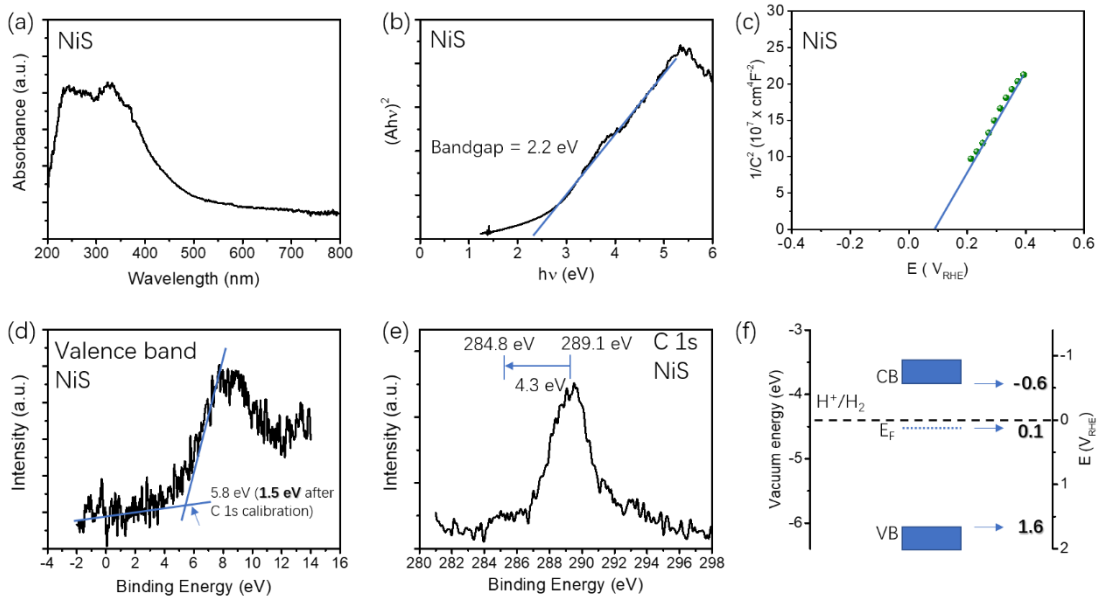

Figure 3.17. (a) The UV–vis absorption spectrum, (b) Tauc plot, (c) Mott-Schottky, (d) valence-band XPS, (e) C1s calibration and (f) band structure of NiS.

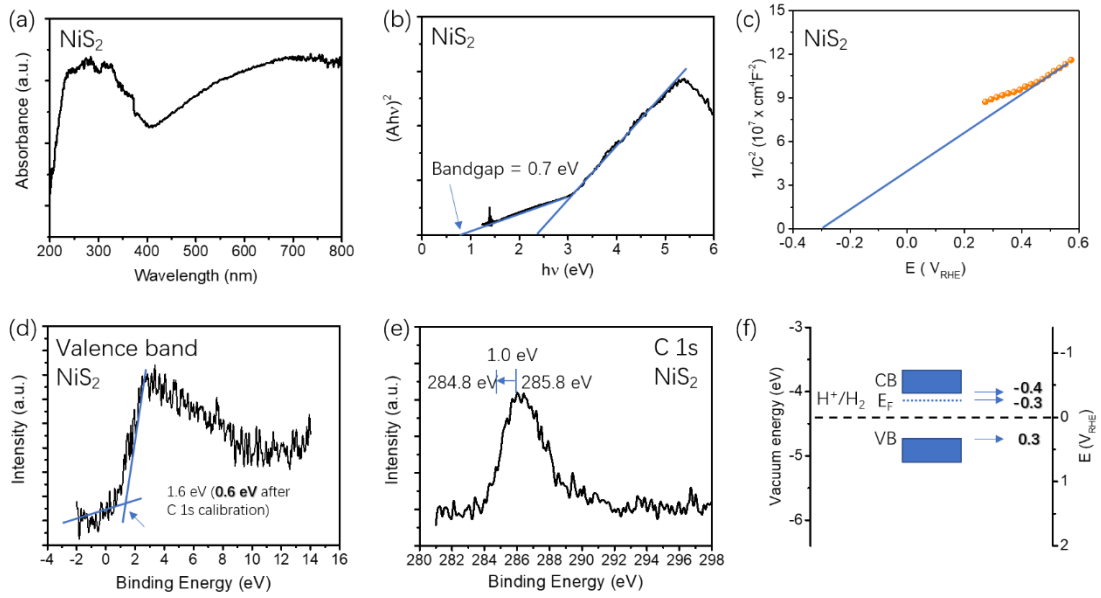

Figure 3.18 (a) The UV–vis absorption spectrum, (b) Tauc plot, (c) Mott–Schottky, (d) valence-band XPS, (e) C1s calibration and (f) band structure of NiS_2.

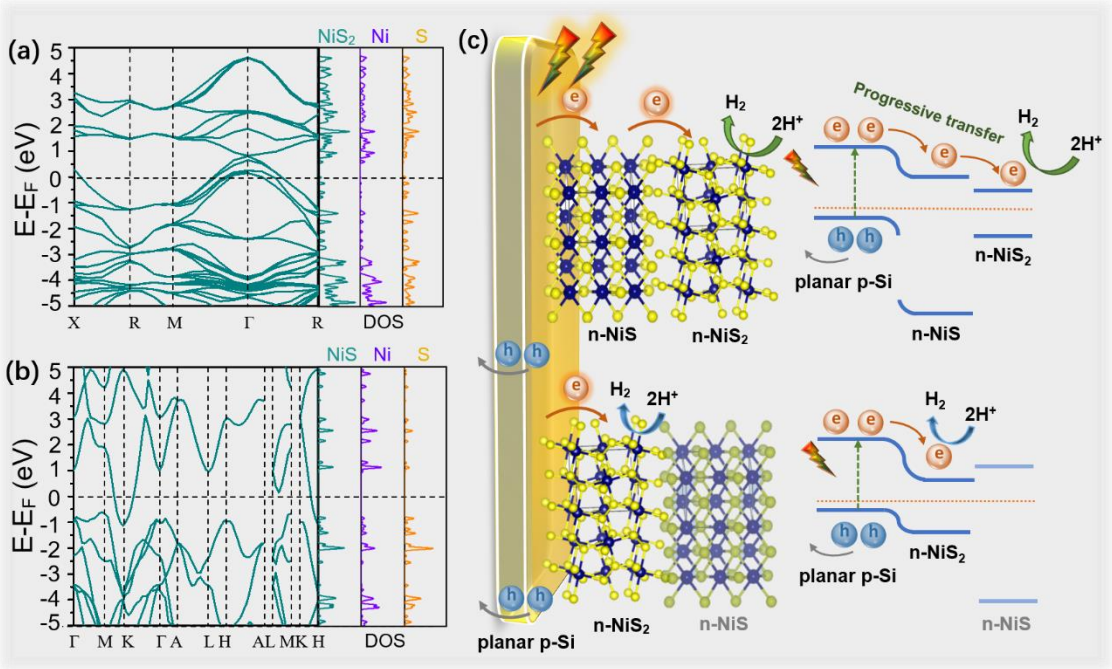

Figure 3.19 Band structure and DOS of (a) NiS_2 and (b) NiS, (c) Schematic diagram of the progressive electron transfer on NNH/Si photocathode for the enhance PEC-HER.

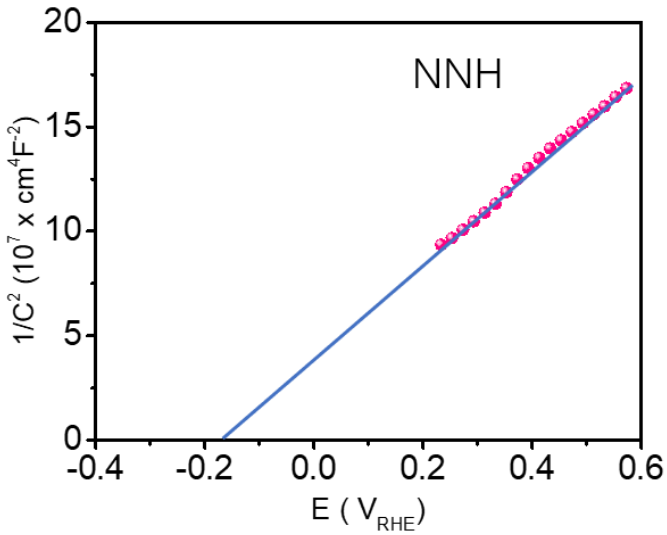

Figure 3.20 Mott–Schottky of NNH.

Based on the well-evaluated band structures of NiS and NiS_2, we further investigated how planar p-Si interacts with the NNH composite, which is formed in-situ as a heterojunction. The Mott–Schottky measurement of NNH (**Figure 3.20**) indicated that it is an n-type semiconducting cocatalyst (n-NNH) with E_f of approximately −0.2 V_{RHE}. When n-NNH was drop-casted onto planar p-Si as a cocatalyst, there were two main interphase-contacts, p-Si/n-NiS/n-NiS_2 and p-Si/n-NiS_2/n-NiS, since the n-NNH

nanoparticles were randomly disposed on the p-Si surface (**Figure 3.21**) and the divergent distributions of the n-NiS and n-NiS_2 phases within n-NNH, as shown by the HR-TEM images of NNH (Figure 3.6a).

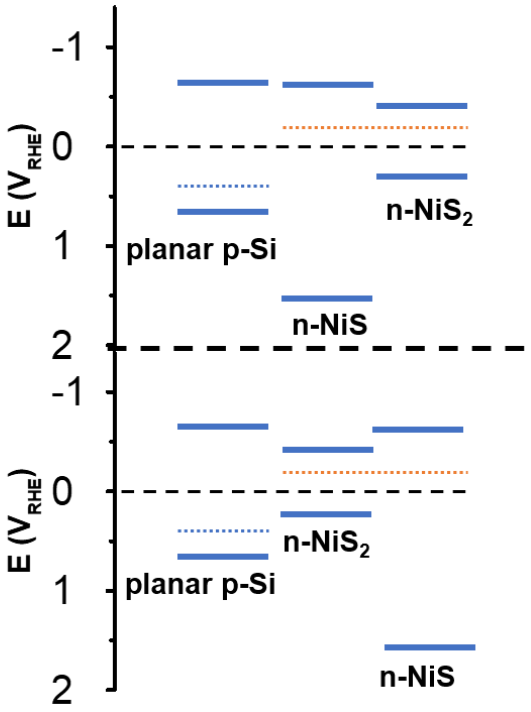

Figure 3.21 Schematic band energy diagram of NNH/Si photocathode before contact.

The enhancement of PEC-HER by the NNH/Si photocathode originated from the interphase-contact, p-Si/n-NiS/n-NiS_2. Accordingly, as shown in the top half of Figure 3.19c, the contact of n-NiS with planar p-Si induced a local electric field with direction from n-NiS to planar p-Si, which caused the local downward band bending of planar p-Si under dark conditions because of their different E_{fs}.[55] The photogenerated electrons would be promoted by this local electric field upon solar light illumination to be transferred from planar p-Si to n-NiS, and subsequently to n-NiS_2, which was active for HER. n-NiS acted as a progressive medium for enhanced electron transfer from CB of planar p-Si to n-NiS_2. Regarding the p-Si/n-NiS_2/n-NiS interphase contact (bottom-half of Figure 3.19c), the photoexcited electrons were transferred from planar p-Si to the exposed edges of n-NiS_2, although they will not transfer further to n-NiS because CBM of n-NiS_2 is more negative than that of n-NiS, which behaves as the NiS_2/Si photocathode with a single p-Si/n-NiS_2 interphase contact. Compared with the direct transfer of an electron from planar p-Si to n-NiS_2, the buffering effect of n-NiS afforded a large driving force for charge-carrier separation and transfer with a much lowered R_{ct}, as demonstrated

in the foregoing EIS analyses, and simultaneously increased the energy barrier for the anti-recombination of the photoexcited electron-hole pairs in this space-charge region, which may principally account for the enhanced PEC activity toward HER.[57] Detailly, after inducing a local electric field and functioning as a progressive electron transfer medium via n-NiS, the photogenerated electron could be rapidly transferred from planar p-Si to Ni^{2+} of the n-NiS phase within n-NNH, and subsequently to Ni^{2+} or $(S_2)^{2-}$ of the defect-rich n-NiS_2 phase within n-NNH, as confirmed by the partial DOSs (Figures 3.19a and 3.19b).

3.4 Conclusions

Summarily, the adequate coupling of the planar p-Si photocathode with NNH (an efficient cocatalyst) was investigated for water splitting for enhanced PEC-HER performance. By tuning the structure of the precursors, NNH was successfully grown in-situ, including the defect-rich NiS_2 (the active sites for HER) and the NiS (the medium for progressive electron transfer) phases. The designed NNH/Si photocathode exhibited excellent performance in 0.5 M H_2SO_4 under solar irradiation regarding the onset potential (0.28 V_{RHE}) and photocurrent density (−18.9 $mAcm^{-2}$ at 0 V_{RHE}). This study establishes a firm foundation to explore more earth-abundant metal sulfides for high-performance PEC-HER systems that are based on the planar Si photoelectrodes for progressive electron transfer by the appropriate engineering of heterostructures.

References

1. I. Roger, M.A. Shipman, M.D. Symes, Earth-abundant catalysts for electrochemical and photoelectrochemical water splitting. *Nat. Rev. Chem.,* **2017**, *1* (1), 0003.
2. E. Samuel, B. Joshi, M.-W. Kim, M.T. Swihart, S.S. Yoon, Morphology engineering of photoelectrodes for efficient photoelectrochemical water splitting. *Nano Energy,* **2020**, *72*, 104648.
3. R. Fan, Z. Mi, M. Shen, Silicon based photoelectrodes for photoelectrochemical water splitting. *Opt. Express,* **2019**, *27* (4), A51-A80.
4. K. Sivula, R. van de Krol, Semiconducting materials for photoelectrochemical energy conversion. *Nat. Rev. Mater. ,* **2016**, *1* (2), 15010.
5. Q. Ding, F. Meng, C.R. English, M. Cabán-Acevedo, M.J. Shearer, D. Liang, A.S. Daniel, R.J. Hamers, S. Jin, Efficient Photoelectrochemical Hydrogen Generation

Using Heterostructures of Si and Chemically Exfoliated Metallic MoS_2. *J. Am. Chem. Soc.,* **2014**, *136* (24), 8504-8507.

6. Y. Hou, B.L. Abrams, P.C.K. Vesborg, M.E. Björketun, K. Herbst, L. Bech, A.M. Setti, C.D. Damsgaard, T. Pedersen, O. Hansen, J. Rossmeisl, S. Dahl, J.K. Nørskov, I. Chorkendorff, Bioinspired molecular co-catalysts bonded to a silicon photocathode for solar hydrogen evolution. *Nat. Mater.,* **2011**, *10* (6), 434-438.
7. H. Lin, S. Li, G. Yang, K. Zhang, D. Tang, Y. Su, Y. Li, S. Luo, K. Chang, J. Ye, In Situ Assembly of MoS_x Thin-Film through Self-Reduction on p-Si for Drastic Enhancement of Photoelectrochemical Hydrogen Evolution. *Adv. Funct. Mater.,* **2020**, *31*(3), 2007071.
8. L. Ji, C. Lv, Z. Chen, Z. Huang, C. Zhang, Nickel-Based (Photo)Electrocatalysts for Hydrogen Production. *Adv. Mater.,* **2018**, *30* (17), 1705653.
9. D. Li, J. Shi, C. Li, Transition-Metal-Based Electrocatalysts as Cocatalysts for Photoelectrochemical Water Splitting: A Mini Review. *Small,* **2018**, *14* (23), 1704179.
10. Z. Luo, B. Liu, H. Li, X. Chang, W. Zhu, T. Wang, J. Gong, Multifunctional Nickel Film Protected n-Type Silicon Photoanode with High Photovoltage for Efficient and Stable Oxygen Evolution Reaction. *Small Methods,* **2019**, *3* (10), 1900212.
11. J. Zhao, L. Cai, H. Li, X. Shi, X. Zheng, Stabilizing Silicon Photocathodes by Solution-Deposited Ni–Fe Layered Double Hydroxide for Efficient Hydrogen Evolution in Alkaline Media. *ACS Energy Lett.,* **2017**, *2* (9), 1939-1946.
12. M.R. Shaner, J.R. McKone, H.B. Gray, N.S. Lewis, Functional integration of Ni–Mo electrocatalysts with Si microwire array photocathodes to simultaneously achieve high fill factors and light-limited photocurrent densities for solar-driven hydrogen evolution. *Energy Environ. Sci. ,* **2015**, *8* (10), 2977-2984.
13. E.L. Warren, J.R. McKone, H.A. Atwater, H.B. Gray, N.S. Lewis, Hydrogen-evolution characteristics of Ni–Mo-coated, radial junction, n^+p-silicon microwire array photocathodes. *Energy Environ. Sci. ,* **2012**, *5* (11), 9653-9661.
14. J.-Y. Jung, J.-Y. Yu, S. Yoon, B. Yoo, J.-H. Lee, Charge Transfer Kinetics of Photo-Electrochemical Hydrogen Evolution Improved by Nonstoichiometric Ni-rich NiO_x-Coated Si Photocathode in Alkaline Electrolyte. *Adv. Sust. Syst.,* **2018**, *2* (2), 1700138.

15. J. Lin, P. Wang, H. Wang, C. Li, X. Si, J. Qi, J. Cao, Z. Zhong, W. Fei, J. Feng, Defect-Rich Heterogeneous MoS_2/NiS_2 Nanosheets Electrocatalysts for Efficient Overall Water Splitting. *Adv. Sci.,* **2019**, *6* (14), 1900246.

16. R. Fan, G. Huang, Y. Wang, Z. Mi, M. Shen, Efficient n^+p-Si photocathodes for solar H_2 production catalyzed by Co-W-S and stabilized by Ti buffer layer. *Appl. Catal. B Environ.,* **2018**, *237*, 158-165.

17. S.K. Choi, G. Piao, W. Choi, H. Park, Highly efficient hydrogen production using p-Si wire arrays and NiMoZn heterojunction photocathodes. *Appl. Catal. B Environ.,* **2017**, *217*, 615-621.

18. F. Chen, Q. Zhu, Y. Wang, W. Cui, X. Su, Y. Li, Efficient Photoelectrochemical Hydrogen Evolution on Silicon Photocathodes Interfaced with Nanostructured NiP_2 Cocatalyst Films. *ACS Appl. Mater. Interfaces,* **2016**, *8* (45), 31025-31031.

19. S. Li, P. Zhang, X. Xie, X. Song, J. Liu, L. Zhao, H. Chen, L. Gao, Enhanced photoelectrochemical performance of planar p-Silicon by APCVD deposition of surface mesoporous hematite coating. *Appl. Catal. B Environ.,* **2017**, *200*, 372-377.

20. Y. Guo, T. Park, J.W. Yi, J. Henzie, J. Kim, Z. Wang, B. Jiang, Y. Bando, Y. Sugahara, J. Tang, Y. Yamauchi, Nanoarchitectonics for Transition-Metal-Sulfide-Based Electrocatalysts for Water Splitting. *Adv. Mater.,* **2019**, *31* (17), 1807134.

21. Y. Hou, X. Zhuang, X. Feng, Recent Advances in Earth-Abundant Heterogeneous Electrocatalysts for Photoelectrochemical Water Splitting. *Small Methods,* **2017**, *1* (6), 1700090.

22. Y. Liu, Y. Dou, S. Li, T. Xia, Y. Xie, Y. Wang, W. Zhang, J. Wang, L. Huo, H. Zhao, Synergistic Interaction of Double/Simple Perovskite Heterostructure for Efficient Hydrogen Evolution Reaction at High Current Density. *Small Methods,* **2020**, *n/a* (n/a), 2000701.

23. S. Wang, Y. Wang, S.-Q. Zang, X.W. Lou, Hierarchical Hollow Heterostructures for Photocatalytic CO_2 Reduction and Water Splitting. *Small Methods,* **2020**, *4* (1), 1900586.

24. X.Y. Yu, X.W. Lou, Mixed Metal Sulfides for Electrochemical Energy Storage and Conversion. *Adv. Energy Mater.,* **2018**, *8* (3), 1701592.

25. S. Li, L. Zhang, W. Zhao, S. Yuan, L. Yang, X. Chen, P. Ge, W. Sun, X. Ji, Designing interfacial chemical bonds towards advanced metal-based energy-

storage/conversion materials. *Energy Storage Mater.,* **2020**, *32*, 477-496.

26. D.Y. Chung, J.W. Han, D.-H. Lim, J.-H. Jo, S.J. Yoo, H. Lee, Y.-E. Sung, Structure dependent active sites of NixSy as electrocatalysts for hydrogen evolution reaction. *Nanoscale,* **2015**, *7* (12), 5157-5163.

27. N. Jiang, Q. Tang, M. Sheng, B. You, D.-e. Jiang, Y. Sun, Nickel sulfides for electrocatalytic hydrogen evolution under alkaline conditions: a case study of crystalline NiS, NiS_2, and Ni_3S_2 nanoparticles. *Catal. Sci. Technol.,* **2016**, *6* (4), 1077-1084.

28. Q. Li, D. Wang, C. Han, X. Ma, Q. Lu, Z. Xing, X. Yang, Construction of amorphous interface in an interwoven NiS/NiS_2 structure for enhanced overall water splitting. *J. Mater. Chem. A,* **2018**, *6* (18), 8233-8237.

29. P. Luo, H. Zhang, L. Liu, Y. Zhang, J. Deng, C. Xu, N. Hu, Y. Wang, Targeted Synthesis of Unique Nickel Sulfide (NiS, NiS_2) Microarchitectures and the Applications for the Enhanced Water Splitting System. *ACS Appl. Mater. Interfaces,* **2017**, *9* (3), 2500-2508.

30. H. Pang, C. Wei, X. Li, G. Li, Y. Ma, S. Li, J. Chen, J. Zhang, Microwave-assisted synthesis of NiS_2 nanostructures for supercapacitors and cocatalytic enhancing photocatalytic H_2 production. *Sci. Rep.,* **2014**, *4* (1), 3577.

31. G. Zhou, Y. Chen, H. Dong, L. Xu, X. Liu, C. Ge, D. Sun, Y. Tang, Ultrafine monodisperse NiS/NiS2 heteronanoparticles in situ grown on N-doped graphene nanosheets with enhanced electrocatalytic activity for hydrogen evolution reaction. *Int. J. Hydrogen Energy,* **2019**, *44* (48), 26338-26346.

32. C. Tang, Z. Pu, Q. Liu, A.M. Asiri, X. Sun, NiS2 nanosheets array grown on carbon cloth as an efficient 3D hydrogen evolution cathode. *Electrochim. Acta,* **2015**, *153*, 508-514.

33. J. Yoo, I.H. Kwak, I.S. Kwon, K. Park, D. Kim, J.H. Lee, S.A. Lim, E.H. Cha, J. Park, Nickel sulfide nanocrystals for electrochemical and photoelectrochemical hydrogen generation. *J. Mater. Chem. C,* **2020**, *8* (9), 3240-3247.

34. Y.F. Tay, H. Kaneko, S.Y. Chiam, S. Lie, Q. Zheng, B. Wu, S.S. Hadke, Z. Su, P.S. Bassi, D. Bishop, T.C. Sum, T. Minegishi, J. Barber, K. Domen, L.H. Wong, Solution-Processed Cd-Substituted CZTS Photocathode for Efficient Solar Hydrogen Evolution from Neutral Water. *Joule,* **2018**, *2* (3), 537-548.

35. P. Giannozzi, S. Baroni, N. Bonini, M. Calandra, R. Car, C. Cavazzoni, D. Ceresoli, G.L. Chiarotti, M. Cococcioni, I. Dabo, A. Dal Corso, S. de Gironcoli, S. Fabris, G. Fratesi, R. Gebauer, U. Gerstmann, C. Gougoussis, A. Kokalj, M. Lazzeri, L. Martin-Samos, N. Marzari, F. Mauri, R. Mazzarello, S. Paolini, A. Pasquarello, L. Paulatto, C. Sbraccia, S. Scandolo, G. Sclauzero, A.P. Seitsonen, A. Smogunov, P. Umari, R.M. Wentzcovitch, QUANTUM ESPRESSO: a modular and open-source software project for quantum simulations of materials. *J. Phys. Condens. Matter,* **2009**, *21* (39), 395502.

36. P. Giannozzi, O. Andreussi, T. Brumme, O. Bunau, M. Buongiorno Nardelli, M. Calandra, R. Car, C. Cavazzoni, D. Ceresoli, M. Cococcioni, N. Colonna, I. Carnimeo, A. Dal Corso, S. de Gironcoli, P. Delugas, R.A. DiStasio, A. Ferretti, A. Floris, G. Fratesi, G. Fugallo, R. Gebauer, U. Gerstmann, F. Giustino, T. Gorni, J. Jia, M. Kawamura, H.Y. Ko, A. Kokalj, E. Küçükbenli, M. Lazzeri, M. Marsili, N. Marzari, F. Mauri, N.L. Nguyen, H.V. Nguyen, A. Otero-de-la-Roza, L. Paulatto, S. Poncé, D. Rocca, R. Sabatini, B. Santra, M. Schlipf, A.P. Seitsonen, A. Smogunov, I. Timrov, T. Thonhauser, P. Umari, N. Vast, X. Wu, S. Baroni, Advanced capabilities for materials modelling with Quantum ESPRESSO. *J. Phys. Condens. Matter,* **2017**, *29* (46), 465901.

37. J.P. Perdew, K. Burke, M. Ernzerhof, Generalized Gradient Approximation Made Simple. *Phys. Rev. Lett.,* **1996**, *77* (18), 3865-3868.

38. V. Barone, M. Casarin, D. Forrer, M. Pavone, M. Sambi, A. Vittadini, Role and effective treatment of dispersive forces in materials: Polyethylene and graphite crystals as test cases. *J Comput Chem,* **2009**, *30* (6), 934-939.

39. S. Grimme, Semiempirical GGA-type density functional constructed with a long-range dispersion correction. *J. Comput. Chem.,* **2006**, *27* (15), 1787-1799.

40. M. Salavati-Niasari, F. Davar, H.J.C.L. Emadi, Hierarchical nanostructured nickel sulfide architectures through simple hydrothermal method in the presence of thioglycolic acid. *Chalcogenide Lett,* **2010**, *7* (12), 647-655.

41. T. Tian, L. Huang, L. Ai, J. Jiang, Surface anion-rich NiS2 hollow microspheres derived from metal–organic frameworks as a robust electrocatalyst for the hydrogen evolution reaction. *J. Mater. Chem. A,* **2017**, *5* (39), 20985-20992.

42. M.S. Faber, M.A. Lukowski, Q. Ding, N.S. Kaiser, S. Jin, Earth-Abundant Metal

Pyrites (FeS_2, CoS_2, NiS_2, and Their Alloys) for Highly Efficient Hydrogen Evolution and Polysulfide Reduction Electrocatalysis. *J. Phys. Chem. C,* **2014**, *118* (37), 21347-21356.

43. J. Huang, H. Gao, Y. Xia, Y. Sun, J. Xiong, Y. Li, S. Cong, J. Guo, S. Du, G. Zou, Enhanced photoelectrochemical performance of defect-rich ReS_2 nanosheets in visible-light assisted hydrogen generation. *Nano Energy,* **2018**, *46*, 305-313.

44. M.-J. Park, J.-Y. Jung, Y.-H. Nam, J.-W. Song, C. Jeong, J.-H. Lee, Improved photoelectrochemical hydrogen evolution using a defect-passivated Al_2O_3 thin film on p-Si. *Thin Solid Films,* **2016**, *616*, 550-554.

45. Y. Yan, J. Lin, J. Cao, S. Guo, X. Zheng, J. Feng, J. Qi, Activating and optimizing the activity of NiCoP nanosheets for electrocatalytic alkaline water splitting through the V doping effect enhanced by P vacancies. *J. Mater. Chem. A,* **2019**, *7* (42), 24486-24492.

46. S. Li, P. Ge, F. Jiang, H. Shuai, W. Xu, Y. Jiang, Y. Zhang, J. Hu, H. Hou, X. Ji, The advance of nickel-cobalt-sulfide as ultra-fast/high sodium storage materials: The influences of morphology structure, phase evolution and interface property. *Energy Storage Mater.,* **2019**, *16*, 267-280.

47. R. Fan, J. Zhou, W. Xun, S. Cheng, S. Vanka, T. Cai, S. Ju, Z. Mi, M. Shen, Highly efficient and stable Si photocathode with hierarchical MoS_2/Ni_3S_2 catalyst for solar hydrogen production in alkaline media. *Nano Energy,* **2020**, *71*, 104631.

48. Q. Jia, C. Yu, W. Liu, G. Zheng, C. Lei, L. Lei, X. Zhang, High performance n^+p-$Si/Ti/NiS_xO_y$ photocathode for photoelectrochemical hydrogen evolution in alkaline solution. *J. Energy Chem.,* **2019**, *30*, 101-107.

49. J.R. McKone, E.L. Warren, M.J. Bierman, S.W. Boettcher, B.S. Brunschwig, N.S. Lewis, H.B. Gray, Evaluation of Pt, Ni, and Ni–Mo electrocatalysts for hydrogen evolution on crystalline Si electrodes. *Energy Environ. Sci.,* **2011**, *4* (9), 3573-3583.

50. Z. Huang, Z. Chen, Z. Chen, C. Lv, H. Meng, C. Zhang, Ni12P5 Nanoparticles as an Efficient Catalyst for Hydrogen Generation via Electrolysis and Photoelectrolysis. *ACS Nano,* **2014**, *8* (8), 8121-8129.

51. Y. Yang, M. Wang, P. Zhang, W. Wang, H. Han, L. Sun, Evident Enhancement of Photoelectrochemical Hydrogen Production by Electroless Deposition of M-B (M = Ni, Co) Catalysts on Silicon Nanowire Arrays. *ACS Appl. Mater. Interfaces,* **2016**, *8*

(44), 30143-30151.

52. H. Zhang, Q. Ding, D. He, H. Liu, W. Liu, Z. Li, B. Yang, X. Zhang, L. Lei, S. Jin, A p-Si/$NiCoSe_x$ core/shell nanopillar array photocathode for enhanced photoelectrochemical hydrogen production. *Energy Environ. Sci.,* **2016**, *9* (10), 3113-3119.

53. J. Feng, M. Gong, M.J. Kenney, J.Z. Wu, B. Zhang, Y. Li, H. Dai, Nickel-coated silicon photocathode for water splitting in alkaline electrolytes. *Nano Res.,* **2015**, *8* (5), 1577-1583.

54. Y. Hou, M. Qiu, G. Nam, M.G. Kim, T. Zhang, K. Liu, X. Zhuang, J. Cho, C. Yuan, X. Feng, Integrated Hierarchical Cobalt Sulfide/Nickel Selenide Hybrid Nanosheets as an Efficient Three-dimensional Electrode for Electrochemical and Photoelectrochemical Water Splitting. *Nano Lett.,* **2017**, *17* (7), 4202-4209.

55. I. Mondal, S.Y. Moon, H. Kim, J.Y. Park, Hydrogen production by water reduction on Si photocathode coupled with Ni_2P. *Int. J. Hydrogen Energy,* **2019**, *44* (14), 7241-7251.

56. H. Bae, V. Burungale, J.-B. Park, S. Wan Bang, H. Rho, S. Hyung Kang, S.-W. Ryu, J.-S. Ha, Pd-Ni nanoalloy decorated carbon nanotubes based efficient and stable silicon photocathode for acidic water splitting. *Appl. Surf. Sci.,* **2020**, *510*, 145389.

57. W. Zhou, F. Niu, S.S. Mao, S. Shen, Nickel complex engineered interface energetics for efficient photoelectrochemical hydrogen evolution over p-Si. *Appl. Catal. B Environ.,* **2018**, *220*, 362-366.

58. B. Klahr, S. Gimenez, F. Fabregat-Santiago, J. Bisquert, T.W. Hamann, Photoelectrochemical and Impedance Spectroscopic Investigation of Water Oxidation with “Co–Pi”-Coated Hematite Electrodes. *J. Am. Chem. Soc.,* **2012**, *134* (40), 16693-16700.

59. M. Li, Y. Zhu, H. Wang, C. Wang, N. Pinna, X. Lu, Ni Strongly Coupled with Mo2C Encapsulated in Nitrogen-Doped Carbon Nanofibers as Robust Bifunctional Catalyst for Overall Water Splitting. *Adv. Energy Mater.,* **2019**, *9* (10), 1803185.

Chapter 4 A Synergetic Strategy to Construct Anti-reflective and Anti-corrosive Co-P/WS_x/Si Photocathode for Durable Hydrogen Evolution in Alkaline Condition

4.1 Introduction

Photoelectrochemical (PEC) water splitting is a promising method to convert solar energy into renewable hydrogen fuel. It involves two half-reactions of hydrogen evolution (HER) at the photocathode and oxygen evolution (OER) at the photoanode, which are generally carried out in highly acidic and alkaline solutions, respectively. As the OER shows more sluggish kinetics to require higher overpotential in acid solutions than HER in an unseparated compartment, conducting HER in alkaline solutions will be preferable with OER.[1-4]

While alkaline solutions result in severe corrosion on Si, the most widely studied photocathode in acidic electrolytes for PEC HER,[5-8] a protection layer is usually utilized to separate the Si photocathode from alkaline solutions. For instance, TiO_2 has proven to be a good protection layer for Si photocathodes via atomic layer deposition.[9, 10] However, these Si photocathodes with dense TiO_2 protection layers need to be combined with precious metal cocatalysts to counter the limitation of light transmission.[9-12] Therefore, designing the appropriate thickness of the protection layer is critical to achieving good alkali resistance, facile electron transfer, and efficient light transmittance to Si. Transition metal chalcogenide such as WS_2 and MoS_2 is one of the potential alternatives, benefiting from their ability in atomic layer fabrication and high stability in acid or alkaline solutions.[13-15] Notably, most of the fabrication processes show the complexity and are not cost-effective.

On the other hand, decorating effective cocatalysts with less light-blocking is also significant to PEC HER in alkaline solutions. Recently, non-noble metal Co-P cocatalysts have attracted significant attention due to their remarkable catalytic properties along with outstanding stability in alkaline HER.[16-19] Specific examples are CoP[18, 20-25], Co_2P[26, 27], Co-P alloys[28], and their derivatives[29-31]. There are also numerous reports on the application of Co-P cocatalysts in PEC HER, but most are under acidic conditions.[22-27] In the mentioned regard, it is highly desirable to fabricate Co-P cocatalysts on Si

photocathodes used in alkaline solutions. However, a similar concern on the thickness of the protection layer also raises to the Co-P cocatalyst due to their intrinsic light-blocking. Thus, less thickness of Co-P cocatalyst with high efficiency for PEC HER is demand for Si photocathodes. Loading the thin-film Co-P cocatalyst via the electrodeposition is a promising method since its morphology and thickness can be modulated by controlling the electrochemical potential or current and affected by the photocathode interphase, including the protection layer.[22, 32]

Herein, a WS_x-protected planar p-Si photocathode with anti-reflective Co-P film cocatalyst (denoted as Co-P/WS_x/Si) is designed and proposed for efficient and durable PEC HER in the alkaline electrolyte (1.0 M KOH). This strategy introduces the self-assembled WS_x thin film on the Si surface as a uniform protection layer with moderate charge-transfer conductivity. Meanwhile, the controllable WS_x serve as nucleation sites to modulate and obtain anti-reflective Co-P cocatalyst by photo-assist electrodeposition, forming a robust and complementary architecture. This synergetic integration of Co-P/WS_x/Si photocathode exhibits outstanding PEC HER performances, including an onset potential of 0.47 V_{RHE} and a high photocurrent density of −25.1 mA cm^{-2} at 0 V_{RHE} under an AM 1.5 G simulated solar illumination. More surprisingly, the Co-P/WS_x/Si photocathode shows superior durability of 300 h at 0 V_{RHE} without visible degradation. This systematic work may pave a new path for planar Si-based PEC-HER applications in alkaline media.

4.2 Experiment section

4.2.1 Materials preparation.

Preparation of H-terminated p-Si, 5WS_x/Si, 20WS_x/Si, and 30WS_x/Si substrates: The pretreatment of boron-doped Si wafers (p-Si: 0.5 mm thickness, 1–10 ohm cm^{-1} resistivity) were adapted from previous literature.[13] The planar p-Si wafers were immersed in H_2O_2: H_2SO_4 (1:2,) solution at 60 ºC for 30 min and washed by deionized water (DW), then etched in 0.5% HF at room temperature for 5 min and washed by DW, and then etched in HCl: H_2O_2: H_2O (1:1:4) solution at 60 ºC for 25 min and washed by DW. After that, the H-terminated p-Si substrates were obtained through immersed in a 40% NH_4F solution for 5 min and washed by DW. Subsequently, 5WS_x/Si, 20WS_x/Si, and 30WS_x/Si substrates were prepared by immersed in 5/20/30 mM $(NH_4)_2WS_4$-containing 5% HF aqueous solutions for 5 min respectively, then washed by DW and

dried at 70 ºC for over 2 hours under vacuum.

Fabrication of Co-P/Si, Co-P/5WS_x/Si, Co-P/20WS_x/Si, and Co-P/30WS_x/Si photocathodes: The photo-assisted electrodeposition of Co-P catalysts on H-terminated p-Si, 5WS_x/Si, 20WS_x/Si, and 30WS_x/Si substrates were conducted in a standard three-electrode cell system at AM 1.5 G solar simulation (30 mW cm^{-2}). The preparation of working electrodes was that the backside of as-prepared substrates was coated with the eutectic gallium-indium alloy, then attached to a Cu plate and sealed. Such photocathodes have an area of 0.4 cm^2. The counter and reference electrodes were a graphite rod and a Hg/HgO (1M NaOH) electrode, respectively. The deposition electrolyte contained 80 mM $CoCl_2 \cdot 6H_2O$, 0.5 M $NaPH_2O_2 \cdot H_2O$, and 0.2 M KCl solution. The Co-P catalysts were obtained by linear voltammetry sweep from 0 to -0.5 V vs. Hg/HgO (1.0 M NaOH) for 5 cycles.

4.2.2 Material characterization

X-ray film diffraction and X-ray photoelectron spectroscopy (XPS, VG-ESCA Mark II) with monochromatized Al Kα radiation were used to determine the crystal structures and surface valence states. Atomic force microscopy (AFM, Nano Navi II), scanning electron microscopy (SEM, JSM-6701F), and transmission electron microscope (TEM, JEM-2100F) were applied to analyze the morphologies of as-obtained samples. Ultraviolet-visible (UV-vis) absorption spectra were measured utilizing a spectrophotometer (UV-2600, Shimadzu, Japan). The charge carrier transfer and separation of target samples were investigated by photoluminescence (PL) emission (FP-6500).

The calculation of P content in Co-P film cocatalyst: According to the relative peak area of Co 2p (Area $_{Co\ 2p}$ = 8180) and P 2p (Area $_{P\ 2p}$ = 268) and their corresponding Relative Sensitivity Factors (RSF, RSF $_{Co\ 2p}$ = 3.5 and RSF $_{P\ 2p}$ = 0.4), the detailed calculation of the atomic ratio of Co 2p to P 2p within the Co-P cocatalyst is shown as following:

$$n_{Co\ 2p} / n_{P\ 2p} = (Area_{Co\ 2p} / ASF_{Co\ 2p}) / (Area_{P\ 2p} / ASF_{P\ 2p})$$

Hence, the P content in Co-P cocatalyst calculated is ~22%.

4.2.3 Photoelectrochemical measurement

The PEC measurements were carried out on an electrochemical workstation (ALS/CH

model 660D) using a three-electrode cell system in 1.0 M KOH at AM 1.5 G solar simulation (100 mW cm^{-2}), which contained a graphite rod as the counter electrode and a Hg/HgO (1.0 M NaOH) electrode as the reference electrode. The exposure area of the photocathode is 0.4 cm^2. Linear sweep voltammograms (LSV) were obtained. Mott–Schottky curves were performed from –0.4 to +0.6 V_{RHE} at 1000 Hz. The onset potential (V_{on}) is defined as the potential that derives a photocurrent density of −0.1 mA cm^{-2}. Electrochemical impedance spectroscopy (EIS) tests were obtained at various conditions (0.01–100 000 Hz). All the potentials could be transformed to the RHE using the equation: $E_{RHE} = E – IR + 0.059\times pH + E_{Hg/HgO}$, where E is the experimental potential, $E_{Hg/HgO}$ is equal to +0.12 V_{RHE}, the pH of 1.0 M KOH is measured to be around 13.6, I and R are the photocurrent density (mA cm^{-2}) and the internal resistance (Ω) of electrolyte contact, respectively. The experiment of H_2 evolution was carried out in a completely sealed quartz reactor. The electrode with an area of 0.4 cm^2 was immersed in the electrolyte in a three-electrode configuration. Prior to the reaction and sealing processes, the electrolyte was purged with argon gas. The generated H_2 was analyzed with a thermal conductivity detector (TCD) gas chromatograph (Shimadzu GC-8AIT, argon carrier). Similarly, AM 1.5 G solar simulation (100 mW cm^{-2}) was utilized as the light sources.

4.3 Results and discussion

4.3.1 Synthesis and characterization of WS_x protective layers

The self-assembly procedure of thin-film WS_x as a protective layer on hydrogen-terminated p-Si is schematically illustrated in **Figure 4.1**a. Specifically, the thin-film WS_x is obtained through H-terminated p-Si immersed in WS_4^{2-}-containing HF aqueous solutions, which is adapted from our previous study.[13] As shown in atomic force microscopy (AFM) images, the bare H-terminated p-Si has an atomically smooth surface with Root Mean Square (RMS) roughness of 0.18 nm (Figure 4.1b). After the H-terminated p-Si immersed in HF aqueous solutions with increasing concentrations of WS_4^{2-}, the average thicknesses of WS_x thin-film increased to approximately 3 nm (Figure 4.1c–e). The thin-film WS_x is not dense and even enough on p-Si using the 5 mM WS_4^{2-} reactant ($5WS_x$/Si, RMS roughness = 0.85 nm), while its uniformity is significantly improved when the WS_4^{2-} concentration increases to 20 mM ($20WS_x$/Si, RMS roughness = 0.59 nm). Increasing the concentration to 30 mM ($30WS_x$/Si, RMS roughness = 0.89 nm) results in excessive growth of WS_x nanoparticles. These preliminary results show

that a moderate 20 mM WS_4^{2-} reactant could ensure a uniform WSx protective layer formation.

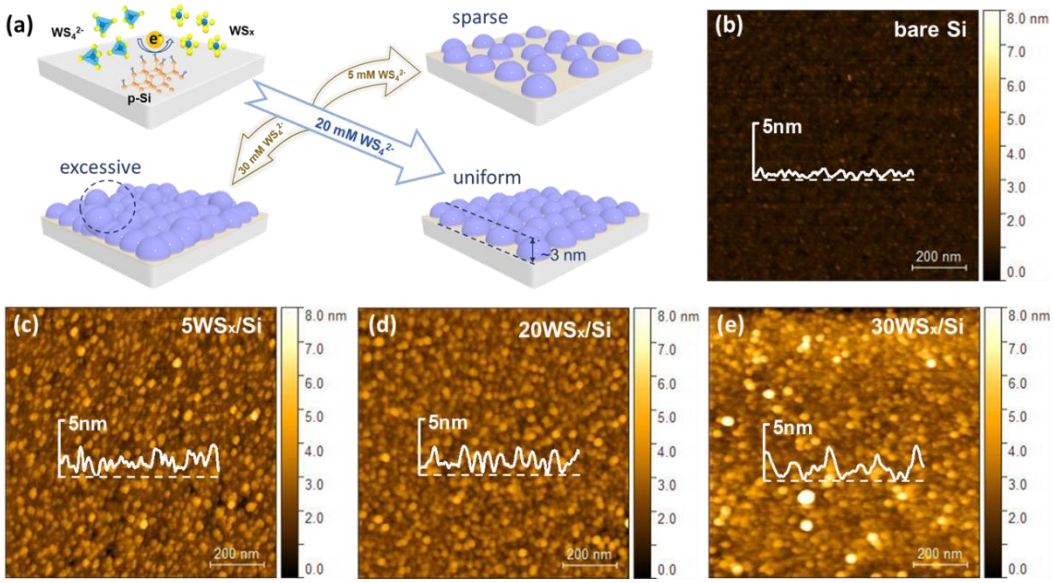

Figure 4.1 (a) Schematic illustration for self-assembled deposition of WS_x on p-Si. AFM images of (b) bare Si, (c) $5WS_x$/Si, (d) $20WS_x$/Si, and (e) $30WS_x$/Si. The height profiles along the corresponding dashed lines are shown as the inset Figures.

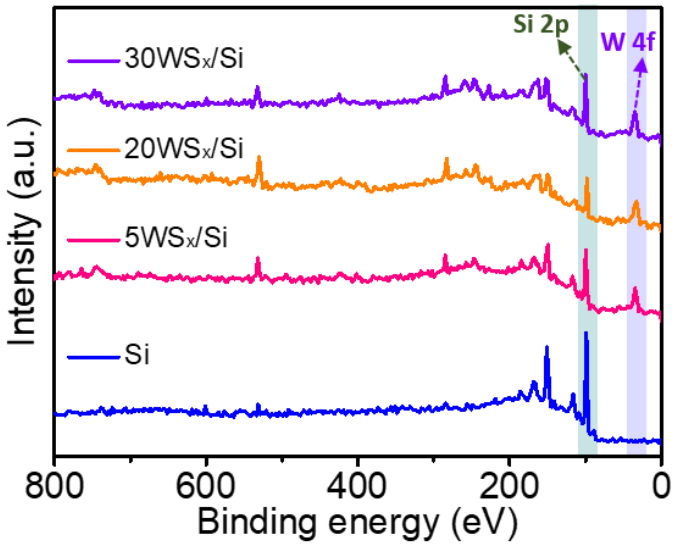

Figure 4.2 The survey spectra of bare Si, $5WS_x$/Si, $20WS_x$/Si, and $30WS_x$/Si.

X-ray photoelectron spectroscopy (XPS) is applied to determine the valence states and chemical composition of WS_x/Si photocathodes. The survey spectra (**Figure 4.2**) confirm the W, S, O, and Si elements. Compared with the bare Si, the W 4f peaks in $5WS_x$/Si, $20WS_x$/Si, and $30WS_x$/Si samples are displayed, proving the successful deposition of WS_x in precursor solutions with different concentrations of WS^{4-}. At the same time, the

intensities of the Si peaks in three WS_x/Si samples have weakened significantly, which is caused by the coverage of WS_x on the Si surface. In **Figure 4.3**a for the high-resolution S 2p spectra, two peaks at 151.1 and 168.3 eV correspond to Si 2s and Si 2s plasmon are observed.[33] Additional peaks appear at around 163 eV, assigned to S 2p. It can be deconvolved into two doublets of S $2p_{3/2}$ and S $2p_{1/2}$. To be specific, the lower binding energy doublets at 162.3 eV (S $2p_{3/2}$) and 163.0 eV (S $2p_{1/2}$) are attributed to the S element of the 2H phase, and the higher binding energy doublets at 163.4 eV (S $2p_{3/2}$) and 164.4 eV (S $2p_{1/2}$) could be assigned to disordered S atoms in the unsaturated S^{2-} in WS_x. Among the studied WS_x/Si, 20WS_x/Si shows a much higher intensity of S 2p peaks than 5WS_x/Si. While when the WS_4^{2-} concentration continues to increase to 30 mM, no noticeable intensity change is observed. In Figure 4.3b for W 4f spectra, the dominant peaks at 33.2 and 35.5 eV are assigned to W $4f_{7/2}$ and W $4f_{5/2}$, respectively. An additional peak of approximately 38.5 eV is assigned to high valence states of W^{VI}, indicating the partially oxidized WS_x due to the air exposure of its surface and uncomplete reduction reaction of WS_4^{2-}.[34] The intensity change of W 4f shows a similar tendency as that of S 2p peaks when the WS_4^{2-} concentration increases.

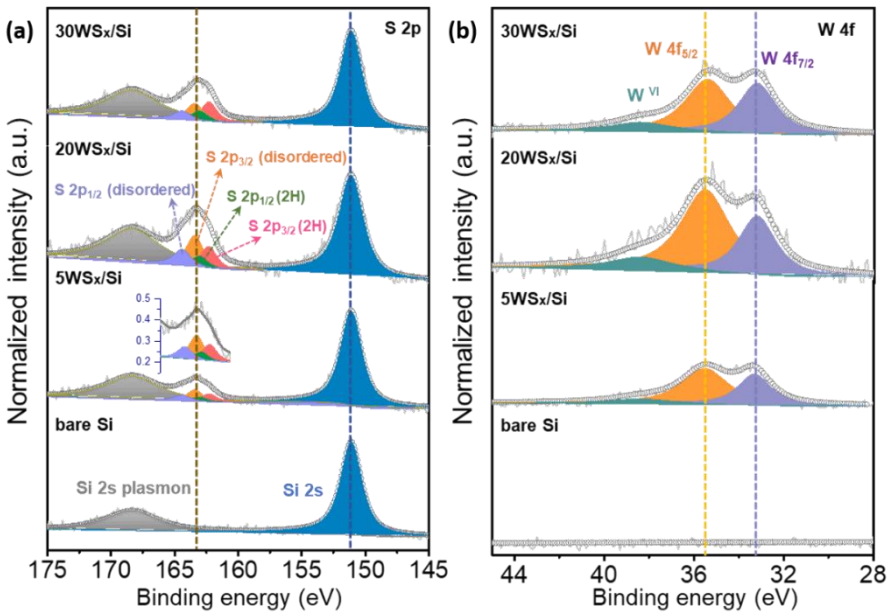

Figure 4.3 High-resolution XPS spectra of (a) S 2p and (b) W 4f for bare Si, 5WS_x/Si, 20WS_x/Si, and 30WS_x/Si. All the spectra are normalized by the intensity of Si 2s as the reference.

Combining the AFM and XPS analyses, it is proved that the thin-film WS_x reaches a saturated and uniform morphology from 20 mM WS_4^{2-} solution onward. That of lower

than 20 mM will make the thin-film WS_x uneven on the Si surface, which might show an insufficient protective role in alkaline solutions. To confirm the protective role of the thin-film WS_x for Si in alkaline solutions, the as-prepared WS_x/Si wafers were soaked in 1.0 M KOH solution for 12 h. Compared with the scanning electron microscopy (SEM) image of the smooth surface of original bare Si (**Figure 4.4**), the SEM image in **Figure 4.5**a shows that the bare Si surface is severely etched with deep pits larger than 1.0 μm^2 after immersing in 1.0 M KOH solution. The etched pits are significantly reduced in WS_x/Si (Figure 4.5b–d), among which $20WS_x$/Si and $30WS_x$/Si already exhibit outstanding alkalic resistance with few slight scratches.

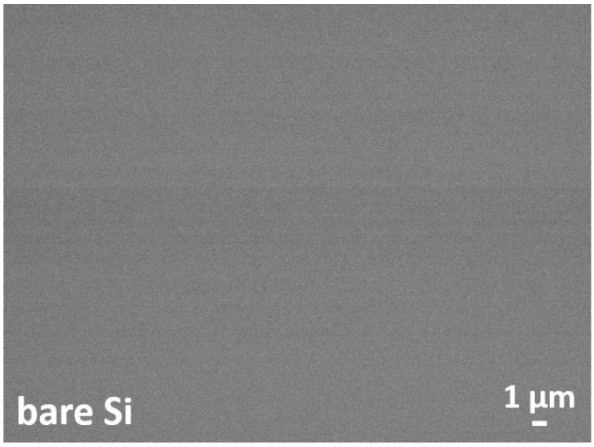

Figure 4.4 SEM images of bare Si wafers before immersing in 1.0 M KOH solution.

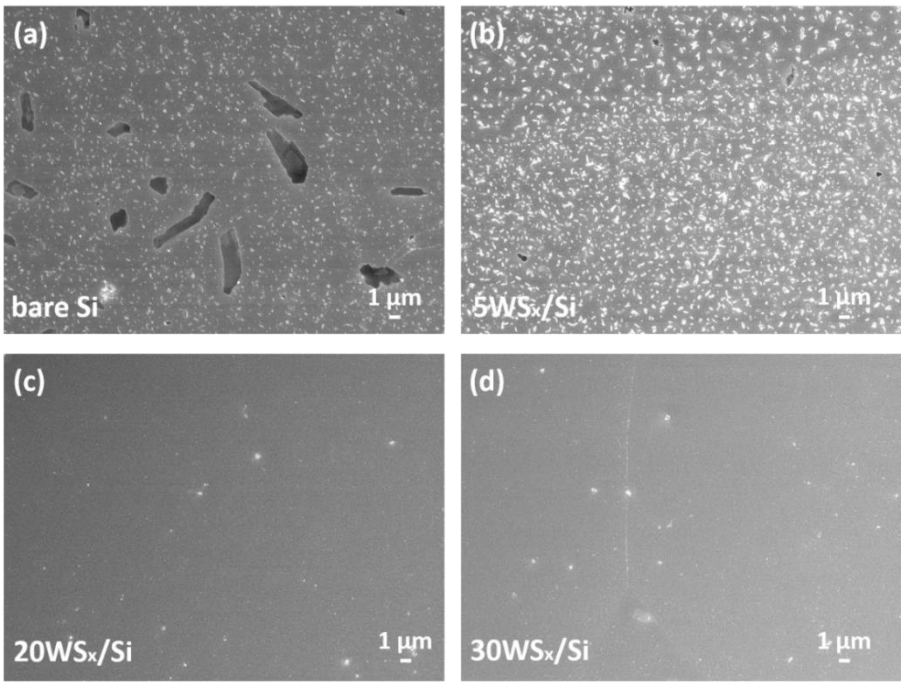

Figure 4.5 SEM images of (a) bare Si, (b) $5WS_x$/Si, (c) $20WS_x$/Si, and (d) $30WS_x$/Si wafers soaked in 1.0 M KOH solution for 12 hours.

4.3.2 Characterization of Co-P/WS_x/Si photocathodes

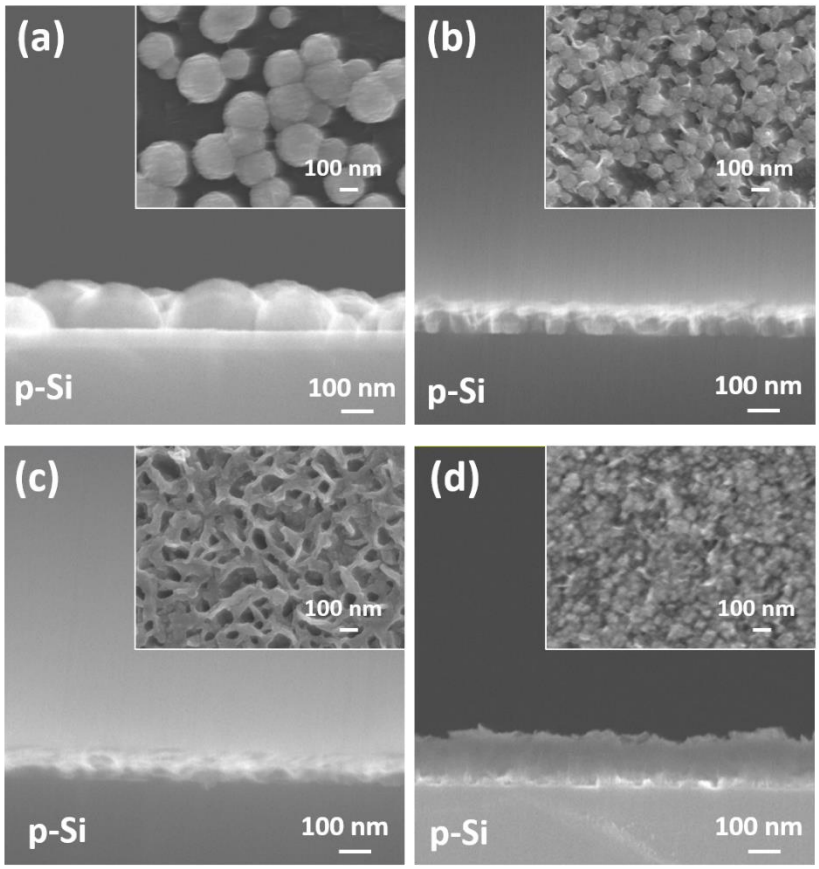

Figure 4.6 SEM images of (a) Co-P/Si, (b) Co-P/5WS_x/Si, (c) Co-P/20WS_x/Si, and (d) Co-P/30WS_x/Si.

The Co-P cocatalysts were then deposited on WS_x/Si via photo-assisted electrodeposition. Without thin-film WS_x on Si, the morphology of Co-P cocatalyst on Si (Co-P/Si) presents dispersed particles with a diameter of approximately 200 nm (**Figure 4.6**a). A large area of Si surface is exposed between the Co-P particles in Co-P/Si (the inset of Figure 2a). While with thin-film WS_x on Si, the morphology and size of Co-P cocatalysts change accordingly. The Co-P particles (Figure 4.6b) deposited on the 5WS_x/Si (Co-P/5WS_x/Si) have smaller sizes and a more compact distribution than the Co-P/Si. In Co-P/20WS_x/Si (Figure 4.6c), a Co-P film about 50 nm thick is formed, evenly covering the photocathode surface. It is worth noting that, in the inset of Figure 4.6c, the porous Co-P surface can provide a large specific surface area and more active sites, which is conducive to full contact with the electrolyte during the PEC-HER process. However, the Co-P film in Co-P/30WS_x/Si becomes much thicker and denser than the other two Co-P/WS_x/Si (Figure 4.6d). Such a thick Co-P cocatalyst layer is likely to block the light

absorption of Si semiconductors. Through the above analysis, along with AFM and SEM observations, it is found that the thin-film WS_x in Co-P/20WS_x/Si could be not only efficient in protecting Si from alkaline solution but also a suitable nucleation base to obtain uniform Co-P film with moderate thickness.

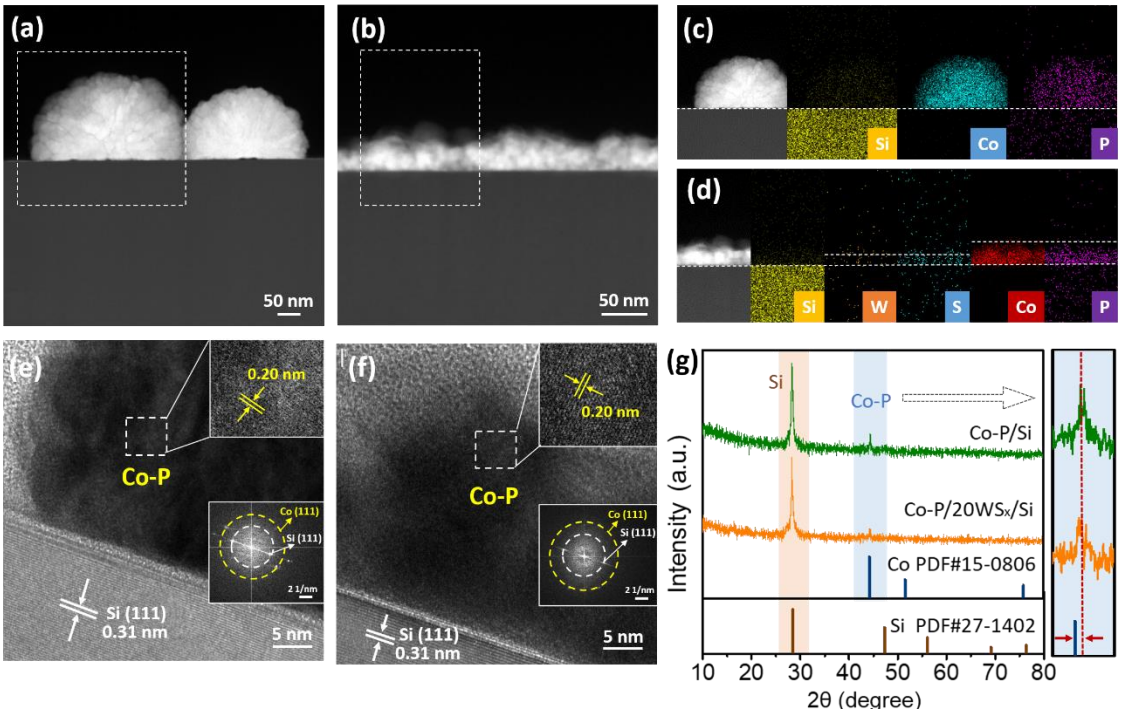

Figure 4.7 (a, b) HAADF-STEM images, (c, d) EDS mapping images, (e, f) HR-TEM images, and the corresponding SAED images inset of Co-P/Si and Co-P/20WS_x/Si, respectively. (g) The thin-film XRD patterns of Co-P/Si and Co-P/20WS_x/Si.

The high-angle annular dark-field scanning transmission electron microscopy (HAADF-STEM) images in **Figure 4.7**a and Figure 4.7b further confirm the difference in the morphologies of Co-P cocatalysts within Co-P/Si and Co-P/20WS_x/Si, respectively. The energy-dispersive spectroscopy (EDS) mapping was carried out to analyze the element distribution therein. The elements of Co, P, and Si in Co-P/Si (Figure 4.7c) are uniformly distributed, corresponding to a bilayer structure of cocatalyst/semiconductor. For Co-P/20WS_x/Si, in addition to the uniform distribution of Co, P, and Si elements, the W and S elements in WS_x present between Co-P and Si, forming a trilayer structure of cocatalyst/protector/semiconductor (Figure 4.7d). Therefore, it is confirmed that the WS_x thin film has an impact on the subsequent Co-P deposition. The unsaturated S in the thin-film WS_x is considered to have an attractive force to concentrate the Co^{2+} ions near the interphase in the electrodepositing solutions. Thus, it leads to more Co-P nuclei formation,

finally resulting in uniform Co-P cocatalysts with smaller sizes in Co-P/20WS_x/Si.

Table 4.1 The atomic ratio of P and Co elements in the EDS result of Co-P/20WS_x/Si regardless of C and O elements.

Element	Atomic %
P K	14.94
Co K	85.06

X-ray diffraction (XRD) is conducted to analyze the compositions of Co-P cocatalysts within Co-P/20WS_x/Si and Co-P/Si, as shown in Figure 4.7g. The characteristic peak at 28.4° is indexed to the (111) facet of Si (JCPDS NO. 27-1402), and the peak of Co-P shifts to a slightly higher angle at 44.4° compared with the (111) facet of Co at 44.2° (JCPDS NO. 15-0806), as shown in the enlarged image of Figure 4.7g. This phenomenon is in good accordance with previous literature about Co-P alloy made by electrodeposition method [35-37], because the relatively low content of P with smaller atomic radius in as-deposited Co-P has such an effect on Co. The P content in Co-P cocatalyst is estimated to be about 22% from the relative XPS peak area and corresponding Relative Sensitivity Factors (The detailed calculation steps in the Experimental Section), which almost corresponds to the atomic ratio in the EDS result (**Table 4.1**). The high-resolution transmission electron microscopy (HR-TEM) images of Co-P/Si and Co-P/20WS_x/Si are further shown in Figure 4.7e and Figure 4.7f, respectively. The interplanar space of 0.31 nm corresponds to the (111) direction of Si, and the d-space of 0.20 nm about as-deposited Co-P is associated with the (111) direction of Co, which is obtained by measuring the average of 10 layers. The selected area electron diffraction (SAED) patterns (the inset of Figures 4.7e, f) also reveal the corresponding diffraction rings from the inner of Si to the outer of Co. The d-space value of Co-P is a little bit smaller than that of standard Co (111), which is consistent with the influence of a small amount of P on Co-P alloy in the above XRD analysis.

4.3.3 PEC-HER performances and mechanism analysis

The PEC-HER performances of bare Si, 20WS_x/Si, Co-P/Si, Co-P/5WS_x/Si, Co-P/20WS_x/Si, and Co-P/30WS_x/Si photocathodes were evaluated in 1.0 M KOH solution at a scan rate of 50 mV/s for comparison. Notably, the linear sweep voltammetry (LSV) curves show that the currents for all photocathodes under dark are negligible (dashed line in **Figure 4.8**a). Under light irradiation, the bare Si photocathode shows an onset potential

of approximately −0.04 V_{RHE} in Figure 3a. Compared with the bare Si, Co-P/Si and Co-P/WS_x/Si photocathodes exhibit positive shifts on the onset potential. Significantly, the Co-P/20WS_x/Si exhibits the optimal onset potential at +0.47 V_{RHE} among the Co-P/WS_x/Si photocathodes, as summarized in Figure 4.8b. It confirms that the Co-P cocatalysts integrating with WS_x can further improve the PEC-HER activity under the alkaline condition, compared with only Co-P cocatalyst. The significantly enhanced PEC-HER performance of Co-P/20WS_x/Si photocathode in the alkaline solution is comparable to the reported Si-based photocathodes (**Table 4.2**). It must be noted that the combination of planar Si and non-noble metal cocatalysts in this study is cost-effective. Mott-Schottky measurements were employed to examine why the integration of Co-P cocatalyst with thin-film WS_x can significantly improve the PEC-HER performance. As shown in **Figure 4.9**, the flat-band potential (the intersection of tangent and x-axis) of the Co-P/20WS_x/Si (+0.25 V_{RHE}) is higher than those of the Co-P/Si (+0.02 V_{RHE}), 20WS_x/Si (−0.14 V_{RHE}), and bare Si (−0.27 V_{RHE}), which corresponds precisely to the positive shifting trend of their onset potentials as analyzed above.

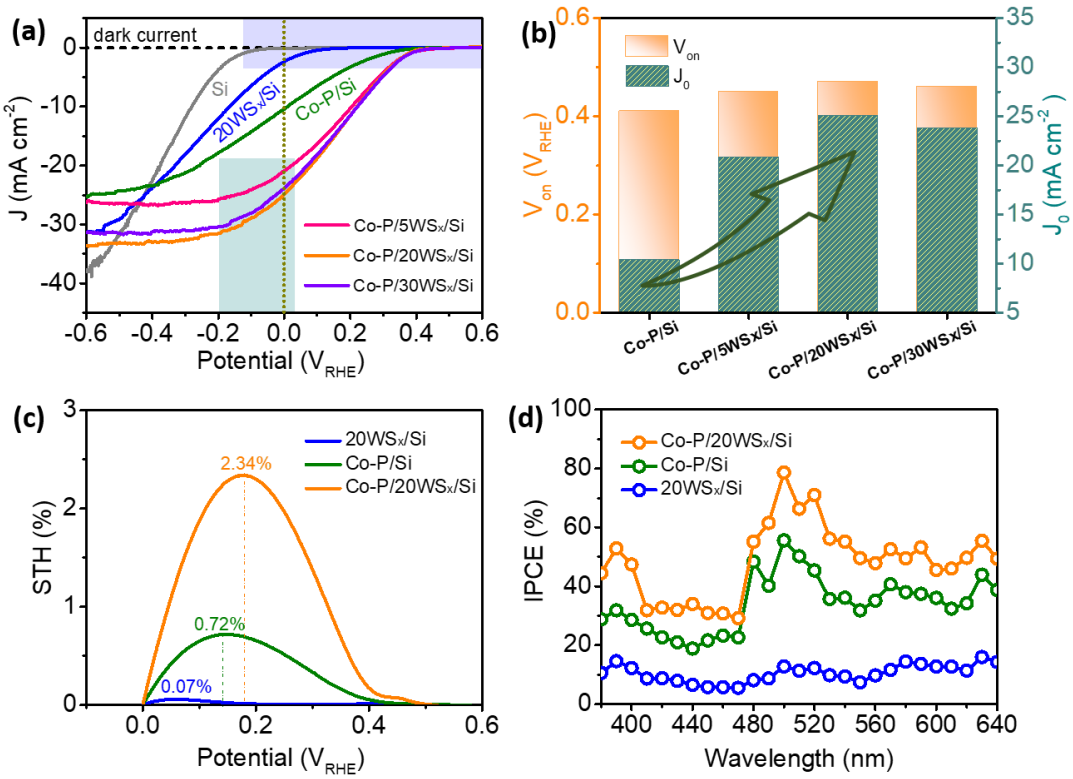

Figure 4.8 (a) LSV curves under light, (b) comparison of onset potentials (V_{on}) and photocurrent densities at 0 V_{RHE} (J_0) of bare Si, 20WS_x/Si, Co-P/Si, Co-P/5WS_x/Si, Co-P/20WS_x/Si, and Co-P/30WS_x/Si, (c) half-cell STH efficiency, and (d) IPCE of 20WS_x/Si, Co-P/Si, and Co-P/20WS_x/Si photocathodes.

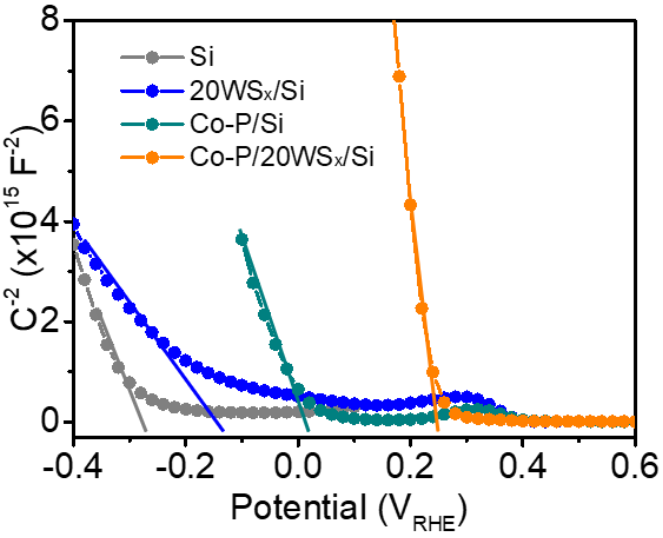

Figure 4.9 Mott-Schottky plots under dark of bare Si, $20WS_x$/Si, Co-P/Si, and Co-P/$20WS_x$/Si.

Table 4.2 Summary of Si-based photocathodes for HER in alkaline media.

Photocathodes	**Deposition method**	**J_{0V} [a] ($mA\ cm^{-2}$)**	**V_{on} [b] (V_{RHE})**	**Stability (h)**	**Electrolyte**	**Light ($mW\ cm^{-2}$)**	**Ref.**
MoS_2/Ni_3S_2/Ni/Si	sputtering/electro deposition	-41.45	0.54	172	1 M KOH	100	2
Ni-Mo/Ni/n^+np^+-Si	spin coating/e-beam /electrodeposition	-36.3	0.50	100	1 M KOH	100	38
Ni-Mo/NiSi/n^+p-Si microwires	electrodeposition	-29.8	0.55	288	1 M KOH	100	1
Pd/b2-TiO_2/b-Si	sputtering	-35.3	0.32	100	1 M KOH	100	10
NiO_x/SiO_2/p-Si	thermal oxidation /e-beam/sputtering	-31	~0.8	1	1 M KOH	100	39
NiFe LDH/Ti/p-Si	hydrothermal/e-beam	-7	~0.3	24	1 M KOH	100	40
Ir/TiO_2/F:SnO_2/Ti /n^+p-Si	spray pyrolysis/e-beam	-35	0.5	5	0.1 M KOH	100	9
Ni/Ti/p-Si	e-beam	-20	~0.3	12	1 M KOH	225	41
Ni-rich NiO_x/Si	sputtering	-20	~0.55	10 (10mA/cm^2)	1 M KOH	100	42
Pt/TiO_2/n^+p Si	sputtering	-15	~0.5	24	1 M KOH	38.6	43
Co-P/$20WS_x$/Si	**self-assembly/ photo-assisted electrodeposition**	**-25.1**	**0.47**	**300**	**1 M KOH**	**100**	**This work**

[a] j_{0V} is the current density at an applied bias of 0 V vs. RHE; [b] V_{op} is the onset potential.

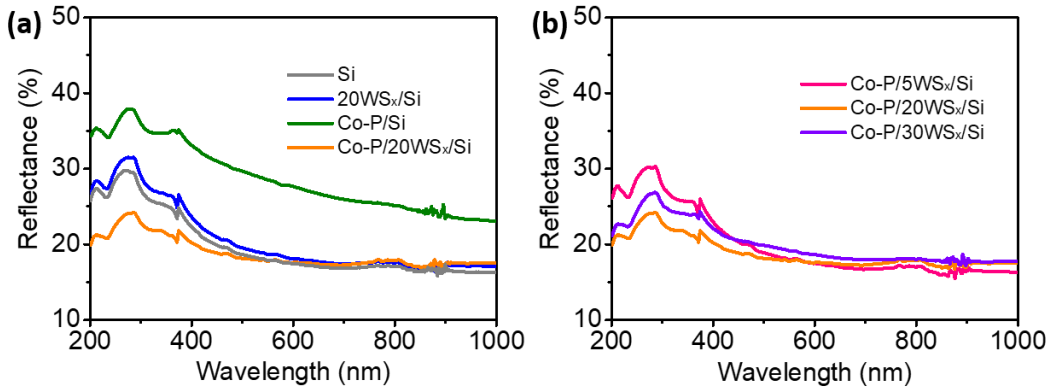

Figure 4.10 UV-vis spectra of (a) bare Si, $20WS_x$/Si, Co-P/Si, and Co-P/$20WS_x$/Si and (b) Co-P/$5WS_x$/Si, Co-P/$20WS_x$/Si, and Co-P/$30WS_x$/Si.

Moreover, the photocurrent densities at 0 V_{RHE} of the studied Co-P/Si and Co-P/WS_x/Si photocathodes are also visually compared in Figure 4.8b. The Co-P/Si photocathode without a WS_x protective layer has a much lower photocurrent density (−10.4 mA cm^{-2}) at 0 V_{RHE} than those of all Co-P/WS_x/Si photocathodes. By contrast, Co-P/$20WS_x$/Si processes the highest photocurrent density of −25.1 mA cm^{-2} at 0 V_{RHE}, followed by Co-P/$30WS_x$/Si with −23.8 mA cm^{-2}, and Co-P/$5WS_x$/Si with −20.8 mA cm^{-2}. Note that the saturated photocurrent densities of as-prepared photocathodes are affected by their optical behaviors. Therefore, **Figure 4.10**a compares the UV-vis reflection spectra of bare Si, $20WS_x$/Si, Co-P/Si, and Co-P/$5WS_x$/Si. The $20WS_x$/Si presents only slightly higher reflectance than that of bare Si, which indicates the uniform WS_x thin film prepared from 20 mM WS_4^{2-} has a little optical impact on the light absorption of the Si semiconductor. However, the light reflectance of Co-P/Si is higher than that of bare Si, resulting in a lower saturation photocurrent density (the photocurrent at −0.6 V_{RHE}), which confirms the light-blocking properties of large-size Co-P particles. Actually, the high light reflection of Co-P/Si is the predictable result, well matching with the large gap between the Co-P particles in the above SEM image (Figure 4.6a) and visible reflected color observed in the optical picture of Co-P/Si, but none in other Co-P/WS_x/Si samples (**Figure 4.11**). Notably, the optical reflectance result of Co-P/$20WS_x$/Si in the low-wavelength region is obviously lower than that of bare Si. This result suggests that the Co-P film acts as an anti-reflective cocatalyst in the Co-P/$20WS_x$/Si photocathode, which may be due to the porous structure of the Co-P film affecting the refractive index, as previously reported.[40] The light reflection spectra of three Co-P/WS_x/Si are further displayed in Figure 4.10b. The Co-P/$20WS_x$/Si gives the lowest reflectance in the low-

wavelength region than those of Co-P/5WS$_x$/Si and Co-P/30WS$_x$/Si, probably because both granular Co-P cocatalyst within Co-P/5WS$_x$/Si and thicker Co-P cocatalyst within Co-P/30WS$_x$/Si will hinder light penetration to the underneath Si semiconductor. Such a result reveals that the WS$_x$ thin film has a regulating effect on the morphology and thickness of subsequently deposited Co-P cocatalyst, and ultimately affects the light utilization efficiency of Si-based photocathodes.

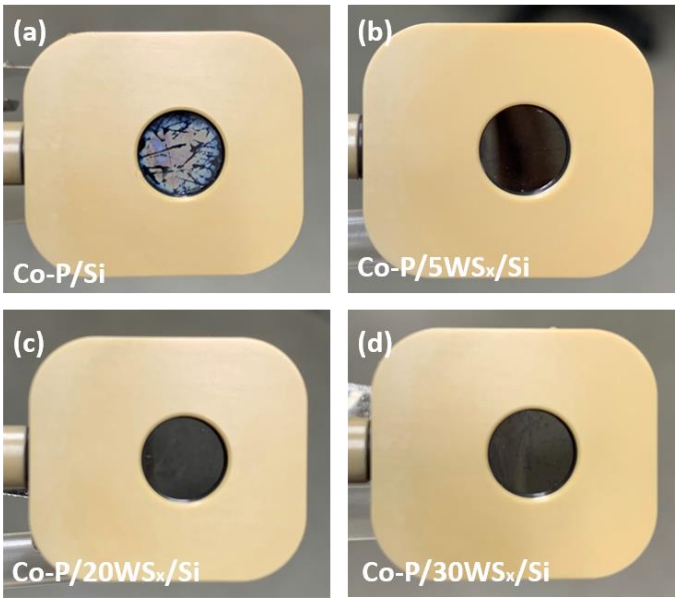

Figure 4.11 The optical pictures of (a) Co-P/Si, (b) Co-P/5WS$_x$/Si, (c) Co-P/20WS$_x$/Si, and (d) Co-P/30WS$_x$/Si.

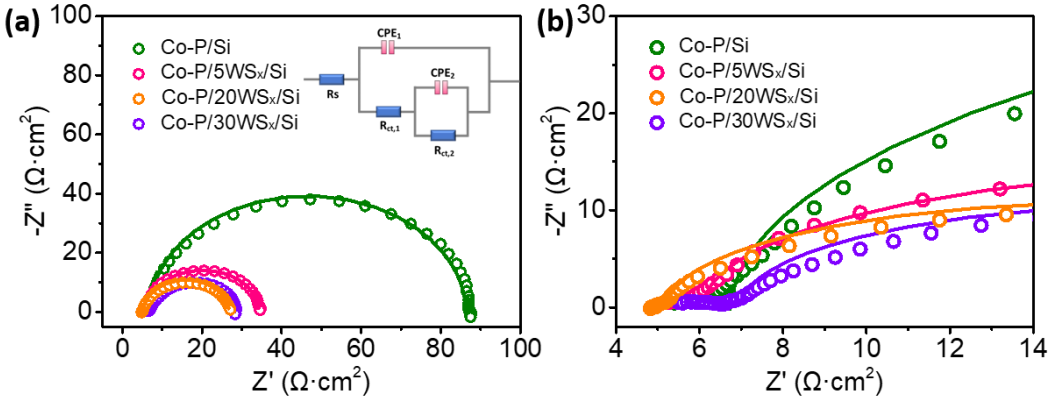

Figure 4.12 (a) Nyquist plots and fitting figures (solid lines) of Co-P/Si, Co-P/5WS$_x$/Si, Co-P/20WS$_x$/Si, and Co-P/30WS$_x$/Si and (b) the corresponding enlarged image.

As shown in Figure 4.8c, the optimum half-cell solar-to-hydrogen (STH) efficiency of 2.34% was obtained at 0.18 V$_{RHE}$ by Co-P/20WS$_x$/Si, followed by Co-P/Si with 0.72% at 0.14 V$_{RHE}$, and 20WS$_x$/Si with 0.07% at 0.05 V$_{RHE}$. Besides, the increased values of STH

efficiency by as-prepared photocathodes are consistent with their positive shifts in onset potentials, which implies the facilitated charge transfer in Co-P/20WS_x/Si photocathode. Furthermore, a noteworthy enhancement of incident photon-to-current efficiency (IPCE) was observed on the Co-P/20WS_x/Si over the wavelength range of 380−640 nm, with a maximum IPCE value of 78.6% at 500 nm (Figure 4.8d). Such high IPCE of Co-P/20WS_x/Si can be explained by the good light utilization efficiency.

Table 4.3 The charge-transfer resistance values of Co-P/Si, Co-P /5WS_x/Si, Co-P /20WS_x/Si, and Co-P /30WS_x/Si photocathodes.

Photocathodes	**R_S ($\Omega \cdot cm^2$)**	**$R_{ct,1}$ ($\Omega \cdot cm^2$)**	**$R_{ct,2}$ ($\Omega \cdot cm^2$)**
Co-P/Si	5.26	1.54	79.55
Co-P/5WS_x/Si	4.64	1.47	28.21
Co-P/20WS_x/Si	4.94	1.47	20.39
Co-P/30WS_x/Si	5.67	1.46	23.15

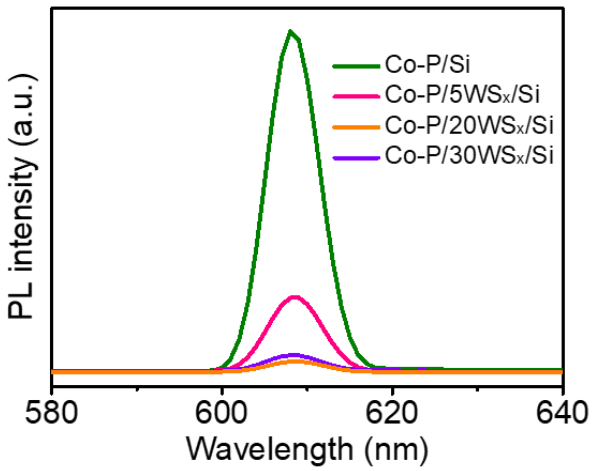

Figure 4.13 PL spectra with an excitation wavelength of 405 nm of Co-P/Si, Co-P/5WS_x/Si, Co-P/20WS_x/Si, and Co-P/30WS_x/Si.

The electrochemical impedance spectroscopy (EIS) and photoluminescence (PL) emission are potent tools to evaluate the behavior of charge carrier transfer and separation in Si semiconductors. The EIS measurements of three Co-P/WS_x/Si and Co-P/Si photocathodes were carried out at +0.40 V_{RHE} under illumination to evaluate the interfacial charge-transfer resistance, as shown in **Figure 4.12**. Nyquist plots of these photocathodes could be fitted into two semicircles using an equivalent circuit model (inset of Figure 4.12a), and the fitting results are presented with solid lines. The equivalent

circuit contains a series of resistances (R_s), two constant phase elements consisting of capacitances of the Si substrate (CPE_1) and cocatalyst (CPE_2), and two charge-transfer resistances ($R_{ct,1}$ and $R_{ct,2}$). The first semicircle in the high-frequency region reflects the charge-transfer resistance at the interface between Si and cocatalyst ($R_{ct,1}$), and the second arc in the low-frequency region represents another one at the interface of cocatalyst/electrolyte ($R_{ct,2}$), corresponding to the catalytic kinetics.[44, 45] The fitted values of R_s, $R_{ct,1}$, and $R_{ct,2}$ are listed in **Table 4.3**. To be precise, the R_s values of as-prepared photocathodes are almost the same, suggesting the similar resistivity of the electrolyte between working and reference electrodes for these photocathodes. Moreover, all photocathodes exhibit small and similar $R_{ct,1}$ value, indicating their good conductivity due to the incorporation of cocatalysts. Next, three Co-P/WS_x/Si photocathodes exhibit much lower $R_{ct,2}$ values than that of the Co-P/Si photocathode, which indicates that the Co-P cocatalyst on the thin-film WS_x can efficiently reduce the charge-transfer resistance at the cocatalyst/electrolyte interface. In particular, the lowest $R_{ct,2}$ value of Co-P/20WS_x/Si suggests that the thin-film 20WS_x with uniform distribution helps to generate a suitable Co-P cocatalyst to promote electron transfer from Co-P cocatalyst to the electrolyte, thus confirming the improved PEC-HER activities. In addition, PL emission was also carried out to help to judge the behavior of the charge carrier transfer. As shown in **Figure 4.13**, all Co-P/WS_x/Si and Co-P/Si samples show PL peaks at 608 nm, ascribed to the recombination of photogenerated electron-hole pairs in Si.[10] The Co-P/Si without WS_x thin-film shows the highest PL intensity, while all three Co-P/WS_x/Si shows less PL intensity. Specifically, a distinct fluorescence quenching occurs in Co-P/20WS_x/Si, suggesting that the charge carrier recombination is suppressed to the greatest extent. It exemplifies that the more robust compatibility of the Co-P cocatalyst and the thin-film WS_x could efficiently promote the charge transfer, consistent with the EIS analysis and PEC HER performance.

4.3.4 Long-term stability testing

In order to determine the long-term stability of the as-prepared photocathodes, the chronoamperometric test at 0 V_{RHE} was conducted, as depicted in **Figure 4.14**. After a duration time of 13 h, the decay of photocurrent density (calculated after 2-h activation) is in the following order: Co-P/Si (−22%) > Co-P/5WS_x/Si (−9%) > Co-P/30WS_x/Si (−7%) > Co-P/20WS_x/Si (−2%). The PEC long-term stability of the optimal Co-P/20WS_x/Si photocathode was confirmed in **Figure 4.15**. The Co-P/20WS_x/Si

photocathode exhibits a photocurrent density of about −27.5 mA cm^{-2} at an applied potential at 0 V_{RHE} over 300 h, which is better than other representative Si-based photocathodes in alkaline solutions so far in Table 4.2. After the 300-h duration test at 0 V_{RHE}, the potential is changed to +0.1, +0.2, and +0.3 V_{RHE}, retaining the photocurrent densities of −24.3, −13.7, and −2.5 mA cm^{-2}, respectively. Even if the applied potential is recovered to 0 V_{RHE} after 375 h, the Co-P/20WS_x/Si photocathode can still return to a stable photocurrent density of approximately −28.4 mA cm^{-2}, and there is no noticeable fading of photocurrent density over 25 h, implying the excellent long-term durability. In addition, the LSV curves of Co-P/20WS_x/Si photocathode were collected before and after the stability test of 400 h in **Figure 4.16**. Although it is found that the photocurrent density at 0V_{RHE} increased slightly, which may be caused by the shedding of partial Co-P cocatalyst due to the violent hydrogen bubble popping, the remaining WS_x layer can prevent serious deep corrosion, as shown in the TEM image (**Figure 4.17).** Notably, there is almost no negative shift in onset potential, demonstrating the superior adhesion of the interface of cocatalyst/protector/semiconductor. In order to determine the H_2 evolution rate of Co-P/20WS_x/Si photocathode (an area of 0.4 cm^2), the chronoamperometric test at 0 V_{RHE} was conducted under a completely sealed condition. The corresponding *J*−*t* profile and *Q* plots are depicted in **Figure 4.18**a. The amount of evolved H_2 on Co-P/20WS_x/Si photocathode is 180.1 μmol after 60 min of consecutive light illumination, and a high Faradaic efficiency of near 99% is calculated based on the amount of generated H_2 and the electrons as in Figure 4.18b, revealing the full utilization of the photoexcited electrons for PEC HER.

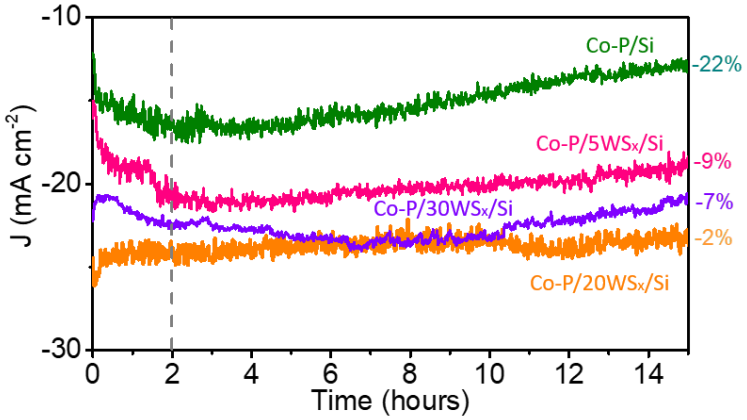

Figure 4.14 The chronoamperometric current–time profiles of Co-P/Si, Co-P/5WS_x/Si, Co-P/20WS_x/Si, and Co-P/30WS_x/Si at 0 V_{RHE} in 1 M KOH under simulated AM1.5G illumination.

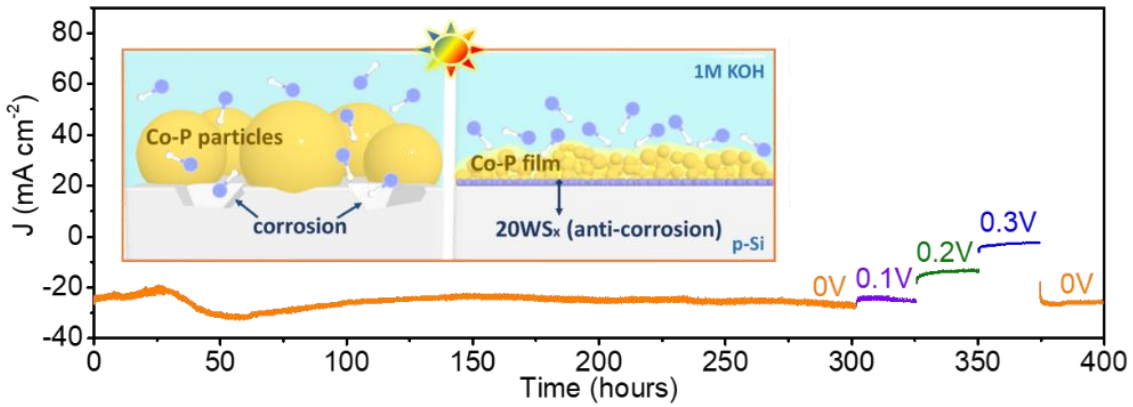

Figure 4.15 The chronoamperometric current–time profiles of Co-P/20WS_x/Si at 0, 0.1, 0.2, and 0.3 V_{RHE} in 1.0 M KOH. Schematic diagram of the anti-corrosive mechanism of Co-P/20WS_x/Si compared to Co-P/Si without 20WS_x protection layer inset.

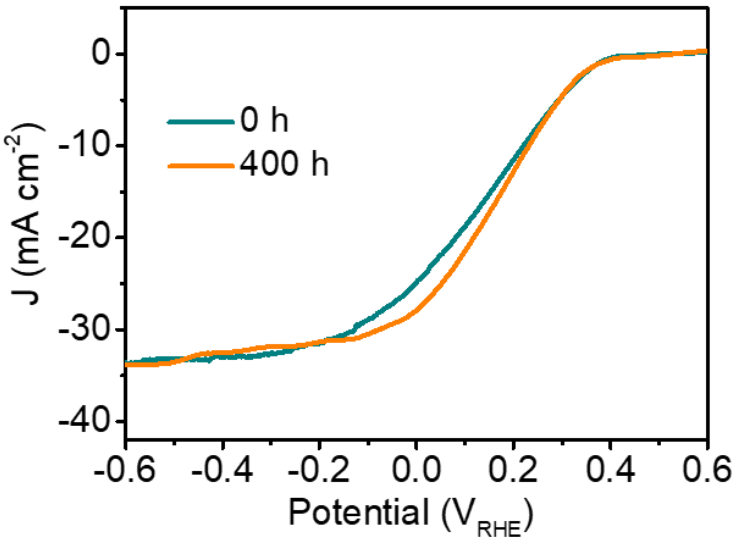

Figure 4.16 LSV curves of Co-P/20WS_x/Si photocathode before and after the PEC-HER long-term stability test.

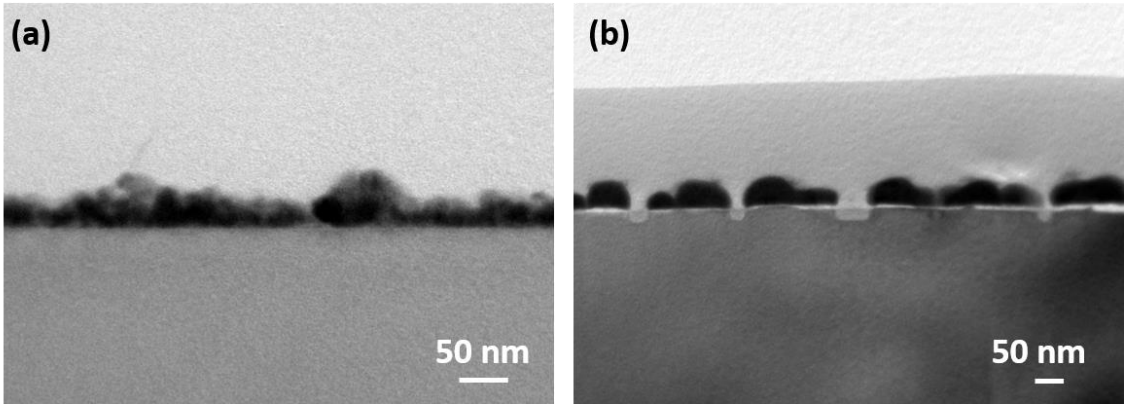

Figure 4.17 The TEM images of Co-P/20WS_x/Si (a) before and (b) after the PEC-HER test.

The schematic diagram (the inset of Figure 4.15) shows the difference between the presence and absence of a uniform WS_x thin film as a protective layer on the stability against alkali corrosion and the morphology of the Co-P cocatalysts. The absence of WS_x thin film makes the Si lose effective resistance to alkali corrosion and results in the Co-P particle morphology, where the gaps between Co-P particles allow the alkaline electrolyte to immerse and corrode the unprotected Si. On the contrary, uniform WS_x thin film has good alkali corrosion resistance and could also be used as a nucleation substrate to form a dense and uniform Co-P film cocatalyst, confirming the superior long-term stability of Co-P/WS_x/Si photocathode in 1.0 M KOH.

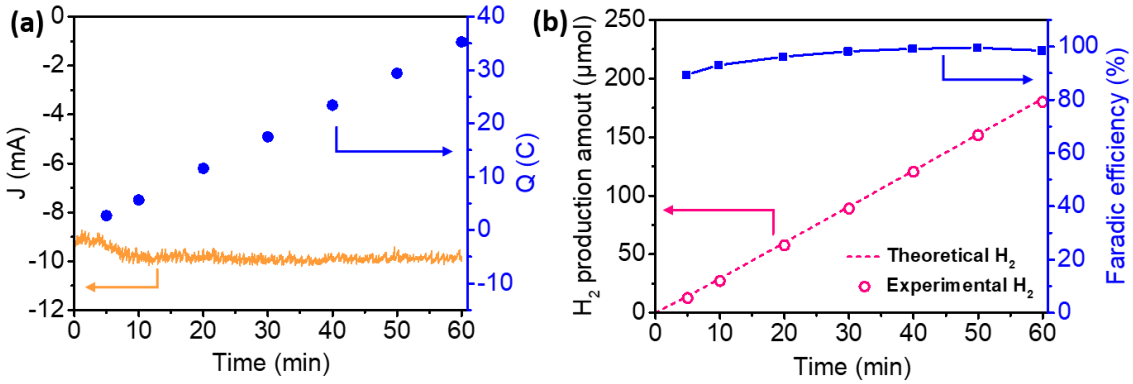

Figure 4.18 (a) *J*−*t* profile and *Q* plots of Co-P/20WS_x/Si photocathode at 0 V_{RHE}, (b) the corresponding H_2 evolution amounts and Faradaic efficiency with illumination time.

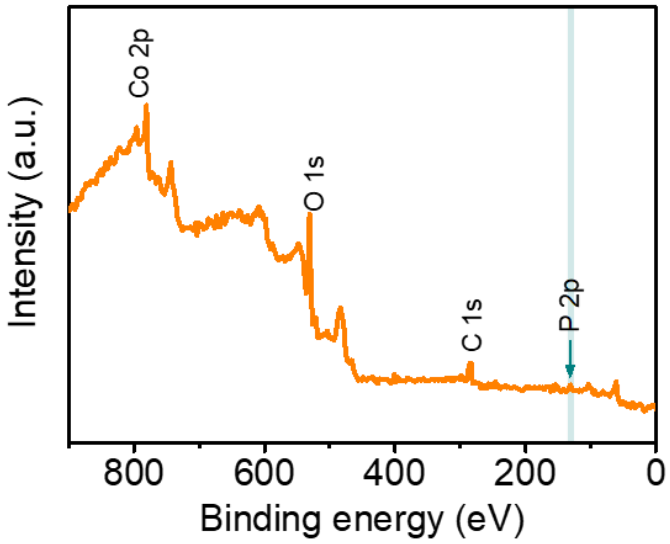

Figure 4.19 XPS survey spectrum of Co-P/20WS_x/Si.

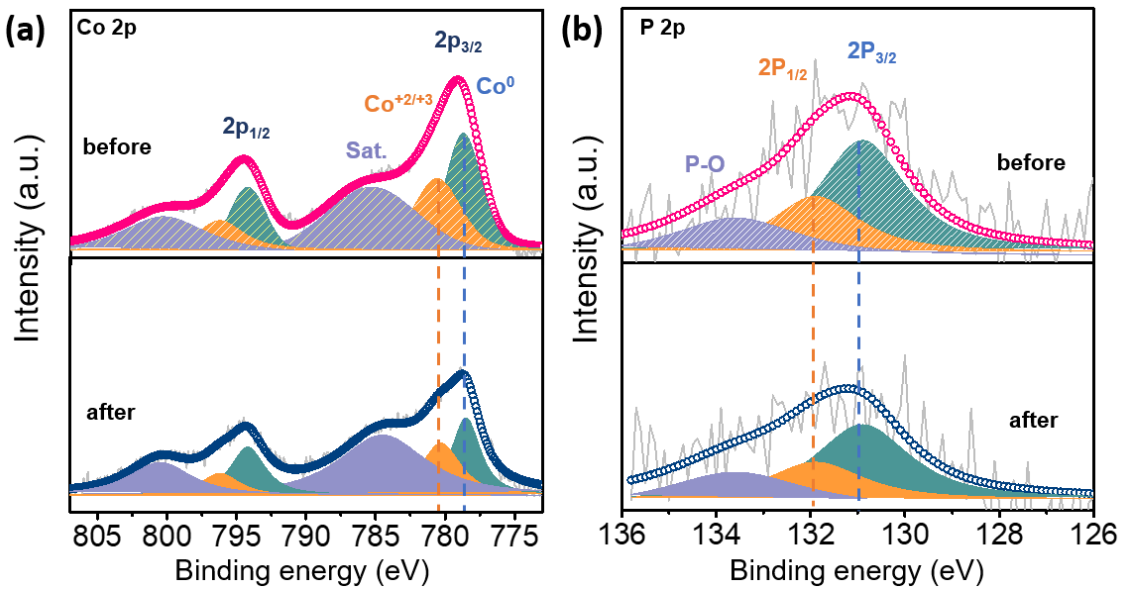

Figure 4.20 High-resolution XPS spectra of Co-P/20WS$_x$/Si in the regions of (a) Co 2p and (b) P 2p before and after the PEC-HER test.

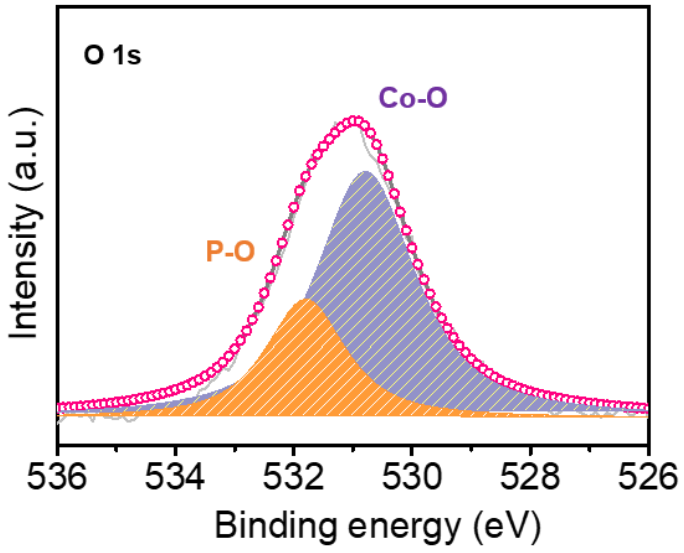

Figure 4.21 High-resolution XPS spectra of O 1s for Co-P/20WS$_x$/Si.

XPS measurements before and after the PEC-HER test within Co-P/20WS$_x$/Si photocathode were carried out to investigate the chemical change of the Co-P film cocatalyst. The signals of Co, P, C, and O elements were detected as displayed in the XPS survey spectra (**Figure 4.19**). In Co 2p XPS spectrum of the Co-P/20WS$_x$/Si photocathode (top of **Figure 4.20**a) before the long-term test, two dominant peaks at 778.7 (Co 2p$_{3/2}$) and 794.2 eV (Co 2p$_{1/2}$) are ascribed to Co^0, while the peak at around 780.6 eV (Co 2p$_{3/2}$) and 796.3 eV (Co 2p$_{1/2}$) are associated with Co$^{+2/+3}$ species, matching well with the Co-P alloy system.[37, 46, 47] The remaining peaks located at ~785.4 and 800.3 eV are satellite

peaks. Moreover, the P 2p peaks (the top of Figure 4.20b) could be deconvoluted into two doublets of P $2p_{3/2}$ (130.9 eV) and P $2p_{1/2}$ (131.9 eV), and a peak centered at 133.6 eV attributed to P−O species, possibly resulting from either the unavoidable oxidation of surface exposed to the air or remains from the electrochemical decomposition of $NaPH_2O_2$.[48] It can also be demonstrated by the XPS spectrum of O 1s, which can be deconvoluted into two peaks of Co−O (530.8 eV) and P−O (531.9 eV) (**Figure 4.21**). After the stability test in the alkaline electrolyte (the bottom of Figures 4.20a−b), the XPS intensities of both Co 2p and P 2p peaks are reduced to a certain extent, which is responsible for the slightly higher photocurrent density observed in the LSV curve of Co-P/20WS_x/Si photocathode after the test. Except for this change, there is no noticeable peak shift for Co and P elements compared with fresh samples. Similarly, for the XRD pattern of the Co-P/20WSx/Si photocathode after the durability test, there is no peak change for the Co-P signal at 44.4°, as shown in **Figure 4.22**. Therefore, the above results indicate that the Co-P cocatalyst within the optimized Co-P/20WS_x/Si photocathode is stable under such an alkaline environment, verifying the long-term durability of PEC HER.

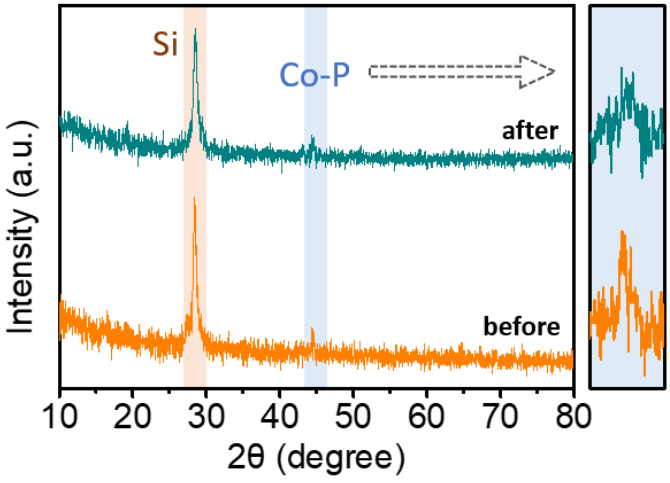

Figure 4.22 The thin-film XRD patterns of Co-P/20WS_x/Si before and after the PEC-HER test.

4.4 Conclusions

The synergetic coupling of the Co-P film cocatalyst with the thin-film WS_x protection layer on planar p-Si photocathode was investigated for efficient and durable PEC HER in alkaline solution. The thin-film WS_x protection layer plays a trifunctional role in 1) supporting excellent anti-corrosion for the Si substrate, 2) providing an appropriate

nucleation base for the morphology optimization of Co-P cocatalyst with anti-reflection, and 3) promoting the electron transfer from Si semiconductor to Co-P cocatalyst. The Co-P cocatalyst could be modulated by controlling thin-film WS_x morphology to have the least light-blocking effect but retain the catalytic activity. The complementary integration of the Co-P film cocatalyst on WS_x/Si photocathode exhibits superior catalytic properties (onset potential of +0.47 V_{RHE}, photocurrent density of −25.1 mA cm^{-2} at 0 V_{RHE}), which benefits from the significantly enhanced reaction kinetics by promoting electron transfer. Meanwhile, through such rational structure, the optimal Co-P/WS_x/Si photocathode possesses superior durability up to 300 h at a high photocurrent density above −25 mA cm^{-2} at 0 V_{RHE} without noticeable degradation in alkaline solution. This study provides a scalable strategy for future Si-based water splitting systems.

References

1. W. Vijselaar, R.M. Tiggelaar, H. Gardeniers, J. Huskens, Efficient and Stable Silicon Microwire Photocathodes with a Nickel Silicide Interlayer for Operation in Strongly Alkaline Solutions. *ACS Energy Lett.,* **2018**, *3* (5), 1086-1092.
2. R. Fan, J. Zhou, W. Xun, S. Cheng, S. Vanka, T. Cai, S. Ju, Z. Mi, M. Shen, Highly efficient and stable Si photocathode with hierarchical MoS_2/Ni_3S_2 catalyst for solar hydrogen production in alkaline media. *Nano Energy,* **2020**, *71*, 104631.
3. X. Zhao, X. Li, D. Xiao, M. Gong, L. An, P. Gao, J. Yang, D. Wang, Isolated Pd atom anchoring endows cobalt diselenides with regulated water-reduction kinetics for alkaline hydrogen evolution. *Appl. Catal. B Environ.,* **2021**, *295*, 120280.
4. Y. Men, Y. Tan, P. Li, X. Cao, S. Jia, J. Wang, S. Chen, W. Luo, Tailoring the 3d-orbital electron filling degree of metal center to boost alkaline hydrogen evolution electrocatalysis. *Appl. Catal. B Environ.,* **2021**, *284*, 119718.
5. K. Sivula, R. van de Krol, Semiconducting materials for photoelectrochemical energy conversion. *Nat. Rev. Mater. ,* **2016**, *1* (2), 15010.
6. W. Zhou, F. Niu, S.S. Mao, S. Shen, Nickel complex engineered interface energetics for efficient photoelectrochemical hydrogen evolution over p-Si. *Appl. Catal. B Environ.,* **2018**, *220*, 362-366.
7. S. Li, G. Yang, P. Ge, H. Lin, Q. Wang, X. Ren, S. Luo, D. Philo, K. Chang, J. Ye, Engineering Heterogeneous NiS_2/NiS Cocatalysts with Progressive Electron Transfer from Planar p-Si Photocathodes for Solar Hydrogen Evolution. *Small*

Methods, **2021**, *5* (4), 2001018.

8. C.-J. Chen, V. Veeramani, Y.-H. Wu, A. Jena, L.-C. Yin, H. Chang, S.-F. Hu, R.-S. Liu, Phosphorous-doped molybdenum disulfide anchored on silicon as an efficient catalyst for photoelectrochemical hydrogen generation. *Appl. Catal. B Environ.,* **2020**, *263*, 118259.
9. M.G. Kast, L.J. Enman, N.J. Gurnon, A. Nadarajah, S.W. Boettcher, Solution-Deposited F:SnO_2/TiO_2 as a Base-Stable Protective Layer and Antireflective Coating for Microtextured Buried-Junction H_2-evolving Si Photocathodes. *ACS Appl. Mater. Interfaces,* **2014**, *6* (24), 22830-22837.
10. J. Zheng, Y. Lyu, R. Wang, C. Xie, H. Zhou, S.P. Jiang, S. Wang, Crystalline TiO_2 protective layer with graded oxygen defects for efficient and stable silicon-based photocathode. *Nat. Commun.,* **2018**, *9* (1), 3572.
11. S. Hu, M.R. Shaner, J.A. Beardslee, M. Lichterman, B.S. Brunschwig, N.S. Lewis, Amorphous TiO_2 coatings stabilize Si, GaAs, and GaP photoanodes for efficient water oxidation. *Science,* **2014**, *344* (6187), 1005.
12. Y.W. Chen, J.D. Prange, S. Dühnen, Y. Park, M. Gunji, C.E.D. Chidsey, P.C. McIntyre, Atomic layer-deposited tunnel oxide stabilizes silicon photoanodes for water oxidation. *Nat. Mater.,* **2011**, *10* (7), 539-544.
13. H. Lin, S. Li, G. Yang, K. Zhang, D. Tang, Y. Su, Y. Li, S. Luo, K. Chang, J. Ye, In Situ Assembly of MoS_x Thin-Film through Self-Reduction on p-Si for Drastic Enhancement of Photoelectrochemical Hydrogen Evolution. *Adv. Funct. Mater.,* **2021**, *31* (3), 2007071.
14. Y. Zhong, Y. Shao, F. Ma, Y. Wu, B. Huang, X. Hao, Band-gap-matched CdSe QD/WS_2 nanosheet composite: Size-controlled photocatalyst for high-efficiency water splitting. *Nano Energy,* **2017**, *31*, 84-89.
15. Y. Yang, H. Fei, G. Ruan, Y. Li, J.M. Tour, Vertically Aligned WS_2 Nanosheets for Water Splitting. *Adv. Funct. Mater.,* **2015**, *25* (39), 6199-6204.
16. Y. Shi, B. Zhang, Recent advances in transition metal phosphide nanomaterials: synthesis and applications in hydrogen evolution reaction. *Chem. Soc. Rev.,* **2016**, *45* (6), 1529-1541.
17. N. Jiang, B. You, M. Sheng, Y. Sun, Electrodeposited Cobalt-Phosphorous-Derived Films as Competent Bifunctional Catalysts for Overall Water Splitting. *Angew.*

Chem. Int. Ed., **2015**, *54* (21), 6251-6254.

18. J.H. Kim, S. Han, Y.H. Jo, Y. Bak, J.S. Lee, A precious metal-free solar water splitting cell with a bifunctional cobalt phosphide electrocatalyst and doubly promoted bismuth vanadate photoanode. *J. Mater. Chem. A,* **2018**, *6* (3), 1266-1274.
19. A. Chunduri, S. Gupta, O. Bapat, A. Bhide, R. Fernandes, M.K. Patel, V. Bambole, A. Miotello, N. Patel, A unique amorphous cobalt-phosphide-boride bifunctional electrocatalyst for enhanced alkaline water-splitting. *Appl. Catal. B Environ.,* **2019**, *259*, 118051.
20. K. Xu, H. Cheng, H. Lv, J. Wang, L. Liu, S. Liu, X. Wu, W. Chu, C. Wu, Y. Xie, Controllable Surface Reorganization Engineering on Cobalt Phosphide Nanowire Arrays for Efficient Alkaline Hydrogen Evolution Reaction. *Adv. Mater.,* **2018**, *30* (1), 1703322.
21. Y. Li, H. Li, K. Cao, T. Jin, X. Wang, H. Sun, J. Ning, Y. Wang, L. Jiao, Electrospun three dimensional Co/CoP@nitrogen-doped carbon nanofibers network for efficient hydrogen evolution. *Energy Storage Mater.,* **2018**, *12*, 44-53.
22. L.-A. Stern, L. Liardet, M.T. Mayer, C.G. Morales-Guio, M. Grätzel, X. Hu, Photoelectrochemical deposition of CoP on cuprous oxide photocathodes for solar hydrogen production. *Electrochim. Acta,* **2017**, *235*, 311-316.
23. C.W. Roske, E.J. Popczun, B. Seger, C.G. Read, T. Pedersen, O. Hansen, P.C. Vesborg, B.S. Brunschwig, R.E. Schaak, I. Chorkendorff, H.B. Gray, N.S. Lewis, Comparison of the Performance of CoP-Coated and Pt-Coated Radial Junction n^+p-Silicon Microwire-Array Photocathodes for the Sunlight-Driven Reduction of Water to H_2(g). *J. Phys. Chem. Lett.,* **2015**, *6* (9), 1679-1683.
24. X.-Q. Bao, M. Fatima Cerqueira, P. Alpuim, L. Liu, Silicon nanowire arrays coupled with cobalt phosphide spheres as low-cost photocathodes for efficient solar hydrogen evolution. *Chem. Commun.,* **2015**, *51* (53), 10742-10745.
25. T.R. Hellstern, J.D. Benck, J. Kibsgaard, C. Hahn, T.F. Jaramillo, Engineering Cobalt Phosphide (CoP) Thin Film Catalysts for Enhanced Hydrogen Evolution Activity on Silicon Photocathodes. *Adv. Energy Mater.,* **2016**, *6* (4), 1501758.
26. S.M. Thalluri, B. Wei, K. Welter, R. Thomas, V. Smirnov, L. Qiao, Z. Wang, F. Finger, L. Liu, Inverted Pyramid Textured p-Silicon Covered with Co_2P as an Efficient and Stable Solar Hydrogen Evolution Photocathode. *ACS Energy Lett.,* **2019**, *4* (7),

1755-1762.

27. S.M. Thalluri, J. Borme, K. Yu, J. Xu, I. Amorim, J. Gaspar, L. Qiao, P. Ferreira, P. Alpuim, L. Liu, Conformal and continuous deposition of bifunctional cobalt phosphide layers on p-silicon nanowire arrays for improved solar hydrogen evolution. *Nano Res.,* **2018**, *11* (9), 4823-4835.

28. I. Paseka, J. Velicka, Hydrogen evolution and hydrogen sorption on amorphous smooth Me-P(x) (Me=Ni, Co and Fe-Ni) electrodes. *Electrochim. Acta,* **1997**, *42* (2), 237-242.

29. H. Liu, X. Ma, H. Hu, Y. Pan, W. Zhao, J. Liu, X. Zhao, J. Wang, Z. Yang, Q. Zhao, H. Ning, M. Wu, Robust NiCoP/CoP Heterostructures for Highly Efficient Hydrogen Evolution Electrocatalysis in Alkaline Solution. *ACS Appl. Mater. Interfaces,* **2019**, *11* (17), 15528-15536.

30. C.D. Nguyen, T.L.M. Pham, T.Y. Vu, V.B. Mai, K.L. Vu-Huynh, Hierarchical Zn-Co-P nanoneedle arrays supported on three-dimensional framework as efficient electrocatalysts for hydrogen evolution reaction in alkaline condition. *J. Electroanal. Chem.,* **2020**, *858*.

31. M. Cabán-Acevedo, M.L. Stone, J.R. Schmidt, J.G. Thomas, Q. Ding, H.-C. Chang, M.-L. Tsai, J.-H. He, S. Jin, Efficient hydrogen evolution catalysis using ternary pyrite-type cobalt phosphosulphide. *Nat. Mater.,* **2015**, *14* (12), 1245-1251.

32. N. Bai, Q. Li, D. Mao, D. Li, H. Dong, One-Step Electrodeposition of Co/CoP Film on Ni Foam for Efficient Hydrogen Evolution in Alkaline Solution. *ACS Appl. Mater. Interfaces,* **2016**, *8* (43), 29400-29407.

33. S. Li, P. Ge, F. Jiang, H. Shuai, W. Xu, Y. Jiang, Y. Zhang, J. Hu, H. Hou, X. Ji, The advance of nickel-cobalt-sulfide as ultra-fast/high sodium storage materials: The influences of morphology structure, phase evolution and interface property. *Energy Storage Mater.,* **2019**, *16*, 267-280.

34. S. Liu, Y. Xu, D. Chanda, L. Tan, R. Xing, X. Li, L. Mao, N. Kazuya, A. Fujishima, Ultrathin WS_2 nanosheets vertically aligned on TiO_2 nanobelts as efficient alkaline hydrogen evolution electrocatalyst. *Int. J. Hydrogen Energy,* **2020**, *45* (3), 1697-1705.

35. V. Ezhilselvi, H. Seenivasan, P. Bera, C. Anandan, Characterization and corrosion behavior of Co and Co–P coatings electrodeposited from chloride bath. *RSC Adv.,*

2014, *4* (86), 46293-46304.

36. V.E. Selvi, H. Seenivasan, K.S. Rajam, Electrochemical corrosion behavior of pulse and DC electrodeposited Co–P coatings. *Surf. Coat. Technol.,* **2012**, *206* (8), 2199-2206.

37. P. Bera, H. Seenivasan, K.S. Rajam, V.K. William Grips, Characterization of amorphous Co–P alloy coatings electrodeposited with pulse current using gluconate bath. *Appl. Surf. Sci.,* **2012**, *258* (24), 9544-9553.

38. R. Fan, S. Cheng, G. Huang, Y. Wang, Y. Zhang, S. Vanka, G.A. Botton, Z. Mi, M. Shen, Unassisted solar water splitting with 9.8% efficiency and over 100 h stability based on Si solar cells and photoelectrodes catalyzed by bifunctional Ni–Mo/Ni. *J. Mater. Chem. A,* **2019**, *7* (5), 2200-2209.

39. J.-Y. Jung, J.-Y. Yu, J.-H. Lee, Dynamic Photoelectrochemical Device Using an Electrolyte-Permeable $NiO_x/SiO_2/Si$ Photocathode with an Open-Circuit Potential of 0.75 V. *ACS Appl. Mater. Interfaces,* **2018**, *10* (9), 7955-7962.

40. J. Zhao, L. Cai, H. Li, X. Shi, X. Zheng, Stabilizing Silicon Photocathodes by Solution-Deposited Ni–Fe Layered Double Hydroxide for Efficient Hydrogen Evolution in Alkaline Media. *ACS Energy Lett.,* **2017**, *2* (9), 1939-1946.

41. J. Feng, M. Gong, M.J. Kenney, J.Z. Wu, B. Zhang, Y. Li, H. Dai, Nickel-coated silicon photocathode for water splitting in alkaline electrolytes. *Nano Res.,* **2015**, *8* (5), 1577-1583.

42. J.-Y. Jung, J.-Y. Yu, S. Yoon, B. Yoo, J.-H. Lee, Charge Transfer Kinetics of Photo-Electrochemical Hydrogen Evolution Improved by Nonstoichiometric Ni-rich NiO_x-Coated Si Photocathode in Alkaline Electrolyte. *Adv. Sust. Syst.* , **2018**, *2* (2), 1700138.

43. D. Bae, S. Shayestehaminzadeh, E.B. Thorsteinsson, T. Pedersen, O. Hansen, B. Seger, P.C.K. Vesborg, S. Ólafsson, I. Chorkendorff, Protection of Si photocathode using TiO_2 deposited by high power impulse magnetron sputtering for H_2 evolution in alkaline media. *Sol. Energy Mater Sol. Cells,* **2016**, *144*, 758-765.

44. Q. Ding, F. Meng, C.R. English, M. Cabán-Acevedo, M.J. Shearer, D. Liang, A.S. Daniel, R.J. Hamers, S. Jin, Efficient Photoelectrochemical Hydrogen Generation Using Heterostructures of Si and Chemically Exfoliated Metallic MoS_2. *J. Am. Chem. Soc.,* **2014**, *136* (24), 8504-8507.

45. G. Yang, S. Li, X. Wang, B. Ding, Y. Li, H. Lin, D. Tang, X. Ren, Q. Wang, S. Luo, J. Ye, A universal strategy boosting photoelectrochemical water oxidation by utilizing MXene nanosheets as hole transfer mediators. *Appl. Catal. B Environ.,* **2021**, *297*, 120268.

46. K. Liu, C. Zhang, Y. Sun, G. Zhang, X. Shen, F. Zou, H. Zhang, Z. Wu, E.C. Wegener, C.J. Taubert, J.T. Miller, Z. Peng, Y. Zhu, High-Performance Transition Metal Phosphide Alloy Catalyst for Oxygen Evolution Reaction. *ACS Nano,* **2018**, *12* (1), 158-167.

47. W. Zhen, Y. Guo, Y. Wu, G. Lu, Co–P/graphene alloy catalysts doped with Cu and Ni for efficient photocatalytic hydrogen generation. *New J. Chem.,* **2017**, *41* (22), 13804-13811.

48. Y. Zhang, L. Gao, E.J.M. Hensen, J.P. Hofmann, Evaluating the Stability of Co_2P Electrocatalysts in the Hydrogen Evolution Reaction for Both Acidic and Alkaline Electrolytes. *ACS Energy Lett.,* **2018**, *3* (6), 1360-1365.

Chapter 5 Conclusions and future prospects

5.1 General conclusions

In this thesis, the main objective is to develop efficient and stable planar Si-based photocathodes via the great efforts in surface/interface engineering for comprehensively enhanced PEC-HER performances. Specifically, three vital strategies for improving the catalytic performance of Si-based photocathodes have been investigated, mainly including 1) the construction of Si buried junction structure acts as a strong built-in electric field with a large energy band offset to restrain carrier recombination and facilitate charge transfer, 2) the design and optimization of cost-effective cocatalysts alleviate the inert active surface of Si to enhance surface HER kinetics at the solid/liquid interface, 3) the interface modulation between the Si and the cocatalyst by inserting a functional interlayer for efficient charge transfer and high mechanical stability. Therefore, a series of findings in this study provide deep understanding for Si surface optimization, cocatalyst design, and Si/cocatalyst interface modulation, as well as highlight the potential importance of the applied surface/interface engineering strategies for future practical Si-based PEC applications. The detailed study could be concluded in the following parts.

1. Construction of buried a-Si/c-Si junction photocathodes for boosting photoelectrochemical hydrogen production

In this part, an a-Si/c-Si junction photocathode with the co-deposition of Pt nanoparticles was constructed by a room-temperature and mild-condition approach to achieve facile electron transfer for enhanced solar hydrogen evolution. The Pt/a-Si/c-Si exhibits an onset potential of 0.42 V_{RHE} and a photocurrent of 35.0 mA cm^{-2} at 0 V_{RHE} in 0.5 M H_2SO_4 under AM 1.5 G, as well as a 3.98% half-cell solar-to-hydrogen efficiency, which is much greater than the case without a-Si. The enhanced performance of Pt/a-Si/c-Si is attributed to the introduction of a-Si layer, which not only functions as a good passivation layer and electron transfer mediator to produce the a-Si/c-Si junction with a large energy band shift to ensure facile charge transfer, but also serves as the growth substrate to obtain smaller and more uniform Pt nanoparticles. This work proposes a feasible manner for enhancing the photoresponse of Si-based photocathodes by developing accessible and controllable Si buried junction structures.

2. Engineering heterogeneous NiS_2/NiS cocatalysts with progressive electron transfer from planar p-Si Photocathodes for solar hydrogen evolution.

In this part, it was demonstrated that the NiS_2/NiS (NNH) heterojunction as excellent cocatalyst is applied to a planar p-Si substrate for enhanced PEC-HER performance. Though tuning the structure of precursors, the in-situ growing NNH was successfully synthesized, including the defect-rich NiS_2 phase as the active sites for hydrogen evolution and the NiS phase as the media for progressive electron transfer. Thus, the photogenerated electron is transferred from p-Si to n-NiS within NNH, followed by to Ni^{2+} and/or S_2^{2-} of the defect-rich n-NiS_2 phase. The NNH/Si photocathode exhibits an onset potential of +0.28 V_{RHE}, a photocurrent density of 18.9 mA cm^{-2} at 0 V_{RHE} and a 0.9% HC-STH efficiency in 0.5 M H_2SO_4 under simulated irradiation of 100 mW cm^{-2} with an AM 1.5 G filter, which is much superior compared with those of NiS_2/Si and NiS/Si photocathodes. This study establishes a firm foundation to explore more earth-abundant metal sulfides for high-performance PEC-HER systems that are based on the planar Si photoelectrodes for progressive electron transfer by the appropriate engineering of heterostructures.

3. A synergetic strategy to construct anti-reflective and anti-corrosive Co-P/WS_x/Si photocathode for durable hydrogen evolution in alkaline condition

In this part, a synergetic strategy is proposed to employ an anti-reflective Co-P film cocatalyst modulated via self-assembly of protective-layer WS_x onto Si photocathode for durable PEC HER under alkaline conditions. The controllable WS_x thin-film was self-assembled on the surface of Si substrate as a uniform protection layer, which efficiently ensures the excellent anti-alkali corrosion of Si semiconductors. Furthermore, the WS_x protection layer also serves as an appropriate nucleation base to modulate the structure of Co-P cocatalyst to possess anti-reflection, finally forming a robust and complementary architecture. The optimal Co-P/WS_x/Si photocathode exhibits an onset potential of +0.47 V_{RHE}, a photocurrent density of −25.1 mA cm^{-2} at 0 V_{RHE} in 1.0 M KOH under an AM 1.5 G simulated solar illumination. More importantly, the Co-P/WS_x/Si photocathode displays a superior durability of 300 h at 0 V_{RHE} without visible degradation. This research provides an effective approach to develop an appropriate Si protection layer that could balance the trade-off between alkalic corrosion resistance and light transmittance, and highlights the potential for further development of durable planar Si-based PEC-HER applications in alkaline media.

5.2 Future prospects

In the pursuit of developing the practical photocathodes with high efficiency and stability, Si has been extensively investigated and recognized as a promising light absorber for hydrogen evolution from PEC water splitting due to its excellent light absorption capability, morphology customizability, well-established production technologies. However, relatively high surface reflectivity, sluggish surface kinetics, as well as potential photo-corrosion and extreme pH electrolyte corrosion during PEC operation remain serious drawbacks of using Si photocathodes. Based on this, reports on the surface/interface engineering of Si-based photocathodes have achieved staged advances, while the stable operation and high solar-to-hydrogen conversion efficiency are still challenging and require further in-depth development. Some issues listed below are worthy of special attention:

(1) So far, the 1.12 eV band gap of Si allows efficient absorption of light from ultraviolet to visible and even near-infrared wavelengths, which is the frequently used photoabsorber for photocathodes. However, limited by the indirect band-edge absorption of Si semiconductors, it remains challenging to achieve the maximum theoretical efficiency of light utilization. The design of Si-based junction structures through integration with other functional semiconductors have also been demonstrated to be powerful interface engineering strategies for Si-based photocathodes to optimize charge transfer and suppress the carrier recombination. However, the development of high-quality tunnel layer materials that can match Si with appropriate energy band alignment is still a major difficulty in future research. Furthermore, the reports about photonic textured Si photocathodes have potential rewards in light absorption and antireflection over the planar counterparts. Various Si micro/nanostructures with increased internal surface area can improve charge carrier collection, internal reflection, and light conversion efficiency. It is worth noting that light absorption and surface recombination should be balanced when constructing surface-textured Si, because the textured structure may generate impurities and defects leading to carrier recombination.

(2) Loading active HER cocatalysts on Si-based photocathodes is a universal surface modification strategy to enhance the reaction kinetics at the Si/electrolyte interface and reduce the activation energies of HER. It is well known that metal-based materials as dominant HER cocatalysts shows superior catalytic activity. In particular, well-designed earth-abundant bimetal alloys or compounds as cocatalysts can exhibit better catalytic

activity and durability especially in alkaline electrolytes, mainly due to their synergetic effects of the corresponding individual components and increased structural defects (active sites). Despite the current PEC-HER performance on Si-based photocathodes has been significantly enhanced via the great efforts in various cocatalyst loading, these cocatalysts are still far from meeting the practical requirement for Si-based PEC-HER applications. On the one hand, earth-abundant metal-based cocatalysts have promising application prospects due to their cost advantages, but there is still a large space for further optimization in their catalytic performance and light transmittance. Strategies such as doping, structural, and morphological manipulations are currently employed to optimize the catalytic activity and optical properties of cocatalysts. On the other hand, the working mechanism of the cocatalyst is not clear enough and requires further in-depth analysis. Thus, the theoretical calculations and modern in situ characterization techniques should be vigorously pursued to elucidate the importance of the cocatalyst modification for Si photocathodes.

(3) The construction of a highly efficient and stable Si-based photocathode requires not only appropriate Si surface modifications and excellent cocatalyst materials, but also a high-quality interface between the cocatalyst and the Si substrate. Consequently, recent reports about Si-based photocathodes based on intermediate protection/passivation layers have been shown that proper interface engineering can effectively minimize carrier loss. Among the various functionalized interface layers, the chemical stability of TiO_2 in the full pH electrolyte range is particularly prominent compared with the metal protective layers with excellent electrical conductivity but accompanied by the parasitic light absorption. The development of other functional interlayers like MoS_2 and WS_x, although not extensively studied, should not be underestimated. The trade-off between the advantages of the additional layers and the light absorption of underneath Si is a crucial consideration for realizing active and durable photocathodes. In addition, the integration technology of Si-based photocathodes is still immature, which is the main reason why many excellent electrocatalysts and functional layer candidates cannot be applied to Si-based photocathodes. Therefore, how to construct Si photocathodes with high-quality interfaces on a large scale in a convenient, controllable, and low-cost manner has become an urgent goal to be realized.

Acknowledgement

Time flies. I still remember the first day I came to Japan to join Hokkaido University and NIMS. The three years of studying and living in Tsukuba have been a colorful, rewarding, and unforgettable journey for me. Yet, happy times are always short, and it's time to say goodbye to the old days. At the end of my Ph.D. program, I am deeply grateful for those who guided, helped, and supported my studies and life.

First of all, I would like to express my sincere gratitude to my supervisor Prof. Jinhua Ye for her professional guidance, valuable discussions, and patient encouragement over the past three years. Prof. Ye is a really nice and wise supervisor. She was always willing to share her scientific ideas and opinions with me, which I thought was absolutely helpful in ensuring the advancement of my Ph.D. research projects. Prof. Ye is also a keen-eyed researcher. Not only did she guide me to explore and discover the key points and highlights of my research work, but she was capable to focus on some seemingly "minor issues" and encouraged me to dig further. When I was writing a research paper, she also patiently helped me polish the manuscript to further refine my work. All her rigorous attitude and great enthusiasm will benefit me throughout my whole life.

Then, I am grateful to my sub-supervisors, Prof. Kiyoharu Tadanaga and Prof. Naoto Shirahata. Thank you for all your suggestions and kind help during my Ph.D. study. Great thanks to Prof. Kei Murakoshi and Prof. Kosei Ueno for their constructive comments and suggestions on my thesis and presentation.

Thirdly, I would like to thank Dr. Huiwen Lin, who helped me a lot in my research. He shared me useful opinions and suggestions in designing experiments, characterizing samples, and analyzing results, which enabled me to run my research smoothly. I want to express many thanks to all the members of the Photocatalytic Materials Group in NIMS, Dr. Gaoliang Yang, Dr. Xiaohui Ren, Dr. Shunqin Luo, Mr. Qi Wang, Mr. Bowen Deng, Mr. Davin Philo, Dr. Hui Song, Dr. Yunxiang Li, Dr. Li Shi, Dr. Kun Chang, Dr. Xusheng Wang, Dr. Yu He, Dr. Shuang Song, Ms. Lan Li, Dr. Yiming Zhang, Dr. Hengming Huang, Dr. Ningdong Feng, Dr. Dekang Huang, Dr. Mengli Li, Dr. Yao Xie, Dr. Xuelian Yu, Dr. Kang Peng, Dr. Shengyao Wang, Dr. Hong Pang, Dr. Fumihiko Ichihara, Dr. Tetsuya Kako, and Dr. Mitsutake Oshikiri for their kind helps in both experiments and daily life. I will cherish these memorable days with them forever. I would like to thank our

secretaries Ms. Kanae Hasegawa and Ms. Haruna Kurokawa, who helped me a lot in every daily thing. I would also like to thank my classmate and friend Ms. Xiaoyu Huang. We came to Tsukuba from China together three years ago. We took classes together, made presentations, and shared interesting stories about our daily lives. We also had plentiful and wonderful memories when we traveled to several beautiful places in Japan.

Furthermore, I would like to thank the China Scholarship Council for the financial support during my Ph.D. study.

Lastly, I would like to express my deep gratitude to my father Laimeng Li and my mother Xianju Wang. Thank you for your selfless love and constant encouragement all the time. You are always my inexhaustible motivation to move forward. I would also like to thank my boyfriend Zhi Chang. We fell in love at the beginning of my Ph.D. period, thank you for your love, trust, and support. Your love is the source of my happiness. I am looking forward to sharing the rest of my life with you too.